Chem Soc Rev

REVIEW ARTICLE

View Article Online
View Journal | View Issue

Cite this: *Chem. Soc. Rev.*, 2022, **51**, 7883

Calcium carbonate: controlled synthesis, surface functionalization, and nanostructured materials

Yu-Qin Niu,[ac] Jia-Hui Liu,[ac] Cyril Aymonier,[f] Simona Fermani,[be]
Damir Kralj,*[d] Giuseppe Falini*[b] and Chun-Hui Zhou*[ac]

Calcium carbonate ($CaCO_3$) is an important inorganic mineral in biological and geological systems. Traditionally, it is widely used in plastics, papermaking, ink, building materials, textiles, cosmetics, and food. Over the last decade, there has been rapid development in the controlled synthesis and surface modification of $CaCO_3$, the stabilization of amorphous $CaCO_3$ (ACC), and $CaCO_3$-based nanostructured materials. In this review, the controlled synthesis of $CaCO_3$ is first examined, including Ca^{2+}–$CO_3{}^{2-}$ systems, solid–liquid–gas carbonation, water-in-oil reverse emulsions, and biomineralization. Advancing insights into the nucleation and crystallization of $CaCO_3$ have led to the development of efficient routes towards the controlled synthesis of $CaCO_3$ with specific sizes, morphologies, and polymorphs. Recently-developed surface modification methods of $CaCO_3$ include organic and inorganic modifications, as well as intensified surface reactions. The resultant $CaCO_3$ can then be further engineered *via* template-induced biomineralization and layer-by-layer assembly into porous, hollow, or core–shell organic–inorganic nanocomposites. The introduction of $CaCO_3$ into nanostructured materials has led to a significant improvement in the mechanical, optical, magnetic, and catalytic properties of such materials, with the resultant $CaCO_3$-based nanostructured materials showing great potential for use in biomaterials and biomedicine, environmental remediation, and energy production and storage. The influences that the preparation conditions and additives have on ACC preparation and stabilization are also discussed. Studies indicate that ACC can be used to construct environmentally-friendly hybrid films, supramolecular hydrogels, and drug vehicles. Finally, the existing challenges and future directions of the controlled synthesis and functionalization of $CaCO_3$ and its expanding applications are highlighted.

Received 19th April 2022

DOI: 10.1039/d1cs00519g

rsc.li/chem-soc-rev

1. Introduction

Calcium carbonate ($CaCO_3$) ubiquitously exists in sedimentary rocks and minerals in the form of marble, limestone, and chalk, and can also be found in marine sediments.[1,2] In addition, $CaCO_3$ is present in many living organisms, functioning either as a structural support (*e.g.*, in algae,[3] sponges,[4,5] corals[6]), a form of protection (*e.g.*, shells),[7] a hard buoyancy tank (*e.g.*, cuttlebone),[8] or as a component in photoreceptor systems (*e.g.*, light-focusing eye lenses of chitons and brittlestars).[9] $CaCO_3$ is also synthesized by bacteria,[10] even in extreme biomineralization conditions,[11] and is an essential component of mineralized tissues as in the apatitic whale bone.[12,13]

Crystalline $CaCO_3$ exhibits three polymorphs: hexagonal vaterite, orthorhombic aragonite, and rhombohedral calcite, in order of increasing thermodynamic stability.[14] Two hydrated crystal phases of $CaCO_3$, monohydrocalcite ($CaCO_3{\cdot}H_2O$) and ikaite ($CaCO_3{\cdot}6H_2O$), have been known for more than a century, while recently, hemihydrate $CaCO_3{\cdot}\frac{1}{2}H_2O$ with a monoclinic structure has been discovered.[14–16] An unstable amorphous $CaCO_3$ (ACC) phase can be found in *Stylophora pistillata* corals,[17] crayfish gastroliths,[18] sea urchin spicules,[19] gastropods,[20] earthworms,[21] plant cystoliths, and other such organisms.[22] The diversity of the origins, composition, morphologies, and polymorphs of $CaCO_3$ makes it an extremely significant material for use in both scientific research and technological applications.

---

[a] Research Group for Advanced Materials & Sustainable Catalysis (AMSC), State Key Laboratory Breeding Base of Green Chemistry-Synthesis Technology, College of Chemical Engineering, Zhejiang University of Technology, Hangzhou 310032, China. E-mail: clay@zjut.edu.cn
[b] Department of Chemistry "Giacomo Ciamician", University of Bologna, Via Selmi 2, I-40126 Bologna, Italy. E-mail: giuseppe.falini@unibo.it
[c] Qing Yang Institute for Industrial Minerals, You Hua, Qing Yang, Chi Zhou 242804, China
[d] Laboratory for Precipitation Processes, Ruđer Bošković Institute, P. O. Box 1016, HR-10001 Zagreb, Croatia
[e] Interdepartmental Centre for Industrial Research Health Sciences & Technologies, University of Bologna, 40064 Bologna, Italy
[f] Univ Bordeaux, ICMCB, Bordeaux INP, UMR 5026, CNRS, F-33600 Pessac, France

$CaCO_3$ is widely used as a filler material in paper, plastics, rubber, paints, and foodstuffs,[23,24] yet its new applications, particularly as a functional nano-$CaCO_3$ material, have driven the extensive research on synthesizing $CaCO_3$ with a specific size, morphology, polymorph, or surface property.[18,23] To improve the processes used to synthesize these specific materials and the properties of the products, liquid–liquid or solid–liquid–gas routes can be tailored by adding judiciously-chosen organic compounds or polymers, which act as templates or modifiers for the nucleation and growth of $CaCO_3$.[25,26] Moreover, water-in-oil reverse emulsion methods and ultrasonic intensification processes have also been introduced to control $CaCO_3$ synthesis, while biomimetic approaches have been developed to produce $CaCO_3$ with specific structures under mild conditions.[27–29] Using these innovative strategies, a variety of $CaCO_3$ particles with different sizes, polymorphs, and morphologies (*e.g.*, spheres, hollow spheres, rods, and flower-like) have been successfully synthesized.[24,30] Meanwhile, more in-depth knowledge of the scientific understanding of the mechanisms that underpin the nucleation and growth of $CaCO_3$ under different conditions and environments and their effects on pH, temperature, supersaturation, organic modifiers, or templates, has been gained.[31,32]

In addition to the control of the dimensions, polymorphs, and morphologies of synthetic $CaCO_3$ micro-/nanoparticles (MNPs), their surface functionalities are also crucial for their

Yu-Qin Niu

Yu Qin Niu is currently a postgraduate at Research Group for Advanced Materials & Sustainable Catalysis (AMSC), College of Chemical Engineering, Zhejiang University of Technology (ZJUT), Hangzhou, China. She received her Bachelor's Degree in Chemical Engineering and Technology from Qingdao University of Science and Technology. Her research presently focuses on organic-inorganic mineral bio-composites under the supervision of Prof. Chun Hui ZHOU. She has coauthored scientific papers in respected peer-reviewed international journals.

Jia-Hui Liu

Jia Hui Liu is currently a PhD candidate at Research Group for Advanced Materials & Sustainable Catalysis (AMSC), College of Chemical Engineering, Zhejiang University of Technology (ZJUT), Hangzhou, China and under the supervision of Prof. Chun Hui Zhou. She received her Bachelor's Degree in Applied Chemistry from Anhui Jianzhu University. Her research presently focuses on colloid and surface chemistry of carbonate and clay minerals, and related hydrogels and nanostructured functional composites and their applications in healthcare, adsorption and catalysis. She has authored and coauthored several scientific papers in respected peer-reviewed international journals.

Damir Kralj

Damir Kralj is a senior scientist and a head of the Laboratory for Precipitation Processes, Ruder Boskovic Institute, Zagreb, Croatia. He studied Chemical Engineering and Chemistry at the University of Zagreb and completed his PhD in 1990. He held a research fellowship at the University of Copenhagen (Arne E. Nielsen) and a postdoc fellowship at the TU Delft (Gerda van Rosmalen). His research focus is on the kinetics and mechanisms of precipitation of slightly soluble ionic salts (calcium carbonates, oxalates, phosphates), metastable and precursor phases, interfacial interactions between mineral surfaces and dissolved species, biomineralization, pathological mineralization and industrial crystallization.

Giuseppe Falini

Prof. Giuseppe FALINI, PhD in Chemistry, is full professor in chemistry at the University of Bologna. Currently, his research activities are addressed to the design and preparation of innovative materials from waste marine biominerals and biopolymers and to the study of the biomineralization process in corals and echinoderms and under environmental stresses. He is co-author of about 230 scientific publications in international journals (two in Science). He also wrote 3 book chapters and is co-inventor of 3 patents. He has been awarded of grants from national institutions, companies and European Community (ERC Adv).

new applications. To this aim, the last decade or so has witnessed many types of *in situ* or post-modification methods having been developed to tune the surface polarity, hydrophilicity, oleophobicity, stability, and reactivity of $CaCO_3$ MNPs.[33,34] $CaCO_3$ MNPs with distinct surface properties can thus be obtained and used to produce $CaCO_3$-based or $CaCO_3$-incorporated structured materials that have growing potential and applications in biomaterials and biomedicines, and environmental applications.[35,36] It has been well established that $CaCO_3$ particles are stable at pH 7, whereas they dissolve and release carbon dioxide (CO_2) gas under acidic conditions,[37] allowing them to be functionalized with targeting molecules or polymers for targeted pH-responsive drug/gene/protein delivery.[38–40] The pH sensitivity of $CaCO_3$ also makes it a useful self-sacrificing template for producing porous or hollow organic–inorganic biomaterials.[41–43] Moreover, major advances have recently been made in combining $CaCO_3$ with contrast agents to achieve various molecular imaging modalities for diagnosis;[40,44] with different polymeric molecules to form porous biodegradable scaffolds for use in bone tissue engineering;[45] and in integrating it with biomolecules to fabricate bioceramics,[46] bone cement,[47] and hydrogels.[48] To date, $CaCO_3$ has been used in many therapeutic and theranostic applications in chemotherapy, photothermal therapy (PTT), or photodynamic therapy (PDT);[49,50] wound healing and blood clotting;[51,52] in ultrasound (US),[53,54] fluorescence,[44] or magnetic resonance imaging (MRI);[55] and multimodal imaging and therapy.[56,59,60] In addition to the above-mentioned aspects of crystalline $CaCO_3$, the preparation and stabilization of ACC have also presented a challenge. Although several synthetic routes to ACC inspired by and based on biomineralization have been developed,[57–59] those processes are sophisticated. The preparation of ACC with distinct properties is affected by the mixing of reactants and additives,[60,61] the control of emulsion formation,[62] precipitation, and other parameters such as humidity, temperature, and pressure.[63] Therein, much attention has been paid to understanding the role of additives, such as magnesium,[64] phosphorus ions,[65] polymeric compounds,[66] and, in particular, the inclusion of carboxyl-containing compounds[67–69] in the stabilization of ACC. Meanwhile, the latest studies have indicated that ACC can be used to prepare organic–inorganic hydrogels[70] and films.[71] Moreover, ACC hybrid NPs loaded with antitumor drug and coated with phospholipid/polyethylene glycol (PEG)/folic acid (FA) have been successfully prepared and used in enzyme-abundant and acidic tumor environments, exhibiting good drug release and antitumor effects, both *in vitro* and *in vivo*.[72,73]

Chun-Hui Zhou

Dr Chun Hui ZHOU, born and brought up in Miaoqian, Qingyang, Anhui, is Professor of Chemical Engineering and Leader of Research Group for Advanced Materials and Sustainable Catalysis (AMSC), Zhejiang University of Technology. He is Director of Qing Yang Institute for Industrial Minerals. He acts as AIPEA Councilor (2017-) and Vice President (2022-). He also serves as Principal Editor of Clay Minerals, Associate Editor of Clays and Clay Minerals, and Editorial Member of Applied Clay Science, Journal of Porous Materials and Journal of Inclusion Phenomena and Macrocyclic Chemistry. He worked as a visiting academic at the University of Queensland (2006-2007) and as a visiting professor at the University of Western Australia (2010). His R&D centers on clay minerals, limestone and dolomite and related functional materials as well as catalysts for converting biochemicals and biomass, He teaches Catalysis, Materials Science and Engineering, and Scientific Literacy.

In this review, the novel synthetic strategies for controlling the sizes, morphologies, and polymorphs of $CaCO_3$ are first critically surveyed, with discussion on models describing the mechanisms of $CaCO_3$ nucleation and growth. Newly-developed surface modification methods, particularly those that involve surface adsorption, surface grafting, and the encapsulation of $CaCO_3$, are highlighted and discussed in detail. Then, the state-of-the-art in terms of engineering nanostructured materials with incorporated $CaCO_3$ toward advanced applications is covered. Next, the major progress and challenges in producing and stabilizing ACC, which is an essential pre-requisite for the further development and utilization of ACC-based organic/inorganic composites, are examined. Finally, the existing issues and future direction of the controlled synthesis, surface modification of $CaCO_3$, and the stabilization of ACC and $CaCO_3$-based nanostructured materials are highlighted.

2. Controlled synthesis of $CaCO_3$ MNPs and formation mechanisms

Although the control of the size distribution, morphologies, and polymorphs of $CaCO_3$ MNPs have been the focus of many academic studies (Fig. 1),[24,74] the theoretical understanding of the crystallization/precipitation of $CaCO_3$ MNPs remains challenging toward practical technology applications. Although $CaCO_3$ can be easily prepared *via* conventional precipitation reactions by adjusting the solution pH, ion concentration, solvent species, reaction temperature, time, or the presence of additives, there is still a need to develop sophisticated strategies and innovative methods using both chemistry and chemical engineering principles to produce $CaCO_3$-based materials that have desirable properties and are suitable for use in advanced applications.[75] The controlled synthesis of $CaCO_3$ MNPs is associated with several significant shortcomings. First, $CaCO_3$ can adopt chain-, needle-, flake-, cubic-, spherical-, spindle-like, and many other morphologies, with sizes ranging from MPs to NPs (Fig. 1B). In addition, the simultaneous initial

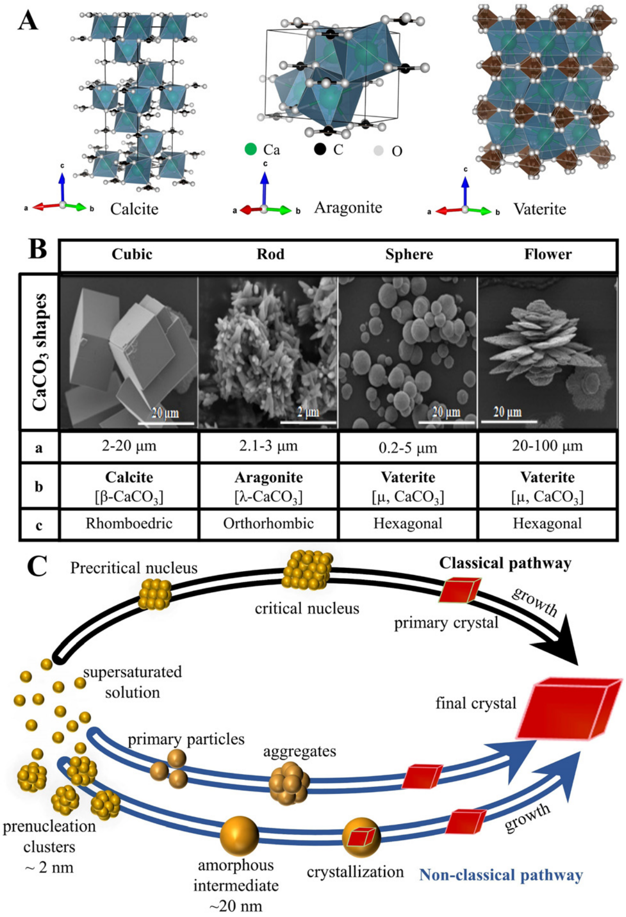

	Cubic	Rod	Sphere	Flower
a	2-20 µm	2.1-3 µm	0.2-5 µm	20-100 µm
b	Calcite [β-CaCO$_3$]	Aragonite [λ-CaCO$_3$]	Vaterite [µ, CaCO$_3$]	Vaterite [µ, CaCO$_3$]
c	Rhomboedric	Orthorhombic	Hexagonal	Hexagonal

Fig. 1 Structure, size and morphology, and polymorphism of CaCO$_3$ micro-/nanoparticles and the associated formation pathways. (A) The polymorphs and crystal structure of CaCO$_3$ (the crystal structure image was generated using the software VESTA, where the green, black, and white balls represent Ca, C, and O atoms, respectively). (B) Typical shapes of CaCO$_3$ particles (a: average diameter; b: crystalline phase; and c: crystalline system). Adapted and reprinted with permission from ref. 79. Copyright 2017, the MedCrave Group under Creative Commons Non-Commercial Attribution License (CC-BY-NC 4.0). (C) Classical and non-classical pathways to CaCO$_3$. Adapted and reprinted from ref. 80 and 81. Copyright (2008), with permission from AAAS.

formation of several polymorphs or/and hydrated forms, which is observed for the majority of CaCO$_3$ precipitation systems, presents challenges in controlled synthesis when the aim is to isolate a pure sample of a specific polymorph of CaCO$_3$ (Fig. 1A). In such systems, the kinetic or thermodynamic stabilization of metastable phases is crucial to enable control over the polymorphism and morphology of the resultant solid phase. To this aim, state-of-the-art techniques and synthetic platforms including a Ca^{2+}–CO$_3$$^{2-}$ reaction system,[76] solid–liquid–gas carbonation,[77] and a water-in-oil reverse emulsion[26] have been developed to synthesize specific types of CaCO$_3$ MNPs and polymorphs of different sizes and/or with unusual morphologies (Table 1).[78] The critical parameters that affect the size distribution, morphology, and polymorphism of CaCO$_3$ are the temperature, solvent, pH, and presence of specific additives.

In addition, the controlled synthesis of CaCO$_3$ by biomineralization has drawn much attention because of its simplicity in controlling polymorphism, morphology, and sizes of the particles, *via* the reaction of CO$_3$$^{2-}$ and Ca^{2+} in the presence of an organic matrix.[78] It is hypothesized that the organic matrix acts either as a substrate for heterogeneous nucleation or as an inhibitor of nucleation or crystal growth *via* adsorption.[82] Besides the above-mentioned methods, some other synthesis strategies that have varying levels of efficiency, such as the decomposition of Ca(HCO$_3$)$_2$,[83] spray drying techniques,[84] electric field-controlled crystallization,[85] ultrasonic irradiation,[86–88] inorganic ion polymerization reactions,[89] and the fusion of amorphous precursors under pressure,[90] have also recently been developed.

To control the synthesis of CaCO$_3$ and subsequently its respective physical and chemical properties, knowledge of the nucleation and growth mechanism of the material is fundamental. As such, models of CaCO$_3$ nucleation have been of experimental or computational focus (Fig. 1C).[91] Such processes can be predominantly explained using classical nucleation theory (CNT), which is based on the assumption that there is simple association between Ca^{2+} and CO$_3$$^{2-}$, the formation of a supersaturated solution, and stable nuclei.[92] However, CNT does not account for unexpected nucleation, proceeding *via* metastable/stable precursor phases, such as clusters at the prenucleation stage,[92] liquid-like precursors,[93] amorphous phases,[94] and even oligomers,[89] which may play important roles in the nucleation and subsequent structure control of CaCO$_3$ (Fig. 1C). Such intermediate-based nucleation theory is referred to as a non-classical nucleation pathway (NCNT) to distinguish it from classical nucleation.

2.1 Controlled synthesis of CaCO$_3$ MNPs

2.1.1 Ca^{2+}–CO$_3$$^{2-}$ system. The easiest and most efficient way to synthesize CaCO$_3$ MNPs is to employ a Ca^{2+}–CO$_3$$^{2-}$ reaction system, in which, typically, calcium salts (CaCl$_2$ or Ca(NO$_3$)$_2$) and carbonate salts (Na$_2$CO$_3$, NaHCO$_3$, K$_2$CO$_3$ or (NH$_4$)$_2$CO$_3$) are mixed to initiate a precipitation/crystallization process.[95] The size distribution, morphology, and polymorphism of the precipitate in such systems are predominantly affected by the initial supersaturation/concentration and/or ratio of the constituent ions (Ca^{2+} and CO$_3$$^{2-}$), pH, reaction temperature, and additives (Table 1).[96,97] Indeed, when the initial supersaturation is high, thermodynamically metastable and/or amorphous phases (vaterite, aragonite, CaCO$_3$·H$_2$O, CaCO$_3$·6H$_2$O, and ACC) may precipitate in a mixture with a stable polymorph, namely calcite, whereas at lower supersaturation, calcite is dominant. The formation of metastable phases, typically obtained at higher supersaturation, is kinetically favorable and precedes *via* the formation of thermodynamically stable phases, as suggested by Ostwald's rule of stages.[98] Metastable phases are expected to be formed when precipitation is fast, *i.e.*, at higher supersaturation, yet the appearance of metastable phases in lower supersaturation domains can be attributed to the influence of other experimental conditions, particularly hydrodynamic factors[99] or the

Table 1 Comparison of the different strategies developed for the controlled synthesis of $CaCO_3$ MNPs

	Conditions and additives				Characteristics					
Strategies	Additive(s)	pH	Temp. (°C)	Other	Morphology	Polymorph	Size (μm)	Advantages	Disadvantages	Ref.
Ca^{2+}–$CO_3{}^{2-}$-reaction system	DSS, PSSS	—	—	$[CaCl_2]$ = $[Na_2CO_3]$ = 5×10^{-4}–5×10^{-2} M	Spherical, toroidal, ellipsoidal	Vaterite, calcite	0.5–1.8	MPs to NPs; various morphologies; various polymorphs; (valcite, vaterite, aragonite); convenient doping with other ions; functionalized with molecules *in situ*	Poor crystallinity; difficult to control particles' size	25
	EG	9.0	25	$[CaCl_2]$ = $[Na_2CO_3]$ = 0.05, 0.1, 0.33 M; EG/H_2O ratios: 1:1, 4:1, 6:1	Spherical, ellipsoidal	Vaterite	0.4–2.7			76
	EG	8.0–10.0; 11.0–12.0	23	$[Ca^{2+}]$:$[CO_3{}^{2-}]$ ratios: 5:1, 2:1, 1:1, 1:2, 1:3	Ellipsoidal, spherical, spheroidal, rhombohedral, flower-like, irregular	Vaterite, calcite	—			109
	SDS; PAA	—	80	PAA (M_w = 8000 g mol^{-1}), [PAA] = 0.5 g L^{-1}, [SDS] = 10 mM	Hollow microspheres	Calcite	4–7			100
Solid–liquid–gas carbonation	Urea	—	150	High-pressure CO_2: 12 MPa, mass ratios: $Ca(OH)_2$/urea = 1:6	Spherical	94.2% vaterite	—	Mainly NPs; mainly cubic or rhombohedral morphology; environment preservation; effective use of mineral resources; industrially	Difficult to control the crystal shape; mainly calcite; polymorph in absence of additives; low CO_2 dissolution	110
	DMCHA, DBU, DBAE, BDA, EP	8.0–13.0	40–90	$[Ca(CH_3COO)_2]$ = 1.0 M	Rhombohedral, spherical, rod-like, shuttle-like	Calcite, vaterite, aragonite	—			78
	EDTA-2Na	—	120	Pressurized-CO_2	Hierarchical hollow microspheres	Calcite	4–6			74
Water-in-oil reverse emulsion	AOT	—	25	AOT/isooctane/water reverse microemulsion, $[CaCl_2]$ = $[Na_2CO_3]$ = 0.05 M	Rod-like, irregular, spherical	Calcite, vaterite	1–3	Size can be well controlled; soft template effect; reproducibility; simple maneuverability; low degree of agglomeration; high purity	Required a certain amount of an oil phase and surfactant	111
	—	—	65	CO_2/N_2 switchable surfactant reverse micelles[a]	Spherical, rhombohedral, dendrite-like	Vaterite, calcite	-			112
	Tween-80, Span-80	—	22	US	Spherical	Vaterite	0.02–0.03			113
Biomineralization	Phe	9.3–12.7	25	[Phe]: 0 g L^{-1}–16 g L^{-1}; CO_2 flow rate: 10–50 mL min^{-1}	Rhombohedral, spherical	Calcite, vaterite	2–5	MPs to NPs; controlled morphologies and polymorphs; good crystallinity; hierarchical structure	Complex mechanism	24
	VHVEVS peptide	7.2	20	$[Ca^{2+}]$ = 22 mM; $CO_3{}^{2-}$: hydrolyzed urea	Fiber-like, nanocubic	Aragonite, calcite	—			114

[a] *N′*-Dodecyl-*N*,*N*-dimethyl acetamidine bicarbonate; AOT: sodium bis(2-ethylhexyl) sulfosuccinate; BDA: *N*-butydimethylamine; DBAE: 2-(dibutylamino) ethanol; DBU: 1,8-diazabicycloundec-7-ene; DMCHA: *N*,*N*-dimethylcyclohexylamine; DSS: dextran sodium sulfate; EDTA-2Na: disodium salt of ethylenediaminetetraacetic acid; EG: ethylene glycol; EP: *N*-Ethylpiperidine; PAA: poly(acrylic acid); Phe: L-phenylalanine; PSSS: poly(styrene sulfonate) sodium; SDS: sodium dodecyl sulfonate; US: ultrasonication; VHVEVS: Ac-Val-His-Val-Glu-Val-Ser-$CONH_2$.

presence of additives.[100] The temporary coexistence of different solid phases indicates that several basic precipitation processes, such as nucleation, growth, dissolution, and/or aging, take place simultaneously. In such cases, besides thermodynamics, kinetic factors play a role in determining the formation of certain phases. It is often found that a kinetically favored phase forms to a large extent despite a lower thermodynamic driving force.[101,102] Moreover, additives containing carboxylic, hydroxyl, carboxylate, phosphonate, sulfonate, and amino groups induce the preferential formation of metastable polymorphs, such as vaterite. By changing the concentration of the additive, molecular weight, and the number of functional groups, the growth rate, crystalline nature, particle size, and stability of the crystals can be controlled.[100,103] Furthermore, the size and porosity of the $CaCO_3$ crystals, particularly vaterite, can be adjusted without any additives, simply by changing the hydrodynamics (way of mixing the reactants, intensity of agitation,[104–106] or *via* the application of US[86,107,108]).

(1) Concentration of reactants

The initial concentrations of the reactant salts (Ca^{2+} and/or CO_3^{2-}) affect the polymorphic selection, size, shape, surface charge, and hydrophilicity of the resultant $CaCO_3$ particles, either *via* their instantaneous mixing or *via* the controlled addition of one component.[76,97,101] For example, submicron vaterite particles have been synthesized from saturated Na_2CO_3 and $CaCl_2$ solutions in the presence of ethylene glycol (EG) *via* dropwise precipitation, which allows variation in the Ca^{2+} concentration of the solution at each moment of the reaction.[76] These techniques affect the crystallization process of $CaCO_3$ by promoting the formation of new nucleation centers instead of providing the conditions for crystal growth. Such a reduced growth rate leads to a decrease in the rate of vaterite recrystallization, resulting in the formation of vaterite particles with spherical or ellipsoidal morphology. Moreover, in the presence of EG and with a controlled Ca^{2+} ion addition rate, the size of such vaterite particles can be controlled. A high concentration of CO_3^{2-} leads to the formation of anisotropic rhomboidal and ellipsoidal morphology, while a low concentration results in the formation of isotropic spheroids.[115] Furthermore, an excess of Ca^{2+} or CO_3^{2-} in the system has multiple impacts on the reaction. An excess of CO_3^{2-} accelerates the reaction and results in $CaCO_3$ particle formation in the early stages, while an excess of Ca^{2+} slows down the process of particle formation and promotes the growth of spheroidal $CaCO_3$ particles.[25]

(2) pH

The precipitation and dissolution of $CaCO_3$ in aqueous solution is a process in which CO_3^{2-} reacts with Ca^{2+} (eqn (1)):

$$Ca^{2+}(aq) + CO_3^{2-}(aq) \leftrightarrow CaCO_3(s) \tag{1}$$

This equilibrium is defined by the thermodynamic solubility product of the respective $CaCO_3$ polymorph (K^0_{sp}), but as a consequence of the removal of CO_3^{2-} from solution (addition in the case of dissolution), new equilibria are instantaneously established among the other ionic species in solution. Thus, even in the simplest systems, such as precipitation initiated by mixing $Ca(OH)_2$ and carbonic acid,[116] or the dissolution of pure $CaCO_3$ in water, in which only the constituent ions (Ca^{2+}, CO_3^{2-}) and the products of the autoprotolysis of water (H_3O^+, OH^-) enter or leave the solution, five additional ionic species (H^+, OH^-, HCO_3^-, Ca^{2+}, and CO_3^{2-}) make a significant contribution to the overall equilibrium of the solution. In a pH ranging from moderately acidic to basic, the equilibria among the relevant ionic species can be described by the respective equations and equilibrium constants (K_x),[117] as follows (eqn (2)–(8)):

$$H^+ + OH^- \leftrightarrow H_2O \quad (K_w) \tag{2}$$

$$CO_2(g) \leftrightarrow CO_2(aq) \leftrightarrow H_2CO_3(aq) \quad (K_H) \tag{3}$$

$$H^+ + CO_3^{2-} \leftrightarrow HCO_3^- \quad (K_1) \tag{4}$$

$$H^+ + HCO_3^- \leftrightarrow H_2CO_3^0 \quad (K_2) \tag{5}$$

$$Ca^{2+} + CO_3^{2-} \leftrightarrow CaCO_3^0 \quad (K_{CaCO_3}) \tag{6}$$

$$Ca^{2+} + HCO_3^- \leftrightarrow CaHCO_3^+ \quad (K_{CaHCO_3^+}) \tag{7}$$

$$Ca^{2+} + OH^- \leftrightarrow CaOH^+ \quad (K_{CaOH^+}) \tag{8}$$

If in the above-mentioned $CaCO_3$ precipitation system the charge balance and mass balance equations of all carbonic and Ca^{2+} species are considered, as well as the ionic strength and the respective approximations for the determination of the non-ideality of the solution, the concentrations and reactivities of all of the species in the solution can be calculated. The supersaturation state of the system, with respect to a specific polymorph, can also be estimated, according to eqn (9):

$$S = [(a(Ca^{2+})\cdot a(CO_3^{2-}))/(K^0_{sp})]^{1/2} \tag{9}$$

where S is the saturation ratio, $a(Ca^{2+})$ and $a(CO_3^{2-})$ are the activities of the Ca^{2+} and CO_3^{2-} ions, respectively, and K^0_{sp} is the thermodynamic solubility product constant. Consequently, the progress of the $CaCO_3$ precipitation dissolution reaction can be followed by measuring the pH ($pH = -\log a(H^+)$), while from these data and known initial experimental conditions, the kinetics and the mechanisms of the process can be determined with relative precision at any given moment.[118,119]

It is obvious from the above-mentioned explanation that the initial pH can be clearly correlated with the composition and stability of the solution (supersaturation or undersaturation), which is, in turn, a key parameter for the determination of physical, chemical, structural, and/or morphological properties of the $CaCO_3$ precipitate. However, to draw consistent conclusions about the role of the initial pH, other relevant parameters (concentrations and the ratio of reactants, hydrodynamics, temperature, presence of additives, and aging time, *etc.*) should be considered.[88,120–122] To this aim, Trofimov *et al.*[95] suggested that an increase in pH from 7 to 11 may lead to the precipitation of vaterite, which was explained by the observations of alterable supersaturation and increased CO_3^{2-} content, but that the addition of negatively-charged inorganic or organic substances appeared to have the same effect. Moreover, Džakula *et al.*[122] showed that in systems in which the supersaturation, ionic strength, ratio of the activity of the constituent ions ($a(Ca^{2+})/a(CO_3^{2-})$), and the type of stirring were identical that the calcite content increased with an increase in the pH from 8.5 to 10.5, while in the same systems that were magnetically stirred with the pH controlled at 8.5 and 9.0, the precipitated product was almost entirely vaterite. The morphology of the resultant vaterite was observed to continuously change with increasing pH. Similarly, in precipitation systems designed to produce vaterite, $CaCO_3$ formation is accelerated in the presence of increased concentrations of CO_3^{2-} ions, in particular, at pH >10.5, and it was demonstrated that spheroids, ellipsoids, or toroids can be specifically prepared *via* careful control of such parameters as the concentrations of the initial reagents, their ratio, reaction time, and organic additives.[25]

Transformation of vaterite morphology, from an almost spherical assemblage of primary NPs (5–10 nm) to hexagonal platelets (1–2 μm) and single crystals has been observed in an ammonia diffusion method.[127] During this process, the pH, and consequently the supersaturation, continuously increased as a result of the decomposition of NH_4HCO_3 and thus led to the diffusion of NH_3 into a $CaCl_2$–$NaHCO_3$ salt solution. It was also deduced that the existence of NH_3 significantly affected the initial polymorph composition of the $CaCO_3$ precipitates: high percentages of calcite were formed at low NH_3 diffusion rates, whereas vaterite became the major phase when the NH_3 diffusion was rapid and NH_3 reached a concentration of >0.02 mol L^{-1}.

(3) Reaction temperature

Temperature affects any precipitation, including the precipitation of $CaCO_3$, in two ways.[1] First, the rate constants of the nucleation and growth of a specific polymorph are influenced as indicated by the Arrhenius equation, which assumes their exponential relationship to temperature. Second, it has been observed that the solubility of different $CaCO_3$ polymorphs and hydrated forms in water varies as a function of temperature as reflected by the changes of their solubility products (K_{sp}) within a defined temperature range (Fig. 2 and Table 2).[97,102,123] Except for ikaite, all K_{sp} values continuously decrease with increasing temperature. The only difference is that the K_{sp} for ikaite has an opposite trend and changes more remarkable upon the changes of the temperature, primarily as a consequence of a large number of hydration water molecules in the crystal lattice.[124] The calculated solubilities of polymorphs and hydrates (c_s), in water and in closed precipitation systems, at 25 °C, are directly compared in Table 2. It is worth noting that although the effect of temperature on the solubility and subsequently on the formation of the polymorphic phases of $CaCO_3$ cannot be simply evaluated without considering other parameters, a general tendency can still be observed. In addition, precipitation diagrams of $CaCO_3$ polymorphs, which cover a broad span of initial concentrations and temperatures, ranging from the freezing to boiling points of water, have been also constructed.[128,129] Such diagrams provide a basis for explaining the nature of the polymorphs precipitated in both inorganic and biological environments, and help to predict, design, and control the synthesis of $CaCO_3$ particles.

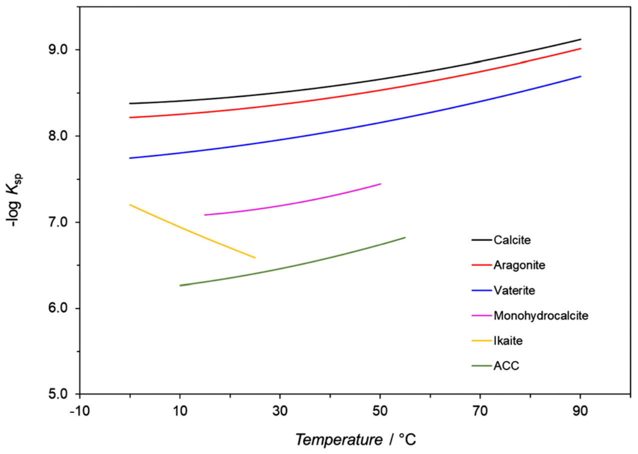

Fig. 2 Minus log of values of thermodynamic solubility products (K_{sp}) of $CaCO_3$ polymorphs and hydrates as a function of temperature. The data in the figure comes from ref. 123–126.

Recently, aragonite has been found to be the dominant polymorph obtained at temperatures of >75 °C and a wide range of supersaturations.[129] At moderate temperatures (50 °C) and low supersaturation, vaterite, aragonite, and calcite phases were observed to precipitate, while at high supersaturation, aragonite and calcite were the dominant phases. At low temperatures (25 °C) at Ca^{2+} concentrations ranging from 0.002 M to saturation, vaterite and calcite phases precipitated, while near to the freezing point of water, no precipitation occurred at 0.002 M and only the calcite phase precipitated at high concentrations. A similar tendency has been observed for temperature combined with other experimental parameters: at low temperatures and high ionic strengths, the precipitation of metastable ikaite and vaterite is favored, whereas at near-freezing temperature under highly alkaline conditions (pH 13.4), only ikaite is formed.[15,130] Moreover, it is known that aragonite, which is slightly less stable than calcite, precipitates at a higher temperature.[23] Since calcite is the only thermodynamic phase formed at ambient temperatures and pressures, the range of temperatures at which it forms in combination with many other parameters is relatively wide because all metastable phases finally transform into calcite, as predicted by Ostwald's law of stages.[98]

However, deviations from the above-mentioned empirical rules have been observed. In a double injection system in which $CaCl_2$ and NH_4HCO_3 solutions were mixed at a range of

Table 2 Thermodynamic solubility products of $CaCO_3$ polymorphs and hydrates as a function of temperature

$CaCO_3$ modification	Expression	Temperature range/°C	c_s (25 °C)/mg dm^{-3}	Ref.
Calcite	$\log K_{sp} = -171.9065 - 0.077993T + 2839.319/T + 71.595 \log T$	0–90	12.29	117
Aragonite	$\log K_{sp} = -171.9773 - 0.077993T + 2903.293/T + 71.595 \log T$	0–90	14.20	117
Vaterite	$\log K_{sp} = -172.1295 - 0.0779933\,T + 3074.688/T + 71.595 \log T$	0–90	22.22	117
Ikaite	$\log K_{sp} = 0.15981 - 2011.1/T$	0–25	125.97	124
Monohydrocalcite	$-\log K_{sp} = 7.050 + 0.000159 \cdot t^2$	15–50	56.06	125
ACC	$-\log K_{sp} = 6.1987 + 0.005336 \cdot t + 0.0001096 \cdot t^2$	10–55	168.73	126

ACC – amorphous $CaCO_3$; c_s – solubility; K_{sp} – thermodynamic solubility product of respective modification; T – absolute temperature/K; t – temperature/°C.

temperatures from 30 °C to 80 °C, vaterite and aragonite phases with various structures and morphologies were predominantly synthesized.[131] In particular, lamellar vaterite particles; a mixture of vaterite, aragonite, and traces of calcite; and aragonite whiskers were formed at 30–40 °C, 50–70 °C, and 80 °C, respectively. The formation of aragonite in the form of elongated needle-/rod-like or whisker-like morphologies with high surface energy, at high temperatures, was attributed to the increased energy of the reactive environment. However, the predominant formation of lamellar vaterite at temperatures up to 60 °C was explained as being due to a decrease in $[CO_3^{2-}]/[Ca^{2+}]$ in line with an increase in the temperature. However, pure vaterite ($\geq$99 wt%) was prepared at high temperatures (up to 60 °C) in systems in which the reactants were slowly mixed and then intensively stirred (600 rpm).[132] The synthesis of pure vaterite under such circumstances was attributed to hydrodynamic conditions, under which increased local supersaturation effects and the formation of the precursor phase (ACC) were avoided.

Besides polymorphic selection, the temperature may also significantly affect the morphology and particle size distribution of precipitates. For example, according to a recent study from Sovova *et al.*,[133] when concentrated aqueous solutions of 0.33 M $CaCl_2{\cdot}2H_2O$ and 0.33 M Na_2CO_3 were mixed in a vessel from 10 °C to 50 °C, the particle size of the vaterite increased linearly with the increasing temperature. A significant change in shape was observed over a temperature range of 20–45 °C; spherical vaterite particles were prepared, which then transformed from spheres to cauliflower-like shapes and then to croissant-like shapes. This change of vaterite particle shape was attributed to the increased diffusion of the Ca^{2+} and CO_3^{2-} ions with increasing temperature and the decreased solubility of $CaCO_3$, leading to an acceleration in the $CaCO_3$ crystallization.[133] The shape of vaterite particles, for example, changes from smooth spheres at 25 °C to cauliflower-like particles at 40 °C or 50 °C, in the systems in which the initial concentrations of the reactants (0.1 M $Ca(NO_3)_2$ and Na_2CO_3) and the stirring speed (1500 rpm) were kept the same.[134,135] Upon an increase in the temperature, the overall transformation of vaterite to calcite is reduced, due to an increase in the growth rate of vaterite. However, in this case, the particle size distribution at 40 °C was found to be similar to that at 25 °C, indicating that the nucleation rate is virtually unaffected by temperature. In contrast, in a study[121] in which an ethanol/water mixture was used with fixed initial concentrations of the reactants, only vaterite precipitated in the range of 0 °C to 100 °C and an increase in reaction temperature evidently led to a decrease in the particle size distribution and changes in morphology. This effect was attributed to the difference in the nucleation rate of the $CaCO_3$ particles and the evaporation rate of ethanol at different temperatures, which is a trend that was the opposite to previously drawn conclusions about the role that temperature plays in $CaCO_3$ precipitation.

In a precipitation system in which the temperature was varied together with the use of different organic additives, Altay *et al.*[136] found that rhombohedral calcite particles were formed within a temperature range of 30–50 °C. At temperatures of >50 °C, calcite particles tended to agglomerate, while their surfaces and edges showed serious defects. At 80 °C and 90 °C, the formation of branch-like aragonite, with different aspect ratios, was observed. The importance of the role played by the organic additive in combination with temperature was also demonstrated in a system in which $CaCO_3$ was precipitated as a result of the slow addition of Na_2CO_3 into a solution of $CaCl_2$ containing diethylenetriaminepentaacetic acid (DTPA) over a temperature range of 60–230 °C.[137] The results of product analyses were seemingly surprising, since the presence of DTPA in solution promoted the formation of pure aragonite at <100 °C, while pure calcite formed at 100 °C and 130 °C, and pure vaterite formed at 230 °C.

The interactions between the dominant experimental parameters, such as the temperature and presence of an inorganic additive, have been described in a publication by Fermani and coworkers,[138] in which the influence of Mg^{2+} (additive concentration) on the aggregation and morphology of precipitated aragonite crystals at different temperatures (40 °C, 60 °C or 80 °C) was investigated. Different from some earlier investigations, aragonite precipitated in a chemical system in which Mg^{2+} acted specifically as a crystal growth modifier, rather than polymorph selector. Indeed, the results showed that an increase in Mg^{2+} concentration favored the aggregation of aragonite crystals in spherulites, while by increasing the temperature, the crystals showed a more regular morphology and rough spindle-like appearance (at 40 °C), later converting into needle-like structures (at 60 °C and 80 °C). In addition, the increase in the Mg^{2+} concentration favored the sharing of (110) faces among the crystals and the appearance of (001) faces.

(4) Additives

Since the properties of dispersed solid phases, particularly the particle size distribution, morphology, and polymorphism are determined during the early stages of $CaCO_3$ formation, the critical question is how the additives control the nucleation process of $CaCO_3$.[91,139] CNT assumes that stochastic collisions of constituent ions take place in supersaturated solutions, and that thermodynamically unstable pre-critical nuclei are formed, which spontaneously grow into a crystalline phase after reaching a post-critical size. The size of the critical nuclei is dependent on supersaturation. A substantial point of CNT is the assumption that the nuclei exhibit all of the macroscopic and interfacial properties of the respective solid phases. However, the so-called pre-nucleation cluster (PNC) pathway assumes that the constituent ions form stable PNCs, which undergo aggregation and formation of larger liquid intermediate phases, with their final dehydration and solidification into amorphous phases and/or crystals.[80] The PNCs are thermodynamically stable solutes with no phase interface and form independent of the level of supersaturation. Therefore, to discern the mechanism of action of different classes of additive molecules with $CaCO_3$ minerals, as well as their interactions with precursors or intermediates that are postulated to exist during the early stages of mineralization, different experimental and/or computer modelling techniques, have been used and described in the literature.[81,92,140]

However, the interaction of additives with the solid phase may take place during the crystal growth process, in which already-formed $CaCO_3$ particles come into contact with the supersaturated solution. The additives thus may either inhibit or promote the growth and change in the morphology of the $CaCO_3$ precipitate.[28] Indeed, the additive molecules can interact with the $CaCO_3$ surface *via* different mechanisms, changing the growth kinetics of the respective faces, or the surface energy.[141] The additive molecules can strongly bind to the surface of the material or its crystal edges, and depending on the extent of the interactions and their surface concentration, growth can be slowed down or even completely disrupted at a given supersaturation level. When the additive molecules are adsorbed at growth sites for a short residence time, the growth is reduced. The additive molecules can also be incorporated into the crystal lattice during growth, distort the $CaCO_3$ crystal structure, and consequently increase the free energy, which is manifested as an increase in solubility.[141] Finally, certain types of additive molecules, typically surfactants, can lower the interfacial or step edge energy by adsorbing to surfaces or step edges.

Attention in recent studies has been given to controlling the growth rate, crystalline nature, stability, particle size, and surface morphology of $CaCO_3$ in the presence of low and high molecular weight additives containing carboxyl, hydroxyl, sulfonate, and amino groups.[95] In particular, additives such as DTPA,[137] para-aminobenzoic acid (PABA),[142] sodium dodecyl sulfate (SDS),[143] sodium dodecyl sulfonate (SDSN),[144] poly(acrylic acid) (PAA),[145] PEG,[143] poly(sodium-4-styrenesulfonate) (PSSS),[25,145] poly (allylamine hydrochloride) (PAH),[146] poly(vinylsulfonic acid) (PVSA),[107] and polyvinyl pyrrolidone (PVP)[144] have been used to control the synthesis of $CaCO_3$. Typically, polyelectrolytes interact with Ca^{2+} ions and provide active sites for the nucleation of $CaCO_3$ and subsequent agglomeration into MNPs. They can also stabilize nonequilibrium morphologies by changing the relative growth rates of different crystal faces *via* molecular interactions with specific crystallographic planes, resulting in the modification of the surface energy and/or the growth of $CaCO_3$ crystals.[115,144]

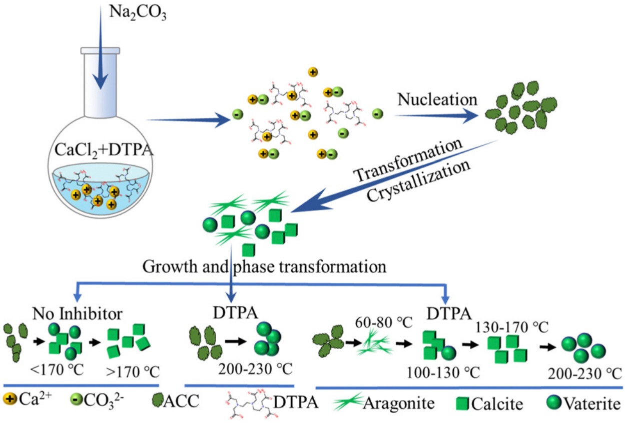

Fig. 3 Schematic diagram showing the processes of $CaCO_3$ precipitation, crystallization, and phase transformation in the presence of DTPA over a temperature range of 60–230 °C (designed and illustrated by the authors of the present Review based on the study reported in ref. 137). DTPA: diethylenetriaminepentaacetic acid.

Clearly, the temperature and initial concentration of reactants and additive are relevant precipitation parameters that may cause the formation of different precursor phases. However, it is worth noting that in complex $CaCO_3$ precipitation systems, the subtle interplay of kinetics of nucleation, crystal growth, and dissolution also have a significant influence on the $CaCO_3$ precipitates. In addition, the overall aging time of the systems should be considered. To obtain an in-depth understanding of such complicated precipitation and related influential parameters, consistent conditions including those mentioned above and hydrodynamic conditions need be experimentally used, which remains a tough task. Using a high concentration of reactants, high temperature and highly-charged additives, the understanding of the role of the transformation/stabilization of unstable polymorphs and the formation of specific morphologies has been to some degree revealed. For example, $CaCO_3$ was precipitated from $CaCl_2$ and Na_2CO_3 solutions in the presence of DTPA over a temperature range of 60–230 °C (Fig. 3).[137] Structural analysis of the final precipitate showed that pure aragonite was formed at <100 °C (Fig. 3 and 4A, B), while calcite was formed in the range of 100–130 °C (Fig. 3 and 4C, D). Vaterite nucleation was observed to commence at 150 °C, with a steady increase in its mole fraction observed and this was in line with an increase in temperature (Fig. 4E and F), while pure vaterite was formed only at 230 °C (Fig. 4G). Such experimental results of a DTPA system highlighted the possible tendency for vaterite to be kinetically stabilized by the presence of additives in the range of 200–230 °C, whereas in the absence of DTPA, below 150 °C, ACC was converted into vaterite and rapidly transformed into calcite through dissolution–recrystallization (Fig. 3). The vaterite observed in the presence of DTPA in the range of 150–230 °C was due to the formation of precursor of metastable vaterite and the transformation of precursor of stable calcite (Fig. 3). It can be assumed that the formation of vaterite was attributed to the transformation of the existing polymorph of calcite. However, it is worth noting that, for revealing the exact transformation mechanisms in such complex $CaCO_3$ precipitation systems, the appropriate sampling and structural analyses of the solid phases need be performed during the nucleation, crystallization and transformation. In addition, the consistent hydrodynamic conditions need be applied in experiments at low and high temperatures, and the aging times should be identical, in order to make the general conclusions about the formation mechanism. These remain a challenging task. However, the structural analysis of solid phases during precipitation in similar systems showed that, initially, the amorphous phase precipitated, which subsequently transformed into the most stable calcite phase *via* an intermediate vaterite phase (Fig. 3).[146,147] Such experimental results of a DTPA system highlighted the possible tendency for calcite to transform into vaterite in the range of 200–230 °C (Fig. 3).

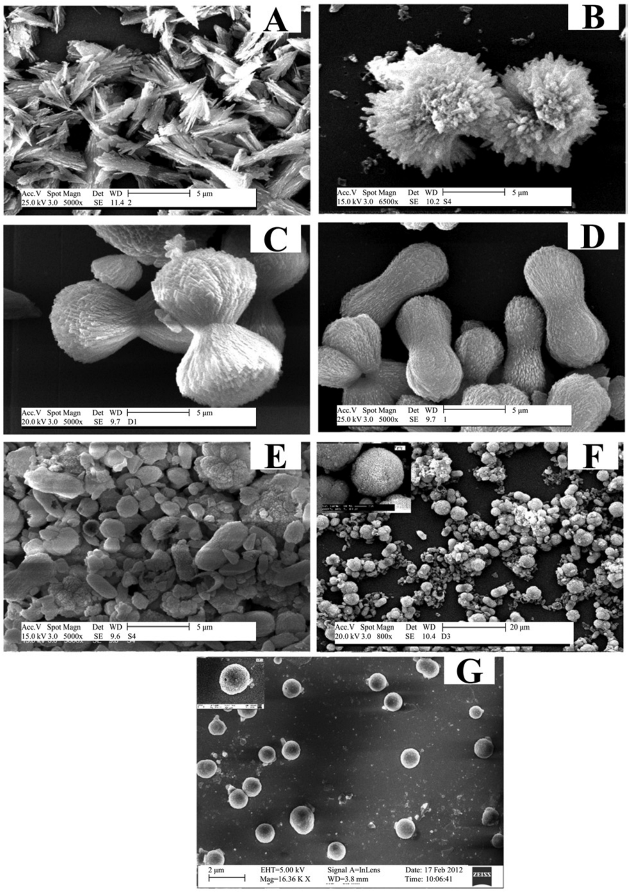

Fig. 4 SEM images of $CaCO_3$ synthesized at different temperatures in the presence of DTPA. (A) 60 °C, (B) 80 °C, (C) 100 °C, (D) 130 °C, (E) 170 °C, (F) 200 °C, and (G) 230 °C. Reprinted from ref. 137. Copyright (2013), with permission from Elsevier.

Additionally, $CaCO_3$ polymorphs were precipitated over a range of temperatures in a precipitation system in which the pH and solvent were altered in the presence of PABA as a structure-directing agent.[142] PABA features a benzene ring on which carboxylate (–COOH) and amino groups (–NH_2) are attached, which makes the overall charge of this molecule susceptible to pH. At pH <7, PABA is positively charged due to the protonation of an amino group, and the formation of calcite was observed. At pH >7, the carboxylate groups were deprotonated and PABA competed with CO_3^{2-} to bind Ca^{2+} ions. Under such conditions, the precipitate consists of calcite as the minor phase and vaterite as the major one. Pure vaterite was obtained when a water–methanol mixture was used as a solvent at pH = 8. To synthesize predominantly nanosized metastable vaterite particles, Nagaraja and co-workers introduced the negatively-charged polymeric additive PVSA into a $CaCl_2$–Na_2CO_3 system.[107] Besides the reaction temperature and the order of reagent addition, the study emphasized the decisive effect that the PVSA concentration has on the size and stability of vaterite. In this process, PVSA plays a dual role: it interacts with Ca^{2+} ions *via* ionic interactions, thus slowing down the nucleation rate, as well as preventing their aggregation into MPs. In addition, the transformation of vaterite into calcite was prevented by PVSA.

Furthermore, through the regulation of organic additives or templates, porous $CaCO_3$ microspheres with various crystal polymorphs and morphologies can be obtained. In this aspect, recently, negatively- and positively-charged biodegradable and non-biodegradable polymers have been used to control the synthesis of $CaCO_3$.[145] The polymers are initially incorporated during the fabrication of the $CaCO_3$ crystal matrix and then entrapped inside microcapsules. For example, negatively-charged PSSS having long hydrophilic was adsorbed on the surface of $CaCO_3$ MPs and was observed to prevent re-crystallization in a similar manner to that of positively charged PVSA.[107,145] Consequently, the shape of porous $CaCO_3$ MPs of vaterite and calcite phases were shown to remain unchanged after six months of storage in water. This indicates that the $CaCO_3$ MPs coating was stable, independently from the charge of the polymer. Such high stability in water of the $CaCO_3$ MPs with different surface charge is very important for layer-by-layer assembly processes. In contrast, spherical vaterite MPs prepared and stabilized in the presence of positively-charged PAH transformed into rhombohedral calcite microcrystals after several weeks of storage in water at room temperature due to the occurrence of recrystallization.[145] In addition, it was found that negatively-charged PAA has a strong effect on the electrostatic stability of $CaCO_3$ particles by preventing their growth, resulting in the formed $CaCO_3$ particles being smaller (400–600 nm) than particles produced using PSSS (600–1.1 μm).[145]

An additional strategy for the preparation of $CaCO_3$ with specific properties is to use different classes of organic additives in the Ca^{2+}–CO_3^{2-} system. For example, Ji *et al.*[143] investigated polymer–surfactant mixtures of PEG and SDS as a template for the controlled formation of hollow $CaCO_3$ microspheres, wherein it was found that PEG strongly interacts with anionic SDS and forms complex micelles, which then act as a chemical microenvironment for the nucleation and growth of $CaCO_3$. SDS provides a nucleation site for the crystallization of the solid phase, due to its interactions with Ca^{2+} in solution. Specifically, no hollow microspheres were obtained when SDS or PEG2000/10 000 were used alone, while the addition of a PEG2000–SDS or PEG10 000–SDS mixture into the Ca^{2+}–CO_3^{2-} system resulted in the formation of hollow calcite and vaterite crystals or hollow rhombohedral calcite crystals, respectively. The variation in molecular weight of the polymer also drastically changes the morphology and polymorph composition of the precipitate. Similarly, when using a mixture of PVP and SDSN as a template in an Na_2CO_3/$CaCl_2$ system at 50 °C, hollow microspheres consisting of calcite and vaterite were prepared,[144] whereas the combination of PAA/SDSN and Na_2CO_3/$Ca(NO_3)_2$ at 80 °C resulted in the formation of calcite hollow microspheres.[100]

2.1.2 Solid–liquid–gas carbonation. CO_2 carbonation is a cost-effective and facile route by which to produce $CaCO_3$ MNPs that exhibit high purity on a large scale, particularly considering that CO_2 is readily available on-site *via* the calcination of limestone. Inherently, solid–liquid–gas carbonation involves the dispersion of solid $Ca(OH)_2$ in water *via* the bubbling of CO_2 gas into it.[148] Such carbonation involves several processes taking place simultaneously, the dissolution of $Ca(OH)_2$ and the release of free Ca^{2+}; CO_2 transfer from the gas to liquid phase and the formation of carbonic acid and its hydrolysis to CO_3^{2-}; and finally; a chemical reaction between the constituent ions. The reaction may be tuned using suitable organic additives or surfactants to manipulate the type, particle size, and morphology of the precipitate.[77,149] Typically, calcite is the most common $CaCO_3$ phase that is formed *via* solid–liquid–gas carbonation. It is thermodynamically the most stable modification at room temperature and pressure, and, consequently, at lower supersaturation conditions (lower driving force for formation of solid phase), it is directly formed by homogeneous or heterogeneous nucleation. On the other hand, at higher supersaturation conditions and in the absence of precipitation inhibitors, initially formed precursor phases, such as ACC or vaterite, transform into calcite *via* a solution-mediated process after a certain period of time.[98] Either in the presence or absence of organic additives or surfactants, the morphologies, polymorphism, and particle size distributions of the precipitated $CaCO_3$ are strongly influenced by operating conditions such as temperature, suspension density, the flow rate of CO_2 gas, pressure, and stirring intensity.[33,150]

Typically, in a solid–liquid–gas reaction system, the reaction temperature influences the solubility, ionic diffusion, and supersaturation of $Ca(OH)_2$ and CO_2. Upon an increase in temperature, the dissolution of solid $Ca(OH)_2$ is increased, while that of CO_2 is decreased.[151] Recently, a new low-temperature dry ice carbonation approach was proposed for the preparation of calcite NP and porous vaterite microspheres, wherein the dry ice acts as both a source of CO_2 and a coolant.[152] Since the formation of $CaCO_3$ is an exothermic process, the decrease in temperature in this process shifts the equilibrium toward the products.[152,153] At low temperature, the nucleation dominates over the crystal growth, which enables the formation of more and considerably smaller $CaCO_3$ NPs than during high-temperature synthesis.

Generally speaking, a key to preparing $CaCO_3$ NPs is high supersaturation, which is beneficial for the nucleation process, while low supersaturation promotes crystal growth.[154] In addition, intensification of mixing and mass transfer processes are appropriate for increasing supersaturation in a solid–liquid–gas carbonation system.[33] The polymorph distribution of the precipitate can be controlled through the selection of the solvent of the system. Typically, calcite NPs have been obtained in water, while vaterite microspheres have been reported to form in a 75% methanol–25% water mixture.[152]

Since organic additives promote the absorption of CO_2 gas into aqueous solution, a variety of compounds have been used to control the polymorphism of crystal phases and morphologies of $CaCO_3$.[155] The majority of the studies conducted found that the interactions of the functional moieties of the additives, such as amine, carboxyl, hydroxyl or ether groups, play significant roles in the precipitation/crystallization processes. These functional groups not only may interact with OH^-, H_3O^+, CO_3^{2-}, HCO_3^- or Ca^{2+} ions present in aqueous solution, but also with the surfaces of the solid phases during the precipitation process, which in turn affects the reaction dynamics and overall crystallization process of the system.[155] Specifically, $CaCO_3$ crystals have been found to precipitate from $Ca(OH)_2$ suspensions and CO_2 in the presence of aliphatic organic additives such as amines, diamines, and amino acids, which was attributed to be due to the alkyl chain length in the aliphatic part of the additive molecules.[155] Consequently, the successive dissolution/recrystallization process is slowed in aqueous systems due to the adsorption of these organic additives on crystal surfaces, but also on reactants and intermediates. Not only polar interactions from hydrophilic functional groups, but also van der Waals interactions from hydrophobic alkyl groups, play important roles in the above-mentioned phase transformation.

In the presence of select organic additives, the formation of $CaCO_3$ NPs with enhanced hydrophobicity typically proceeds in several steps: the nucleation of the NPs, their aggregation, and their final templated crystallization. For example, mixed polyethylene glycol phosphate (PGP) and stearic acid (SA) in a $Ca(OH)_2$ slurry could play a synergistic role in this process.[156] During the nucleation process, SA and PGP promote a certain preferential orientation at the $Ca(OH)_2$–$CaCO_3$–CO_2 interfaces. Specifically, SA molecules are adsorbed on surfaces, while soluble PGP exists in the form of micelles and free PGP molecules. The free PGP molecules act as templates for the subsequent crystallization process. During PGP aggregation, hydrogen bonding form between the O of PGP and surface –OH groups of the $CaCO_3$ crystals, resulting in their accretion and the formation of well-oriented polycrystalline aggregates. $CaCO_3$ particles crystallize at the nucleation sites provided by SA and grow along the PGP chains, thereby leading to the formation of chain-like or rod-like $CaCO_3$. To synthesize hydrophobic $CaCO_3$ NPs with different morphologies *via* the carbonation of a suspension of $Ca(OH)_2$ with a CO_2/N_2 gas mixture and by varying the octadecyl dihydrogen phosphate ($C_{18}H_{37}OPO_3H_2$) concentration, Wang *et al.*[149] proposed that Ca^{2+} in (001) stereochemical (spindle-like) calcite layers might specifically interact with $C_{18}H_{37}OPO_3H_2$ to form P–O–Ca bonds. In this way, a number of calcium phosphate (CaP) precursor sites create favorable conditions for the nucleation and growth of $CaCO_3$, as Ca^{2+} is located almost in the same lattice positions in the (001) layers, alternating with layers of CO_3^{2-} in calcite. The pseudohexagonal net of $C_{18}H_{37}OPO_3H_2$ has a suitable inter-headgroup space, which matches the distance between the coplanar Ca^{2+} ions on the (001) face in calcite.[157] In addition to geometric matching, the stereochemical arrangement of phosphate functional groups induces the nucleation of calcite due to the tridentate arrangement of P–O simulating the oxygen positions of CO_3^{2-} lying parallel to the crystal surface.

Metastable $CaCO_3$ polymorphs have also been obtained in $Ca(OH)_2$–CO_2 carbonation systems. Glycine (Gly) has been found to react with $Ca(OH)_2$ to form calcium glycinate ($(H_2NCH_2COO)_2Ca$).[158] In this way, monodisperse spherical vaterite was prepared using Gly as an additive at room temperature and atmospheric pressure. Specifically, almost 100%

spherical vaterite was obtained by adjusting the molar ratio of Gly : Ca^{2+}. Initially, when CO_2 was dissolved into a solution of $(H_2NCH_2COO)_2Ca$, the concentration of CO_3^{2-} increased above the precipitation limit, resulting in the nucleation of a mixture of $CaCO_3$ polymorphs. On continuation of CO_2 bubbling, the concentration of Gly liberated from $(H_2NCH_2COO)_2Ca$ gradually increased. This liberated Gly predominantly adsorbed onto the crystal faces of the growing calcite, thus inhibiting its further nucleation and growth, finally resulting in the formation of spherical vaterite. Such promotion of vaterite formation in the presence of Gly can also be extended to other systems such as $CaCl_2$–$NH_3{\cdot}H_2O$–Gly–CO_2 or $CaCl_2$–Gly–Na_2CO_3 reactions.[158] In these systems, the resulting precipitate retains the polymorphic composition (vaterite), morphological characteristics (spherical particles), and size distribution, which are preserved even after thermal treatment and conversion into calcite. A model precipitation system was devised for vaterite nucleation, using an aqueous solution containing $Ca(OH)_2$, NaCl, Gly, hyaluronic acid (HA) as a template, and supercritical CO_2 as both as a reactant and a continuous (or external) phase.[161] As a result of fast CO_2 diffusion and dissolution in such a basic aqueous solution, spherical and hollow vaterite particles with an average diameter of 5 μm can be obtained. Recently, a novel free-solvent system was proposed for preparing spherical vaterite.[110] In the high-pressure CO_2 carbonation of $Ca(OH)_2$ using urea as an additive, the urea entrapped $Ca(OH)_2$ *via* its melt to stabilize the formation of vaterite with its $-NH_2$ functional group and triggered the formation of water by its decomposition to initiate the carbonation process. In this process, carbonation was initiated by the formation of Ca^{2+} and HCO_3^- upon pressurizing CO_2 and the urea-entrapped $Ca(OH)_2$, followed by the further formation of complexes between Ca^{2+} and the $-NH_2$ of urea. HCO_3^- can be easily trapped by $-NH_2$ to form an intermediate carbamate (–NHCOO–), which acts as a nucleation site for vaterite particles.[162] In this solvent-free process, $Ca(OH)_2$ completely transforms into spherical vaterite as the predominant phase without generating inorganic salts as by-products.

Furthermore, $CaCO_3$ hollow or porous microspheres can be fabricated in the presence of additives. For example, high-purity hollow calcite microspheres with a micro–nano hierarchical structure have been prepared *via* a carbonation process at 120 °C using pressurized CO_2 and the disodium salt of ethylenediaminetetraacetic acid (EDTA–2Na) as a crystal growth control agent.[74] During the pressurized-CO_2 carbonization reaction, EDTA complexed the Ca^{2+}, which become the main nucleation site. In this way, $CaCO_3$ clusters were trapped in the structure and automatically self-assembled into uniform hollow spheres. Therein, the introduction of pressurized CO_2 gas increases the solubility of CO_2 in the liquid phase, thus improving the driving force of the carbonization reaction. However, CO_2 bubbles can also act as a template for fabricating a specific type of $CaCO_3$. In a new one-step bubble-templating process to prepare hollow calcite rhombohedral NPs, no removal or decomposition of the template was unnecessary. Similarly, by bubbling CO_2 gas through an aqueous $Ca(OH)_2$ suspension, Kontrec *et al.*[163] successfully prepared hollow rhombohedral calcite NPs with a mean particle size of around 100 nm. The dissolution of the precursor ACC particles that existed in close contact with the nucleation of calcite during the early stages of the process, accompanied by simultaneous release of the trapped amount of $Ca(OH)_2$, resulted in the formation of holes with a diameter of around 50 nm at the calcite surface.

2.1.3 Water-in-oil reverse emulsion. For controlling the synthesis of $CaCO_3$ MNPs, a so-called water-in-oil (W/O) microemulsion method has captured considerable attention due to its simplicity, reproducibility, and soft-template effect.[23,112] A W/O microemulsion is a thermodynamically stable dispersion of water in oil that is formed primarily as a result of the existence of stable interfacial layers of surfactants.[164] Typically, $CaCO_3$ precipitation in such a W/O system begins with the mixing of two separate micellar solutions containing Ca^{2+} and CO_3^{2-}. After the mixing, the micelles possessing sufficient energy collide, leading to the mixing of the reactants and the onset of the reaction.[26] Meanwhile, such micellar aqueous micro-/nanodroplets can serve as micro-/nanoreactors and as a template with a tunable organic–inorganic interface. The nucleation and growth of $CaCO_3$ are restricted in such microreactors, while the agglomeration of the obtained $CaCO_3$ particles can be effectively inhibited. Hence, micro-/nano-$CaCO_3$ crystallites with a particularly narrow size distribution, polymorph content, and morphology can be synthesized.[26,164]

To elucidate the role of the micellar interface and to demonstrate that $CaCO_3$ crystallization can be triggered ''on-demand'' by removal of the organic–inorganic interface, Stawski *et al.*[26] investigated a highly supersaturated precipitation system comprising two aqueous phases (Na_2CO_3 and $CaCl_2$) and the surfactant dioctyl sodium sulfosuccinate dissolved in oily 2,2,4-trimethylpentane. After mixing two microemulsions, the inter-droplet interactions enabled the exchange of Ca^{2+} and CO_3^{2-} ions between the individual reverse micelles, leading to supersaturation with respect to $CaCO_3$ inside the water nanoreactors, thus triggering the formation of Ca–CO_3 clusters and the liquid-like $CaCO_3$ phase, which may be akin to the concept of prenucleation clusters or ion pairs, and the precipitation of a solid phase.[26] The instant formation of any solid $CaCO_3$ phase could not be obtained in spite of the high initial supersaturation ($c(Ca^{2+}) = c(CO_3^{2-}) = 0.075$ mol dm^{-3}) because each aqueous pool contained only approximately 1–3 Ca^{2+} or CO_3^{2-} ions. However, the solute $CaCO_3$ phase inside the water cores decreased the rigidity of the micellar surfactant/water interface, which promoted the aggregation of micelles and the formation of large globules. The subsequent precipitation of solid $CaCO_3$ could be initiated by the addition of ethanol, which destabilized the globules containing the Ca–CO_3 clusters. Within the clusters of the reverse micelles, the interactions between the organic interface and inorganic species compete with the purely inorganic drivers, thus changing the thermodynamics of the system and stabilizing the Ca–CO_3 clusters.[26] This observation is in contrast to fully inorganic aqueous systems, in which solids form instantaneously under the same chemical conditions. A different approach to initiate precipitation was proposed by Walsh *et al.*[159] Instead of mixing two microemulsion systems, they prepared only one aqueous saturated $Ca(HCO_3)_2$ solution and subsequently subjected it to outgassing and evaporation to remove CO_2 and consequently increase the supersaturation for $CaCO_3$ precipitation. The organic phase used was SDS in octane, and in some additionally stabilized systems dodecanol co-surfactant was added. In water/SDS/oil microemulsions, discrete spheroidal vaterite MPs with a sponge-like microarchitecture and internal patterning were obtained. The spheroids are formed *via* the initial nucleation of vaterite at the oil–water droplet interface and patterned by microbubbles of CO_2 entrapped at the surface of the water droplets (Fig. 5A).[159] The precipitation of vaterite then proceeded inwardly as the droplets progressively decreased in volume as a result of the evaporation of water and oil. However, the sulfate head groups of the applied SDS most likely specifically interacted with dissolved Ca^{2+} and promoted the vaterite formation, as confirmed by control precipitation experiments in aqueous systems.[159]

The size distribution, polymorphism, and morphology of $CaCO_3$ precipitated in reverse emulsion systems can be controlled by changing the concentration of both the reactants and surfactant, and the water: surfactant molar ratio (ω).[112] A CO_2/N_2 switchable surfactant/soft template (N'-dodecyl-N,N-dimethylethyl amidine bicarbonate) dissolved in either $CaCl_2$ or Na_2CO_3 solution has been used to form reverse micellar solutions. At high reactant concentrations, a mixture of vaterite and calcite precipitated, whereas at intermediate or low concentrations (under 0.3 M) only calcite was produced. The size of the $CaCO_3$ particles was increased as a result of the destabilization of the reverse micelles and their coalescence. The $CaCO_3$ particles show a mixed crystal type of vaterite and calcite (ω = 3.52). As ω increases, the strength of the reverse micelle interfacial membrane decreases. However, with this increase in ω, the $CaCO_3$ size becomes large and difficult to control due to the interface membrane being easily broken as a result of the collision between the reverse micelles.

To improve $CaCO_3$ precipitation in W/O emulsion processes, Badnore *et al.*[113] used US to prepare an emulsion and showed that in a model system containing aqueous Na_2CO_3 (emulsion A) and $CaCl_2$ (emulsion B) solutions and toluene stabilized by biodegradable surfactants (Tween-80 and Span-80) as a continuous phase, $CaCO_3$ NPs were synthesized with a diameter in the range of 20–30 nm (Fig. 5B).[113] Particle size distribution was more uniform in the US $CaCO_3$ system than that of $CaCO_3$ prepared *via* conventional methods of synthesis. In addition, in the US system, porous spherical vaterite was the dominant solid phase.

A nanoreactor has also been developed based on a W/O emulsion system to carry out polymerization and mineralization simultaneously, in which the crystal structure, such as the shape and polymorph, of $CaCO_3$ at the nanoscale can be tailored by changing the conditions (*e.g.*, temperature, time, and ion concentration) for crystallization and the ones (*e.g.*, initiation time and initiator concentration) for polymerization. For instance, two separate types of nanodroplets $Ca(NO_3)_2$/monomer and Na_2CO_3 were prepared and suspended in an cyclohexane/dimethicone oil phase, mixed *via* fusion and fission processes triggered by US to precipitate $CaCO_3$ only inside

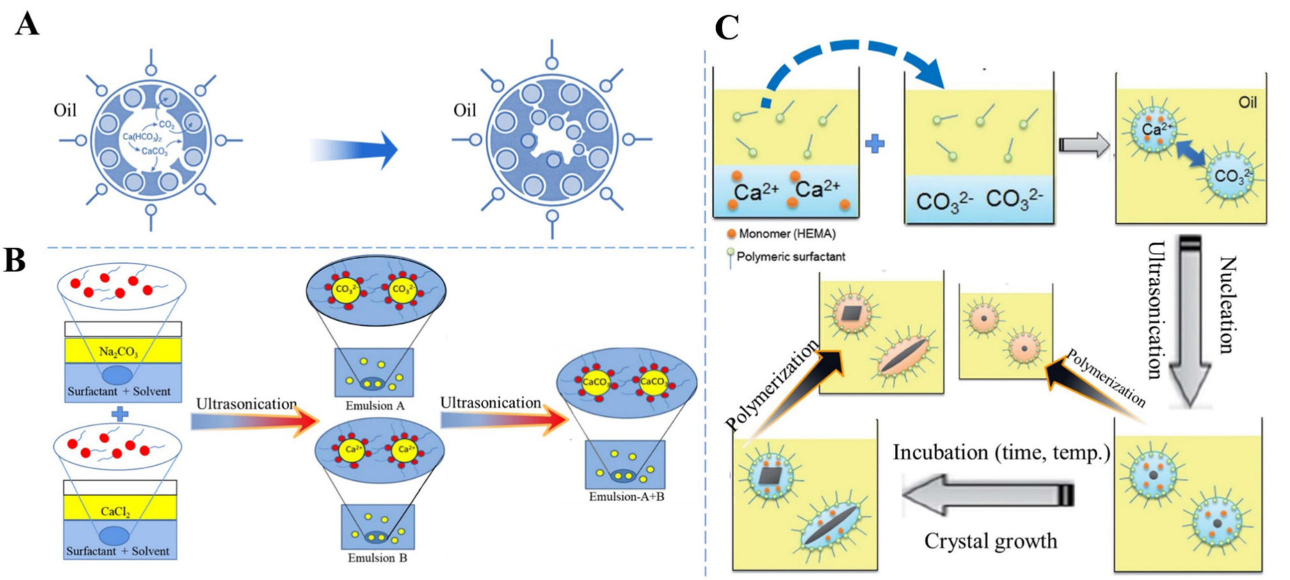

Fig. 5 Schematic diagram showing the preparation of $CaCO_3$ in W/O systems. (A) The formation of vaterite in water/SDS/oil microemulsions. Adapted and reprinted from ref. 159. Copyright (1999), with permission from John Wiley and Sons under the terms of the Creative Commons Attribution Non-Commercial (CC BY-NC 3.0) License. (B) Sonochemical synthesis of $CaCO_3$ *via* a miniemulsion technique using US. Reproduced from ref. 113. Copyright (2015), with permission from Elsevier. (C) Preparation of $CaCO_3$ NPs with a variety of crystal shapes and structures by incubation with HEMA as a monomer and subsequent polymerization inside a nanoreactor of a miniemulsion system. Reprinted from ref. 160. Copyright (2012), with permission from the Royal Society of Chemistry.

the nanodroplets (Fig. 5C).[160] In the presence of a monomer, 2-hydroxyethyl methacrylate (HEMA), spherical, rod-like, or ACC can be produced. The incubation period for nucleation and growth of $CaCO_3$ with HEMA before the polymerization of HEMA inside the nonodroplets, as well as the polymerization rate, were recognized as critical factors which manipulated the structures and polymorphs of $CaCO_3$ NPs. The crystal shape of $CaCO_3$ was found to be controllable from rod-like to spherical forms upon increasing the rate of polymerization. Enhancement of the polymerization rate by increasing the concentration of a lipophilic initiator, AIBN, allowed HEMA to rapidly inhibit crystal growth to give rise to the entrapment of small and spherical $CaCO_3$ particles.

2.1.4 Biomimetic $CaCO_3$ formation. $CaCO_3$ is the most abundant biomineral,[28] found in $CaCO_3$-based biominerals such as nacre, which is an exceptionally strong and tough material that is produced by living organisms. In addition, there are many other hierarchically-structured natural $CaCO_3$-based materials with fascinating properties, such as sea urchin spines or the coccoliths of marine algae, which comprise organic substrates and a limited number of elements under ambient conditions.[22,94] Therefore, it is not surprising that many research studies have focused on investigating $CaCO_3$ biomineralization *via* the analysis of biogenic materials, trying best to understand the crystallization mechanisms and interactions between the organic and mineral phases, and to imitate the crystallization processes.[23,28,82] To gain a general conceptual picture of biomineralization in which both synergistic and competitive effects are involved, surface chemistry and precipitation models involving the presence of additives, should be carefully analyzed.[31] Since acidic macromolecules are traditionally considered to be critical to $CaCO_3$ biomineralization, many different classes of charged small organic compounds or polyelectrolytes, such as polysaccharides, polypeptides, or proteins and different experimental strategies and conditions have been systematically applied to discern the roles they play in the biomineralization of $CaCO_3$.[165–167]

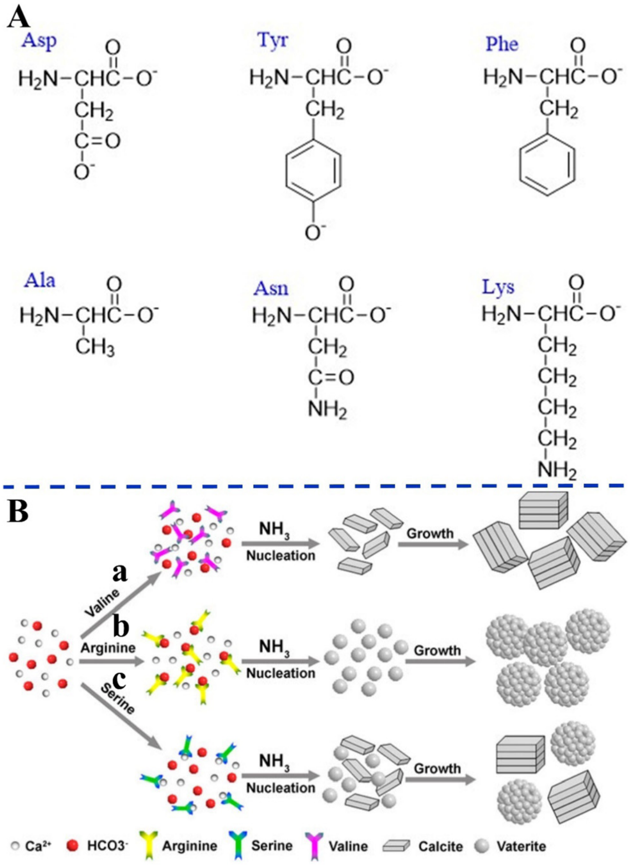

Fig. 6 Schematic diagram illustrating the effects of different amino acids on biomimetic $CaCO_3$ precipitation. (A) Amino acids with different surface charges, polarity, and side chains. (B) Schematic diagram illustrating the formation mechanisms of $CaCO_3$ in the presence of different amino acids. (a) L-Valine; (b) L-arginine; and (c) L-serine. Reprinted by permission from [Springer Nature Customer Service Centre GmbH]: [Springer Nature] [ref. 173], [Copyright] (2013).

Amino acids with different surface charges, polarity, and side chains can regulate the nucleation, growth, and crystal structure of $CaCO_3$ (Fig. 6). It has been established earlier that the intraskeletal glycoproteins associated with $CaCO_3$ biominerals are rich in side chains of carboxylated residues (*i.e.*, aspartate and glutamate) and Gly.[168] From this key information, in a pioneering study, Addadi and co-workers[169] showed that the beta-sheet conformation of the adsorbed poly-aspartate macromolecules was responsible for the epitaxial oriented growth of calcite. In another milestone work, Gower and Tirrell[170] revealed that the addition of poly(aspartate) to supersaturated solutions of $CaCO_3$ led to unusual vaterite aggregates with helical extensions, as well as distorted calcite crystals that contained spiral pits. A reductionist approach, based on high-resolution synchrotron powder diffraction and analytical chemistry, was utilized to screen the 20 most common amino acids in terms of their incorporation into calcite. This research showed that the important factors were amino-acid charge, size, rigidity, and the relative pK_a of the carboxyl and amino terminal groups. It was also demonstrated that cysteine, surprisingly, interacted very strongly with the mineral phase and therefore, like acidic amino acids, became richly incorporated.[171] By *in situ* atomic force microscope observations and molecular modelling studies of calcite growth in the presence of chiral amino acids, it was found that the enantiomer-specific binding of the amino acids to calcite surface-step edges that offered the best geometric and chemical fit changed the step-edge free energies, which in turn resulted in modifications of macroscopic crystal shape.[172] These results emphasize that the mechanism underlying crystal modifications through organic molecules will be better understood by considering both stereochemical recognition and the effects of binding on the interfacial energies of the growing crystal. In the presence of different concentrations of highly nonpolar hydrophobic L-valine (Val), positively-charged L-arginine (Arg) (Fig. 6A), and the less polar uncharged L-serine (Ser), $CaCO_3$ with different morphologies and polymorphs were synthesized *via* the diffusion of NH_3 into a saturated aqueous solution of $Ca(HCO_3)_2$ (Fig. 6B).[173]

As a result of the coordination interactions formed between the amino acids and Ca^{2+}, Ca^{2+}–amino acid complexes were first formed. Val did not affect nucleation at neutral pH, but merely changed the growth/assembly of calcite during the growth process at increasing values of pH (Fig. 6B-a). It can be speculated that this effect can be related to a change of the ζ-potential of the calcite crystal surface, which unfortunately was not reported in the paper. Without the addition of amino acids, rhombohedral calcite was predominantly produced. The effects on the nucleation were attributed to the charge of the side chains and their possible interactions with the constituent ions (Ca^{2+} or HCO_3^-) present in solution, while the effects on the crystal growth were attributed to the gradual increase in pH and deprotonation of $-NH_3$ and –OH. The strong electrostatic interactions between the positively-charged side chain of the Arg and the HCO_3^- result in the formation of a stable complex, which affects the nucleation of the $CaCO_3$ to form vaterite (Fig. 6B-b). However, with the less polar uncharged Ser, some of the Ca^{2+} form a complex with Ser, while the rest remained in the form of free ions, resulting in the simultaneous nucleation of calcite and vaterite to form the two polymorphs (Fig. 6B-c). Similarly, amino acids that have side chains with different charge and polarity under experimental conditions, such as L-aspartic acid (Asp), L-tyrosine (Tyr), Ser, L-asparagine (Asn), L-lysine (Lys), L-phenylalanine (Phe), and L-alanine (Ala), were found to significantly change the morphology and polymorph distribution of $CaCO_3$ precipitates (Fig. 6A).[30] Without the addition of amino acids, a mixture of typical calcite rhombohedral crystals and vaterite spherulites were observed. Asp contains two deprotonated –COOH groups that also cause relatively strong distortions of the calcite crystal lattice in the *c*-axis direction, which indicates Asp progressive incorporation into structure (Fig. 6A). The influences of nonpolar amino acids (Phe, Ala) on the structural and morphological properties of the $CaCO_3$ precipitates were less pronounced. The strong effect observed for polar, particularly negatively-charged amino acids (Ser, Asn, Lys), may indicate that besides the strong impact of negatively-charged side groups on the precipitation of $CaCO_3$, the hydrogen-bonding donor side-chain groups (–OH, $-NH_2$ or –CO–NH–) could also influence the interactions of the amino acids with the calcite surface (Fig. 6A).

Although the majority of studies on the role of amino acids on biomimetic $CaCO_3$ precipitation have focused on Asp and Gly, Phe, which makes up around 5% of the acid-soluble organic matrix of biomineralized structures, was also used as an organic template with the aim to induce the nucleation and growth of $CaCO_3$.[24] High concentrations of Phe have been shown to inhibit the nucleation and growth of calcite, and promote the formation of vaterite crystals with solid or hollow structures.[174] Phe is an ampholyte that can release protons as an acid and accepts proton as a base. The structure of the anionic form of Phe is generated in solution due to deprotonation at high pH. This anionic form of Phe captures Ca^{2+} *via* electrostatic interactions with $-COO^-$ and $-NH_2$ groups to form a Ca^{2+}–Phe complex. At low Phe concentration (<6 g L^{-1}), a large amount of Ca^{2+} ions promote the generation of calcite and suppress the formation of vaterite. However, as the concentration of Phe increases, a large amount of Ca^{2+}–Phe complex promotes the generation of vaterite and suppresses the formation of calcite.

Moreover, the results of the analysis of the crystal growth kinetics of a calcite seed in contact with zwitterionic model molecules with an acidic side chain, *i.e.*, Asp derivatives, ((L-Asp)$_1$, (L-Asp)$_2$ and (L-Asp)$_3$), which mimic the macromolecules found in biominerals, are a somewhat surprising and not intuitive.[167] Most binding modes between dissolved molecules and calcite surface involve a positively-charged ammonium group, although attachment *via* negatively-charged side-chain carboxylate groups has also been frequently observed. The experimentally observed values of adsorption constants and binding free energies are in good agreement with free energy profiles determined from fully atomistic molecular dynamics simulations. As these features are also precisely the active sites for crystal growth, the growth inhibition mechanism relies primarily on the blocking of these sites, preventing further incorporation of dissolved ions and thus halting further growth. Montanari *et al.*[175] concluded that Asp and its polymers (Asp_5 and Asp_n) inhibit growth, with a decreasing rate of calcite growth in line with an increase in the chain length of the amino acid.

The work on aragonite mineralization has also been inspired by the nacreous layer of marine organisms, which is the inner part of the shells of some mollusks, gastropods or cephalopods. Murai *et al.*[114] used a synthetic multifunctional β-sheet Ac–VHVEVS–$CONH_2$ peptide to act as a template for the *in vitro* biomimetic mineralization of aragonite *via* a "self-supplied mineralization" experimental setup. These synthetic β-sheet peptides formed three-dimensional (3D) nanofiber networks comprising assembled bilayer β-sheets, with His and Ser residues acting as the $CaCO_3$ source supplier to hydrolyze urea to generate CO_3^{2-} due to a charge relay effect between the His and the Ser residues. $CaCO_3$ was selectively mineralized on the peptide assembly using the generated CO_3^{2-}, thus leading to a fiber-like structure being obtained. However, in nature, biomineralization occurs in the presence of complex polypeptides, which interact with mineral surfaces electrostatically, but also stereochemical interactions and geometrical matching play critical roles in this process.[28,176] The use of poly(amino acids) as model molecules for investigating organic/inorganic interactions in $CaCO_3$ biomineralization is more appropriate than small monomeric molecular systems. A series of typical polypeptide molecule systems, including polyaspartic acid (PAsp), polyglutamic acid (PGlu), and polylysine (PLys), have been to precipitate $CaCO_3$ crystals. Specifically, the crystallization of calcite on nonpolarized and polarized calcite single crystal substrates in the presence of PLys has a significant effect on the morphologies of the precipitate. At low PLys concentrations (<0.5 mg 10 mL^{-1}), rhombohedral calcite crystals form and aggregate with an island structure, while at high PLys concentrations (1.0–3.0 mg 10 mL^{-1}) calcite aggregates elongated in the direction perpendicular to the substrate were obtained.[174] When $CaCO_3$ was precipitated in a double-diffusion setup in agar hydrogel in the presence of PLys and PAsp, nucleation was found to occur heterogeneously on the polypeptide assemblies.[82] In the presence of PLys alone, calcite and vaterite adopted dendritic and spherulitic morphologies, respectively, and calcite was the major component of the mixture. In the presence of PAsp alone or a mixture of PLys and PAsp, the precipitate comprised only hollow calcite spherulites, the cores of which might contain polypeptide assemblies and $CaCO_3$ of poor crystallinity. It is interesting to note that the crystal growth of a calcite seed in the presence of PLys, PAsp, and PGlu suggests a dual action of PLys in its interaction with calcite.[177] PLys interacts non selectively, electrostatically adsorbing at the crystal surface, thus increasing the rate of calcite growth at low concentrations and inhibiting it at high concentrations. Strong interactions between the crystal surfaces and PAsp are thought to be coordination between the carboxylic groups of the side chain of the PAsp (β-pleated sheet) and the Ca^{2+} cations of the calcite surface. Kim *et al.*[166] investigated the interactions between $CaCO_3$ and low-charge hydroxyl-rich macromolecules, by adsorbing proteins and homopolymers onto gold NPs, and concluded that the observed strong interactions may be similar to those observed in living organisms. Such complex systems also hold potential for synthesizing a class of unique single-crystal nanocomposites, which may be used as thermoelectrics, optoelectronics, catalysts, paints, and coatings or as drug delivery systems.

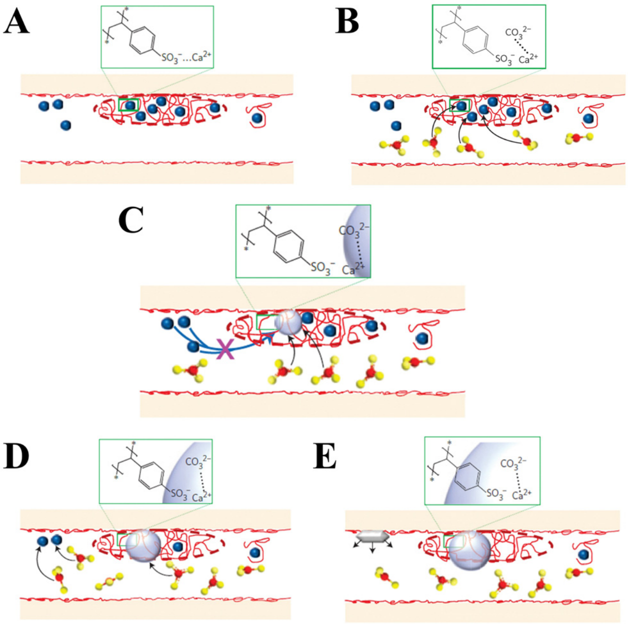

Fig. 7 Schematic diagram illustrating the mechanism of $CaCO_3$ mineral formation in the biomimetic matrix (blue dots: Ca^{2+}; red dots: SO_3^-; red and yellow dots: CO_3^{2-}). Reprinted by permission from [Springer Nature Customer Service Centre GmbH]: [Springer Nature] [ref. 178], [Copyright] (2015).

In addition to peptides, polypeptides, and proteins, other macromolecules have also been found to play a role in directing biomineralization and affect growth habits, phase selection, and precipitation kinetics. For example, Smeets *et al.*[178] showed that polystyrene sulphonate (PSS) may mimic sulfated carbohydrates, which have been found to be responsible for the nucleation of aragonite in the nacreous layer of mollusk shells. The proposed mechanism of $CaCO_3$ mineralization assumes that free Ca^{2+} is attracted to the SO_3^- group of PSS *via* electrostatic attraction, which leads to a locally high Ca^{2+} concentration in immobilized Ca–PSS globules (Fig. 7A). After the diffusion of CO_3^{2-} into Ca–PSS globules, it binds with Ca^{2+} and replaces the weaker SO_3^-/Ca^{2+} interaction (Fig. 7B), therefore meaning that supersaturation increases and reaches the critical value for the nucleation of ACC (Fig. 7C). When the free Ca^{2+} in the globules is depleted, ACC stops growing, but due to the continuous generation of CO_3^{2-} the supersaturation in the solution continues to rise to the level required for the nucleation of vaterite (Fig. 7D). The vaterite continues to grow until the free Ca^{2+} in the solution is depleted below the solubility values typical for a given set of conditions (Fig. 7E). In this model, the strong Ca binding capacity of SO_3^- generates the high local supersaturation required for nucleation of $CaCO_3$.

As for the role played by common functional groups in $CaCO_3$ biomineralization, Deng *et al.*[179] proposed that nucleation of $CaCO_3$ occurs mainly *via* an ion aggregation mechanism at the –COOH groups of self-assembled monolayer surfaces, resulting in the direct formation of calcite. At the surfaces of –OH and $–NH_2$ groups of self-assembled monolayers, the synthesis of the $CaCO_3$ phase proceeds *via* the formation of $CaCO_3$ clusters, with their aggregation in solution and final adsorption onto the surface. It was also found that the surfaces of the –OH and $–NH_2$ groups of self-assembled monolayers promote the formation of vaterite with preferred crystalline orientations, while neither amorphous nor crystalline $CaCO_3$ modification has been observed on the $–CH_3$ surface of groups. However, the interactions between the organic interfaces and $CaCO_3$ surface and their effects on $CaCO_3$ nucleation and growth could be highly complex. The polymorph distribution and precipitation rate are not equally affected by the selection of organic matrix. There are competitive or synergistic effects on nucleation and various precipitation pathways. Specifically, an organic matrix rich in ternary amines has been shown to strongly promote the nucleation of vaterite, while a carboxyl-enriched polyelectrolyte film has been found to significantly stabilize ACC in the near-surface region and equally promote the nucleation of both vaterite and calcite.[31]

2.2 Nucleation and growth of $CaCO_3$

Regardless of the methods used for producing $CaCO_3$ in a controllable way, understanding and utilizing the nucleation of $CaCO_3$ polymorphs and their hydrated phases are crucial, yet challenging. The nucleation of $CaCO_3$ is a process of forming a new phase in the form of small embryos from a homogeneous system (solution), the free energy of which is higher than that of the emerging new phase.[141] Superficially, the driving force is expressed as the supersaturation of the solution, *i.e.*, the ratio of the actual concentration of the solute and its equilibrium solubility at a given temperature. Nucleation is not only the initial stage of $CaCO_3$ crystallization, it consequently determines some important properties of the obtained crystal phases, including the polymorph selection or particle size distribution.[180] Following nucleation, the growth of crystals occurs *via* the adsorption of constituent units onto the existing crystal face, with their two-dimensional migration toward the growing steps, and final integration into the kink positions. The nucleation is an elemental process and must be controlled in to produce crystals with desired shapes, sizes and textures.[22,176]

The mechanisms of the nucleation and growth of $CaCO_3$ polymorphs, with and without additives, remain debatable.[28,80] A basic theoretical model, also known as CNT, describes the formation of $CaCO_3$ nuclei as being *via* the association of constituent units (ions) that overcome a free-energy barrier at a critical nucleus size (Fig. 8A-a).[91,181] However, recent experimental evidence from advanced experimental techniques (cryo-transmission electron microscopy) and molecular simulation, have suggested that the crystallization process may proceed by pathways not as those predicted by CNT.[92,140] The crystallization process of $CaCO_3$ crystals is based on NPs rather than constituent units (ions) as in the CNT, a particle-based theoretical model referred to as NCNT. NCNT assumes that the nucleation and growth of $CaCO_3$ are mediated by NPs, clusters, liquid-like precursors or oligomers (Fig. 8). After nucleation, the primary $CaCO_3$ NPs assemble into iso-oriented crystals (Fig. 8A-b). When polymers or other additives are present, the primary $CaCO_3$ NPs transform into mesocrystals (Fig. 8A-c). However, $CaCO_3$ biominerals can be formed *via* stable PNCs, with aggregation into the ACC phase occurring *via* collision and coalescence, before transformation into a crystal phase (Fig. 8A-d).[80] These above-mentioned crystallization pathways can only be interpreted using NCNT.

Stable prenucleation ionic clusters form even in undersaturated solution.[80,183] For example, in a study by Gebauer,[80] clusters formed at pH = 9.00 were found to have an average size of ∼70 ions, which is larger than predicted by CNT. Nevertheless, the structure of the PNCs is pH-dependent, with their precise structure remaining unknown, although it is apparent that they exhibit ''solute character''. Such assumption means that hydration energy taking solvent effects into account can be ascribed to clusters, but not the surface tension, as predicted by CNT. Consequently, PNCs are formed with a negligible activation barrier, which can be matched with thermal energy. The activation barrier of PNCs is much lower than the critical nucleation enthalpy predicted by CNT for the formation of metastable clusters. However, Demichelis *et al.*[184] concluded, using computer modelling with potential measurements, titration, and speciation calculations, as well as after structural analyses of quenched precursors, that the PNCs of $CaCO_3$ are ionic polymers comprising Ca^{2+} and $CO_3{}^{2-}$ ions held together only *via* ionic interactions, with a dynamic topology consisting of chains, branches, and rings. The structural forms of the prenucleation clusters can be affected by the concentration of ions, as it results in a change in the frequency of collisions between the ions/ion pairs and clusters. In terms of a liquid-like precursor in the nucleation and growth of $CaCO_3$, a polymer-induced liquid precursor (PILP) is a typical case (Fig. 8B).[28] The additives incorporated in the PNCs or nano-droplets kinetically stabilize the PNCs against dehydration or the nano-droplets against aggregation and/or coalescence so that they grow into macroscopic PILPs. For instance, it has been found that the PILP of $CaCO_3$ forms in the presence of charged polymers, then coalesces into thin films on a substrate (Fig. 8B), finally transforming into calcite or vaterite.[93] In most cases, the formation of $CaCO_3$ involves multiple nucleation and

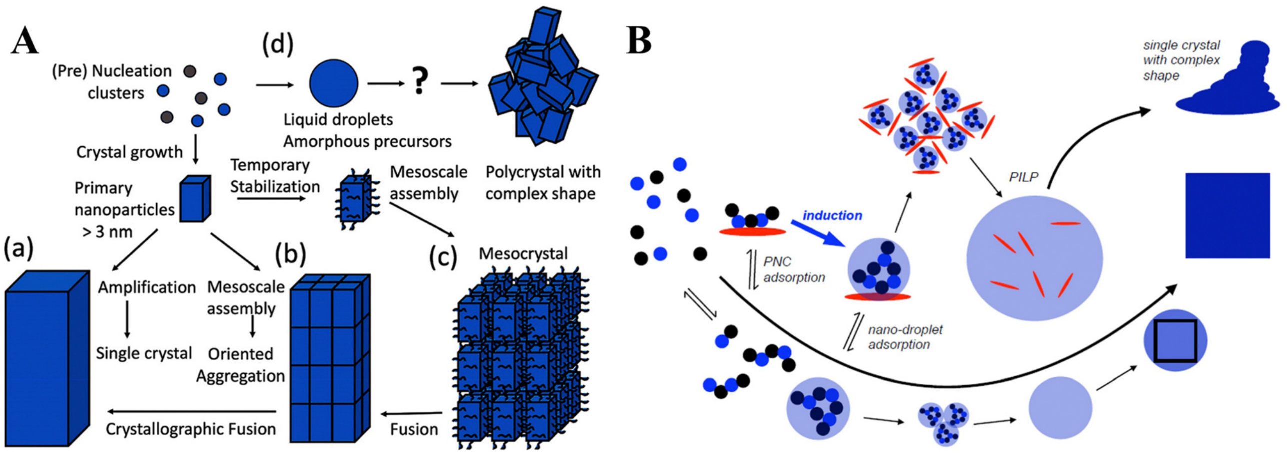

Fig. 8 Schematic diagram of the crystallization pathway of $CaCO_3$. (A) The classical and nonclassical crystallization pathways of $CaCO_3$. (a) Classical crystallization pathway involving layer-by-layer growth *via* ion ($Ca^{2+}/CO_3{}^{2-}$) addition. (b) Oriented aggregation of primary NPs forming iso-oriented crystals. (c) Mesocrystal formation *via* the self-assembly of primary NPs covered with organics. (d) Crystallization *via* liquid droplets or amorphous precursor phases. Adapted and reprinted with permission from ref. 181 and 182. Copyright (2003), with permission from John Wiley and Sons under the terms of the Creative Commons Attribution Non-Commercial (CC BY-NC 3.0) License. (B) The mechanism of nucleation according to the PNC pathway with the effects of PILP and nano-droplet adsorption by an additive (red ellipsoid). Reprinted from ref. 139. Copyright (2018), with permission from MDPI under the terms of the Creative Commons Attribution License.

growth pathways. Various distinct precrystalline entities, liquid droplets, amorphous precursors and mesocrystals are present during the crystallization of $CaCO_3$.[182,185] For example, for sea urchin larval spicules growth, the transformation of a granular phase of ACC into calcite single crystals *via* a complex and tortuous propagation pathway by secondary nucleation. The crystallization of ACC leads to the final mesocrystalline structure.[187,188]

As discussed above, both the PNC- and PILP-mediated nucleation and growth pathways of $CaCO_3$ involve an amorphous phase, followed by the formation of $CaCO_3$ polymorph crystals. An as-yet unanswered question is how ACC transforms into crystalline $CaCO_3$. According to a study by Bots *et al.*,[186] the ACC crystallizes to vaterite in three stages (Fig. 9). During the first stage, hydrated and disordered ACC forms, which then rapidly transforms into a more ordered and dehydrated form of ACC. Meanwhile, vaterite grows *via* a spherulitic mechanism,[189] followed by an intermediate stage during which the vaterite continues to form from the dissolving ACC. The third stage is controlled by the Ostwald ripening of the vaterite particles, *via* a dissolution reprecipitation mechanism.[190] The further ripening of the vaterite is easily displaced by a dissolution–reprecipitation transformation and finally, calcite is formed. Such a pathway provides a comprehensive description of the abiotic mechanism of the crystallization of pure ACC.

When monomer and oligomer molecules are involved in $CaCO_3$ nucleation processes as important precursors in polymers, these oligomer structures can produce $CaCO_3$ with a specific structure. For example, an ionic polymer-like structure of $CaCO_3$ can be generated by bubbling CO_2 into an ethanol solution containing $CaCl_2{\cdot}2H_2O$ and triethylamine (TEA, $(C_2H_5)_3N$).[89] In this reaction, ethanol as the solvent favors the a formation of a hydrogen bonding between the nitrogen of TEA and the protonated carbonate (Fig. 10A). The capping with TEA stabilizes the precursors, namely ionic $(CaCO_3)_n$ oligomers, in which n represents the number of Ca^{2+}:$CO_3{}^{2-}$ units (Fig. 10A). The value of n within the ionic oligomers can be tuned to between 3 and 11 by altering the molar ratio of Ca^{2+} to TEA (Fig. 10B), where the $(CaCO_3)_n$ oligomers possess a rod-like structure with a length of 1.2 nm (Fig. 10C). After removing the TEA, the oligomers change their shape from chain-like to branch-like structures (Fig. 10D). Pure monolithic ACC can be rapidly constructed *via* the crosslinking of the ionic oligomers with the increased density of the oligomers (Fig. 10E), which is then subsequently transformed into bulk crystals with a continuous and oriented internal structure (Fig. 10F). The oligomeric precursors can be molded into shapes to enable the construction of calcite rod arrays, which show the advantage of integrating classic inorganic and polymer chemistry in their crystallization.

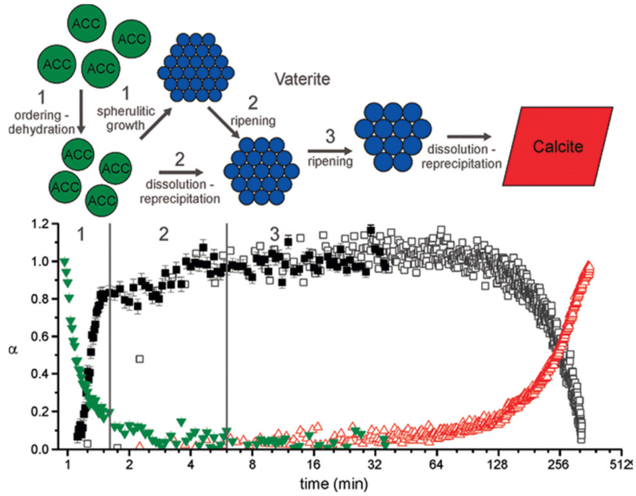

Fig. 9 Schematic representation of the proposed multistage ACC → vaterite → calcite crystallization pathway (top) with the underlying combined reaction progress (the green triangles and full black squares represent ACC and vaterite, and the open squares and red triangles represent vaterite and calcite). Reprinted with the permission from ref. 186. Copyright (2012) American Chemical Society.

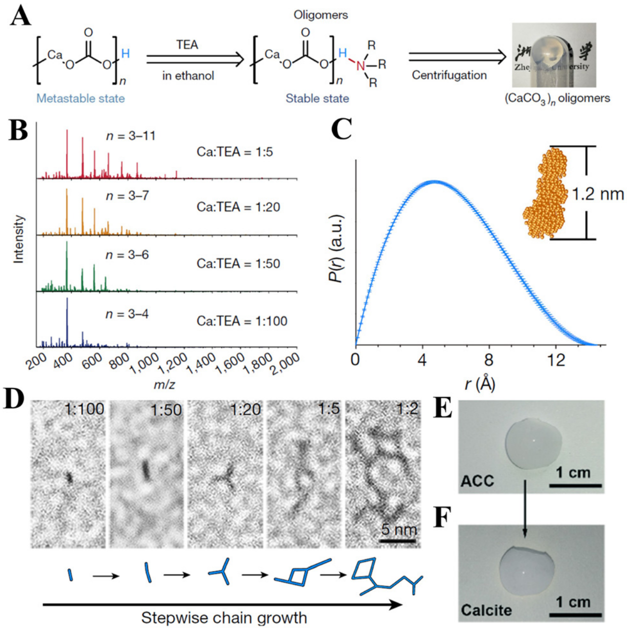

Fig. 10 Schematic diagram of the oligomers involved in the crystallization of $CaCO_3$. (A) Scheme of the capping strategy and reaction conditions for producing $(CaCO_3)_n$ oligomers (left) and a photograph of the gel-like oligomers (right). (B) Mass spectra of $(CaCO_3)_n$ oligomers with different Ca : TEA molar ratios. (C) Pair-distance distribution function (PIJr) of the $(CaCO_3)_n$ oligomers. The inset shows the shape simulation of the oligomer. (D) High-resolution TEM images of $(CaCO_3)_n$ oligomers grown at different Ca : TEA ratios from 1 : 100 to 1 : 2. (E) Photographs of monolithic ACC prepared from $(CaCO_3)_n$ oligomers. (F) Photographs of monolithic calcite prepared from monolithic ACC. Reprinted by permission from [Springer Nature Customer Service Centre GmbH]: [Springer Nature] [ref. 89], [Copyright] (2020).

3. Surface modification of $CaCO_3$ NPs

$CaCO_3$ NPs possess polar hydroxyl groups (–OH) on their surface, which endow them with hydrophilic and oleophobic properties.[27] In addition, owing to their high surface energy, $CaCO_3$ NPs are more prone to agglomerate *via* intermolecular forces and electrostatic interactions.[191] For the same reason, the $CaCO_3$ NPs are also not easy to uniformly disperse in either hydrophobic polymer or organic polymer matrices.[192,193] Surface modification can be undertaken to overcome these issues and enhance the affinity and interfacial incompatibility of $CaCO_3$ with organic molecules.[194] The surface modification of $CaCO_3$ NPs can be achieved by surface grafting and surface coating.[27] Surface modifiers such as coupling agents, organic acids, anionic and cationic surfactants, and inorganic SiO_2 have also been used to modify the surface of $CaCO_3$ NPs.[195] Furthermore, the surface modification process can be intensified by ball milling. Such auxiliary mechanochemical treatments not only help to break up the $CaCO_3$ aggregates, but also enhance surface reactivity of the $CaCO_3$ NPs toward the modifiers.

3.1 Organic modification of $CaCO_3$ NPs

It has now been found that the –OH groups on the surface of $CaCO_3$ NPs can react with many types of organic modifiers, such as silane coupling agents, titanate coupling agents,[196] aluminate coupling agents,[197] unsaturated organic acids, and anionic and cationic surfactants. Silane coupling agents such as vinyltrimethoxysilane, triethoxyvinylsilane, γ-aminopropyl triethoxysilane, and methyltrimethoxysilane and γ-methacryloxypropyl trimethoxysilane have been used to modify the surface of $CaCO_3$ NPs. Surface modification of $CaCO_3$ NPs with these silane coupling agents occurs *via* condensation-like polymerization, in which the hydrolysis product of $CaCO_3$ is used as monomer and a silane coupling agent as a chain terminator,[198] where the [–Si–OR] group (where R is the methyl or ethyl of the molecular end of the coupling agent) of the silane coupling agent reacts with the –OH group on the surface of the $CaCO_3$ NPs. Consequently, the silane coupling agents are grafted onto the surface of the $CaCO_3$ NPs at one or several sites. The bulky organic moiety grafted onto the surface of the $CaCO_3$ NPs lowers the surface-free energy of the $CaCO_3$ NPs and generates surface exclusion and steric hindrance effects, thereby preventing the $CaCO_3$ NPs from aggregating. For example, the silane coupling agent methyltrimethoxysilane ($CH_3Si(OCH_3)_3$) hydrolyzed in water to form $CH_3Si(OH)_3$, which then reacted with the –OH groups on the surface of the $CaCO_3$ NPs to form Ca–O–Si bonds (Fig. 11).[199] With an increase in the methyltrimethoxysilane concentration, a greater number of methyltrimethoxysilane molecules was then grafted onto the surface of the $CaCO_3$ NPs. As a consequence, the grafted $CaCO_3$ NPs exhibited a higher hydrophobicity than unmodified $CaCO_3$ NPs and have potential applicability as a stabilizer for foams and emulsions. The use of US irradiation to uniformly disperse the agglomerated $CaCO_3$ NPs into the reaction mixture reduces their surface energy, along with reducing the electrostatic forces of attraction in the material. When treated with triethoxyvinylsilane using a US-assisted technique, the surface modification of the $CaCO_3$ NPs proceeds *via* the reaction of each Si–OC_2H_5 group with the –OH groups on the surface of the $CaCO_3$ NPs.[200]

The surface of $CaCO_3$ NPs can be modified with methacrylic,[201] myristic,[202] oleic acids,[203] and SA.[204] These acids are made up of two parts: a hydrophobic tail and a hydrophilic head. The carboxyl groups of these acids interact with Ca^{2+} *via* an electrostatic attraction, creating a hydrophobic monolayer over the $CaCO_3$ NPs.[204] Modifications to the $CaCO_3$ NPs can be made by so-called "dry" or "wet" methods.[204] In the "dry" method, the SA is added to the filler while it is maintained in a dispersed state, usually by high shear mixing at a melting temperature that matches or exceeds that of SA. In this process, it is assumed that surface dissociation of molten SA occurs, where the H^+ cations go to a surface CO_3^{2-} to form surface HCO_3^-, and the stearate anions are chemisorbed by surface Ca^{2+} cations (Fig. 12A).[205] Due to the steric effects of hydrocarbon chains of chemisorbed stearate (their oblique conformation), part of the Ca^{2+} surface centers are blocked, affecting the degree of surface dissociation of molten SA, or the amount of the chemisorbed SA. SA molecules can be adsorbed or bonded to the surface of calcite *via* hydrogen bonding or as dimers due to the interaction of hydrocarbon chains (Fig. 12A). In the "wet" method, a double electric layer consisting of the Stern and diffused layer was formed on the calcite/water boundary. The micelles of SA were formed, and SA of free molecules or molecules from micelles dissociated in a basic aqueous solution (pH = 10.14) (Fig. 12B). The stearate anions can be chemisorbed on primary centers of Ca^{2+} ions or participate in ion exchange with OH^- ions from secondary surface centers (Fig. 12B). With increasing adsorption density, vertical orientation of the adsorbed SA and stearate anions with respect to the surface is achieved, and the *trans*-conformation of the hydrocarbon chains is maintained due to the interactions between the hydrocarbon chains and the thickness of the double electrical layer. Such a double electric layer further influences the interaction of calcite with stearate anions and SA molecules (Fig. 12C).

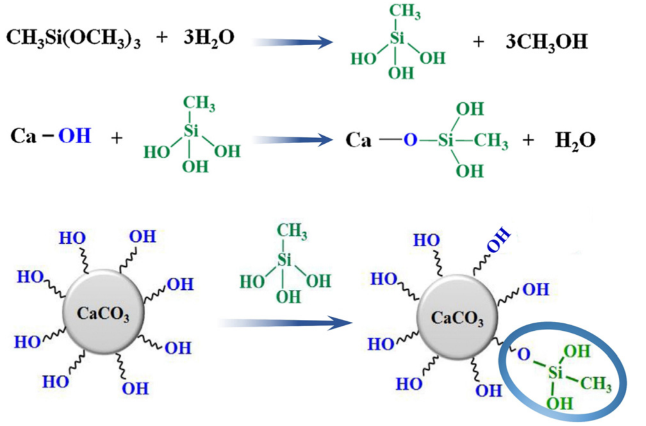

Fig. 11 Schematic diagram showing surface modification of $CaCO_3$ NPs by reaction with methyltrimethoxysilane. Reprinted from ref. 199. Copyright (2019), with permission from Elsevier.

In addition to the above-mentioned "dry" or "wet" processes, a mechanochemical method involving the simple mixing of $CaCO_3$ and organic acids *via* ball milling can be applied to modify the surface of $CaCO_3$ NPs. The ball milling technique not only reduces the size of the $CaCO_3$ NPs *via* mechanical

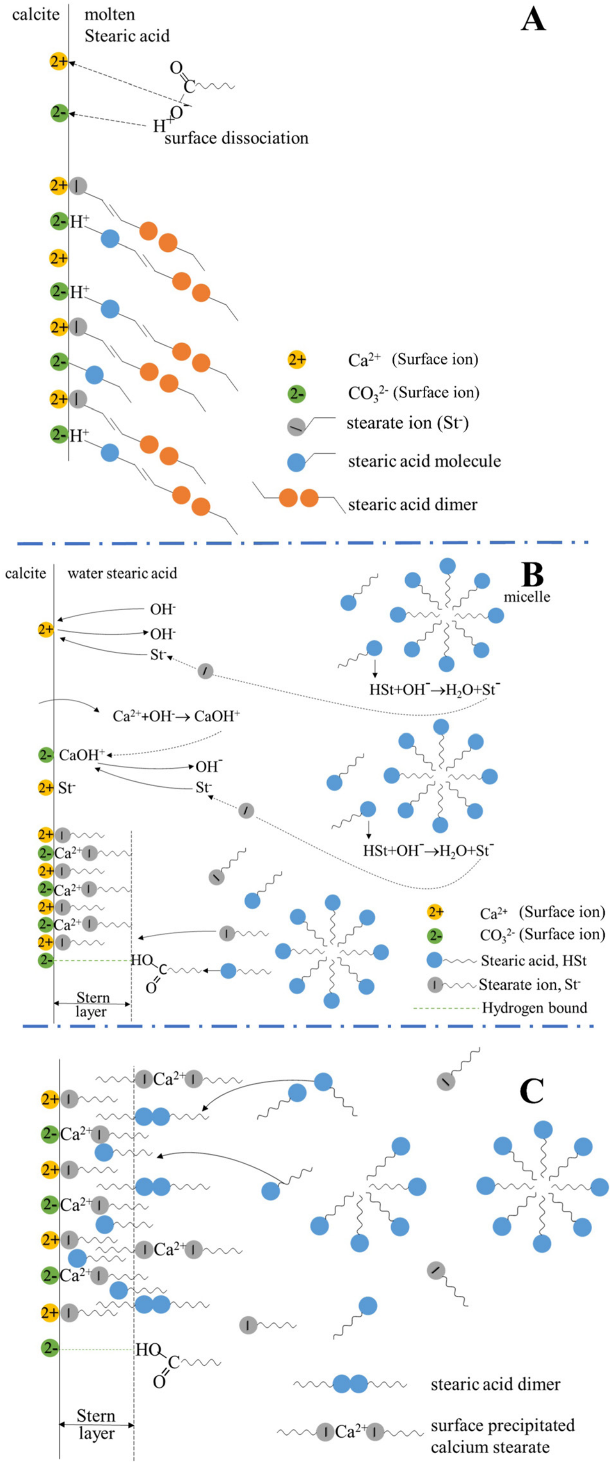

Fig. 12 Schematic diagram illustrating the surface modification of calcite using stearic acid (SA) *via* the "dry process" and "wet process." (A) Surface dissociation of molten SA on calcite and possible structure of the adsorbed layer on calcite in the "dry" method. (B) Interaction in the calcite/water and SA system, and the structure of the Stern layer in the "wet" method at a SA concentration of $c < 1.5$ phr (phr = mass of SA (g) per 100 g of limestone, $8.8 < \mathrm{pH} < 10.14$). (C) Structure of the adsorbed layer (the Stern layer and a part of the diffuse layer) in the calcite/water and SA system at a SA concentration of $c > 1.5$ phr (pH = 8.7–8.8). Slightly modified and reprinted from ref. 205. Copyright (2013), with permission from Elsevier.

force, but also enhances the chemical activity for the attachment of modifiers to their surface.[206,207] Dry ball milling and wet ball milling have been used for the surface modification of $CaCO_3$ NPs. Dry ball milling requires high energy consumption and a long milling time, while wet ball milling requires relatively low intensity. For example, Deepika *et al.*[208] used a wet ball milling method to produce SA-modified $CaCO_3$ NPs, wherein the hydrophobicity, reactivity and dispersion of the $CaCO_3$ NPs were reported to be improved.[209] The coating efficacy has been found to correlate with respect to the reactivity of $CaCO_3$ and the modifiers in the ball milling approach.[210] Yoğurtcuoğlu *et al.*[207] also revealed that sodium oleate can be chemically adsorbed on the surface of $CaCO_3$ NPs *via* wet ultrafine grinding. In contrast, when the aqueous suspension of fatty acid salt (a mixture of RCOONa, sodium stearate or sodium oleate, RCOONa) was added into an aqueous suspension of $CaCO_3$, the former dissociated sodium and carboxylate ions ($RCOO^-$), which in turn then hydrolyzed and generated respective carboxylic acids (RCOOH). However, solid $CaCO_3$ NPs partially dissolved and produced Ca^{2+} and $CO_3{}^{2-}$, which hydrolyzed to $HCO_3{}^-$ and OH^-. It was suggested that the free Ca^{2+} at the surface of the $CaCO_3$ NPs reacted electrostatically with $RCOO^-$, while the OH^- reacted with RCOOH due to the formation of hydrogen bonding (Fig. 13).[193] Consequently, the $CaCO_3$ NPs convert from hydrophilic to hydrophobic *via* the adsorption of a large amount of $(RCOO)_2Ca$ organic long chains. For example, the surface modification of $CaCO_3$ NPs can be achieved using $Ca(OH)_2$ and CO_2 *via* carbonation and modified *in situ* in the presence of calcium stearate ($(CH_3(CH_2)_{16}COO)_2Ca$, $(RCOO)_2Ca$).[33] $(RCOO)_2Ca$ absorbs on the surface of the $CaCO_3$ NPs, or further adsorbs and forms a second layer over the RCOO–$CaCO_3$ NPs. It may also transfer and be adsorbed on the surface of unmodified $CaCO_3$ NPs.

Many types of anionic surfactants have been used to modify the surface of $CaCO_3$ NPs *via* physical and chemical adsorption

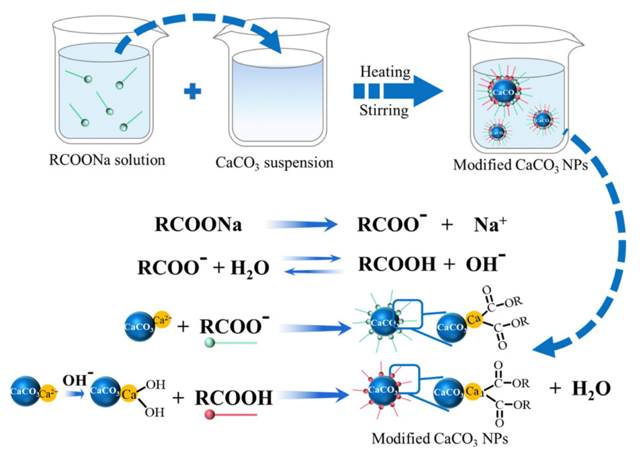

Fig. 13 Schematic diagram showing the surface modification of $CaCO_3$ NPs with fatty acid salt (RCOONa). ($RCOO^-$ adsorbed on Ca^{2+}; RCOOH adsorbed on OH^- *via* hydrogen bonding (shown in red)). Designed and illustrated by the authors of the present Review based on the study reported in ref. 193.

or chemical reactions. Anionic surfactants used to achieve this include SDS, 2-ethylhexylsulfosuccinate (AOT), fluorosurfactants (*e.g.*, Zonyl® TBS),[211] alkylbenzene sulfonic acid (ABSA),[212] and laureth sulfonic acid (LSA).[212] The electrostatic attraction between the positively-charged $CaCO_3$ NPs and negatively-charged anionic surfactant headgroups results in monolayer adsorption of the surfactant at the NP–water interface.[213] When $CaCO_3$ NPs interact with amphiphilic compounds, for example linear alkylbenzene sulfonic acid (LABSA) and branched alkylbenzene sulfonic acid (BABSA), a monolayer of the surfactant is formed on the surface of the $CaCO_3$ NPs due to electrostatic interactions and the hydrophobic effect.[212] The surface of LABSA-modified $CaCO_3$ NPs with a uniform arrangement of linear alkyl chains on it exhibits better hydrophobicity than that of BABSA-modified $CaCO_3$ NPs. Nevertheless, LABSA and BABSA are both non-biodegradation in the environment. Two types of anionic surfactants, LSA surfactants, such as magnesium laureth sulfate (LSA-Mg) and calcium laureth sulfate (LSA-Ca), have also been used for the surface modification of $CaCO_3$ NPs.[214] However, the hydrophobicity of the modified $CaCO_3$ NPs was found to be very compatible with hydrophobic polymers. A more recent study revealed that the use of an anionic fluorinated surfactant Zonyl TBS appeared to be more efficient in improving the hydrophobicity of $CaCO_3$ NPs than the use of anionic hydrocarbon surfactants such as ABSA and LSA.[211] Basically, anionic ABSA, LSA, and fluorinated surfactants exhibit similar adsorption on the surface of $CaCO_3$ NPs (Fig. 14A). In a region of low anionic surfactant concentration, with an increase in anionic surfactant concentration, the surface of the $CaCO_3$ NPs becomes increasingly more hydrophobic due to the gradual formation of a complete monolayer of an anionic surfactant on the positively-charged $CaCO_3$ NPs *via* electrostatic interactions (Fig. 14A-b). However, after that, a further increase in surfactant concentration brings about a reverse change from hydrophobic to hydrophilic due to the formation of a bilayer of surfactant molecules on the surface of the $CaCO_3$ NPs (Fig. 14A-b and c).

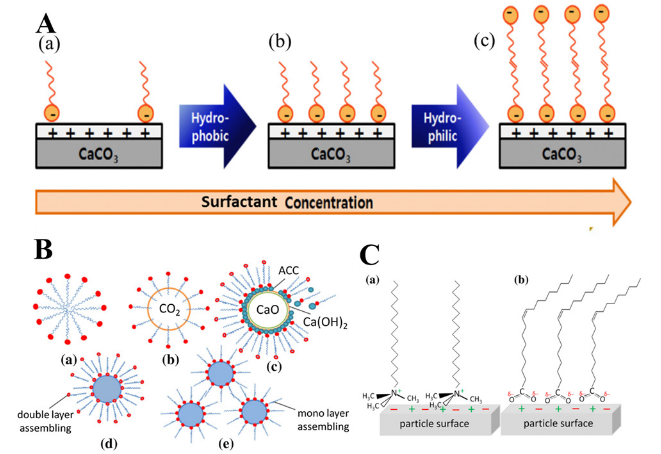

Fig. 14 Schematic diagram illustrating the adsorption behavior of anionic and cationic surfactants on the surface of $CaCO_3$ NPs. (A) The adsorption behavior of anionic ABSA, LSA, and fluorinated surfactants on the surface of $CaCO_3$ NPs. (a) Adsorption of surfactant molecules on the surface of $CaCO_3$ NPs; (b) formation of a monolayer saturated with surfactant molecules on the surface of $CaCO_3$ NPs; (c) formation of a bilayer on the surface of $CaCO_3$ NPs. Reprinted from ref. 212. Copyright (2014), with permission from Elsevier. (B) Assembly of the surfactant (CTAB and oleate) in the $CaO–CO_2–H_2O$ system; a surfactant–water, b surfactant–CO_2 bubbles, and c surfactant–CaO–$Ca(OH)_2$–ACC; d surfactant–$CaCO_3$ before filtration; and e surfactant–$CaCO_3$ after filtration and washing. (C) Interaction of (a) CTAB and (b) oleate on the $CaCO_3$ particle surface. (B and C) Reprinted by permission from [Springer Nature Customer Service Centre GmbH]: [Springer Nature] [ref. 195], [Copyright] (2015).

The interaction of $CaCO_3$ with a surfactant is remarkably affected by the size, ionic charge, and structure of the organic modifiers. A cationic surfactant reacts with negatively-charged CO_3^{2-} on the surface of $CaCO_3$ NPs. The modification can be *in situ* achieved in the process of bubbling carbonation ($CaO–H_2O–CO_2$) (Fig. 14B).[195] When CaO particles and CO_2 bubbles are introduced into an aqueous solution containing cationic surfactant (CTAB ($R–N^+–(CH_3)_3$)), a fraction of the CTAB ($R–N^+–(CH_3)_3$) assembles on the surface of the CO_2 bubbles and the $Ca(OH)_2$-covered CaO particles (Fig. 14B-a–c). An ACC shell is formed *via* reaction of the CO_3^{2-} ions with the $Ca(OH)_2$ layer on the CaO particle surface (Fig. 14B-c). The first layer of surfactant molecules adsorbs with the hydrophilic heads onto the surface of $CaCO_3$. On this first layer, the second layer of surfactant molecules is assembled, forming a double layer structure (Fig. 14B-d). In the process of surface modification, the quaternary ammonium head ($R–N^+–(CH_3)_3$) of CTAB interacts with the negatively-charged CO_3^{2-} sites on the $CaCO_3$ surface (Fig. 14C-a). In contrast, the polar carboxylate head ($–COO^-$) with high charge density of the anionic surfactant ($R\text{-}COO^-$) sodium oleate physically binds to or forms a complex with (coplanar) Ca^{2+} at the surface of $CaCO_3$ (Fig. 14C-b). The $R\text{-}COO^-$ binds more strongly to the $CaCO_3$ surface compared with $R–N^+–(CH_3)_3$, with the largest quaternary ammonium head of the four alkyl groups bound to the central nitrogen atom. Small and linear surfactants with high charge density have been found to preferentially interact with the $CaCO_3$ surface, while bulky surfactants need to structurally fit to the $CaCO_3$ surface to ensure efficient interaction.[195]

3.2 Inorganic modification of $CaCO_3$ NPs

Although the surface modification of $CaCO_3$ NPs has thus far mainly focused on organic modification, the inorganic modification of $CaCO_3$ NPs has been attempted so as to adjust their poor acid resistance and surface reaction activity.[215] The surface of $CaCO_3$ NPs modified by SiO_2 can form $SiO_2@CaCO_3$ composite NPs with a core–shell structure.[27] The SiO_2 particles are tightly bound to $CaCO_3$ *via* Si–O–Ca bonds. The product exhibits the integrated properties of SiO_2 and the $CaCO_3$ NPs, showing improved surface reaction activity and acid- and heat-resistance of the $CaCO_3$ NPs.[215] In the surface modification of $CaCO_3$ using aqueous hexafluorosilicic acid (H_2SiF_6) solution, amorphous SiO_2 was generated from the hydrolysis of silicon hexafluoride (SiF_6^{2-}), with release of F^- anions. CaF_2 subsequently precipitated from the reaction between F^- anions and Ca^{2+} cations, which originated from partial dissolution of the $CaCO_3$ surface at pH = 5–7. As a result, a layer of inorganic coating, consisting of amorphous SiO_2 and crystalline CaF_2 was formed on the $CaCO_3$ surface. No partially fluorinated $CaCO_3$ with extended structure has been detected.[215]

$SiO_2@CaCO_3$ composite NPs have been successfully prepared *via* surface deposition,[216] sol–gel,[192] and mechanical methods.[217] For example, in the preparation of $SiO_2@CaCO_3$ core–shell NPs *via* surface deposition, Na_2SiO_3 solution added to $Ca(OH)_2$ slurry was carbonized at pH 9.0 by controlling the rate of CO_2.[216] The reaction was stopped when the pH value of the system dropped to 7.0, and was then aged for 2 h to obtain $SiO_2@CaCO_3$ core–shell NPs. SiO_2 layers with a thickness of around 5 nm were observed to be coated continuously on the surface of the $CaCO_3$ core. $SiO_2@CaCO_3$ core–shell NPs can also be produced using the sol–gel method *via* hydrolysis and condensation of tetraethyl orthosilicate (TEOS) in ethanol/water under alkaline conditions.[218] A study has shown the preparation of $SiO_2@CaCO_3$ core–shell NPs *via* a mechanochemical method. In a study by Cui *et al.*,[217] hydrated SiO_2, 30 wt% sodium polyacrylate solution, and grinding media were mixed in water, and the mixture was ground for 90 min. Then, $CaCO_3$ was mixed into the mixture, kept at pH 10 by the appropriate addition of ammonia, then the mixture was ground for 40 min. The mechanochemical process activates the SiO_2 and $CaCO_3$ NPs. Under alkaline conditions, the surface of $CaCO_3$ yields Ca^{2+} and the surface of SiO_2 yields silicon hydroxyl (Si–OH). Thus, SiO_2 and $CaCO_3$ then combine *via* the reaction of their hydroxy functional groups to form $SiO_2@CaCO_3$ core–shell NPs.

$SiO_2@CaCO_3$ core–shell NPs can be further functionalized to improve surface properties and endow the inorganic components with reactivity, thus improving the dispersion of $CaCO_3$ particles and interface compatibility with organic matrices. Recently, a one-pot reaction to coat $CaCO_3$ NPs with SiO_2 and surface silanization using a bis-(γ-triethoxysilylpropyl)-tetrasulfide coupling agent has been reported.[27] In this process, water was used as a solvent for the selected neutral silica sol solution, as the thermal motion of the SiO_2 sol particles intensifies the Brownian motion at a relatively mild temperature (80 °C), increasing the probability of the occurrence of collisions between the SiO_2 and $CaCO_3$ NPs. This leads to instability of the sol system and the condensation of SiO_2 particles on the surface of $CaCO_3$ NPs to form a dense SiO_2 coating. The further surface silanization of the $SiO_2@CaCO_3$ core–shell NPs endows the $CaCO_3$ NPs with more reactive points, thus enhancing the crosslinking density of the composite.

4. $CaCO_3$-Based nanostructured biomaterials

$CaCO_3$ NPs and surface-modified derivatives prepared *via* controlled synthesis can be further engineered into a variety of $CaCO_3$-based nanostructured biomaterials (Fig. 15), which can be used in bone tissue engineering, hemostatic agents, drug/gene/protein nanocarriers, diagnostic and therapeutic agents, and theranostic nanoplatforms. Firstly, $CaCO_3$ NPs can be incorporated into a polymer matrix to generate a bioceramic that exhibits pronounced strength, excellent biocompatibility, bioactivity, and high osteoconductivity. Secondly, porous $CaCO_3$ microspheres can be combined with biomacromolecules such as collagen and chitosan (CS) to form $CaCO_3$-mineralized scaffolds and organic–inorganic hydrogels,[75,219] which have uses in bone repair, osteoregeneration, and wound dressing. Thirdly, the combination of pH-sensitive gas-generating $CaCO_3$ NPs with imaging contrast agents such as elements or organic fluorophores, bioimaging contrast agents for US imaging, MRI, fluorescence imaging, and multimodal imaging agents can be constructed for use in medical diagnosis (Table 3).[56] Fourthly, $CaCO_3$ functionalized using lipids or polymers shows enhanced physical stabilization and can act as a binding site for targeting agents to form porous or core–shell nanocarriers for use in oncosis, chemotherapy, PDT, and PTT.[220,221] In addition, pH-sensitive CO_2-generating $CaCO_3$ NPs can be loaded with anticancer drugs and imaging agents, as a designed novel nanotheranostic platform for use in US imaging-guided chemotherapy and PDT,[222,223] MRI-guided chemotherapy, and fluorescence imaging-guided chemotherapy and PDT.[42,44,55]

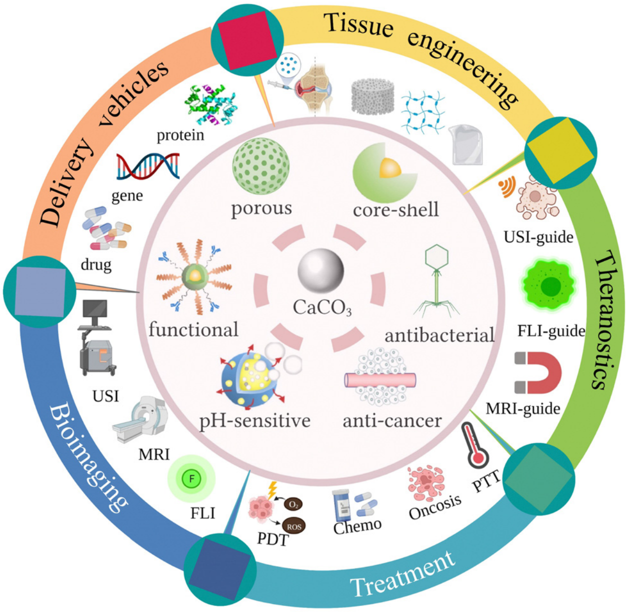

Fig. 15 Schematic diagram showing emerging $CaCO_3$-based nanostructured biomaterials (Created with https://BioRender.com).

4.1 Bone regeneration and bone tissue engineering

4.1.1 $CaCO_3$ cement and bioceramics. $CaCO_3$ has been shown to be biologically active in binding to bone *in vivo*.[224] $CaCO_3$ cements and bioceramics are characterized by their considerable compressive strength, moderate degradation rate, good cell response, and being free from any obvious drawbacks such as supply difficulties, biological variability, or risk of viral or bacterial contamination.[225] In addition, $CaCO_3$ cements

Table 3 Synthesis methods, physicochemical characterization, and therapy modalities of $CaCO_3$-based multifunctional nanocarriers for cancer therapy

$CaCO_3$-Based nanocarriers	Synthesis methods	Therapeutic compound	Physicochemical characterization	Targeting ligand	Stimulus sensitivity	Therapy modalities	Ref.
PAA/$CaCO_3$ NPs	Template method Heat treatment in a high-purity CO_2 atmosphere	DOX	Average size:120 nm DOX loading capacity: 1.18 g of DOX per g of NPs pH-sensitive sustained release	N/A	pH	Chemotherapy	49
Vaterite $CaCO_3$ nanoplate assemblies with exposed high-energy (001) facets	Solvothermal reaction of Ca $(CH_3COO)_2$ (c = 7 mM) in DMF/H_2O mixed solvent (3 : 1 v/v) at 120 °C for 6 h	DOX	Diameters ranging from 0.8 to 1.9 μm A maximum DOX loading capacity: 65% Encapsulation efficiency: 80% Sustainable release	N/A	pH	Chemotherapy	265
$CaCO_3$/rGO-TEPA NPs	Mineralized $CaCO_3$ crystals in solution with rGO-TEPA	DOX	Spherical and a few cubic shaped crystals with approximately 2–4 μm in size DOX loading efficiency: 94.7% pH-sensitive release and mild storage-release: pH 7.4 : 13.8%, pH 5.0 : 91.7%	N/A	pH	Chemotherapy	266
$CaCO_3$-HA-HB NPs	$CaCO_3$ NPs cross-linked HA through physical adsorption	HB	Hydrodynamic diameter: 410 nm Enhancement of PDT cytotoxicity to cancer cells HB loading capacity: 20 mg per g $CaCO_3$ NPs as the original concentration of HB was 2 mg mL^{-1} Cellular internalization of NPs by MCF-7 cells: 85%	HA	pH NIR	Photodynamic therapy	267
OVA@$CaCO_3$ NPs	Starch-templating method	OVA	Size: ≈500 nm The high loading rate of 19.6% Increased antigen cross-presentation Elicited CD8 T cell proliferation; Potent cytotoxic T lymphocytes responses, and excellent tumor rejection	N/A	N/A	Therapeutic vaccines	40
Fe_3O_4@PDA@$CaCO_3$/ICG NPs	Fe_3O_4 NPs: traditional alkaline precipitation method ICG: adsorbed onto PDA nanoshell through electrostatic adsorption under mildly acidic conditions established by the hydrolysis of $CaCl_2$	IGG PDA	Average hydrodynamic diameter: 134.4 nm Decomposed in response to acidic TME and triggered drug release Increased the therapeutic bioavailability Low systemic toxicity		Magnetic field NIR pH	Combinatorial photothermal/photodynamic therapy	50
NMOF@DHA@$CaCO_3$ NPs	Coprecipitation Seed-growth strategy	DHA TCPP	Average sizes: 382 ± 23 nm in length and 182 ± 37 nm in width pH-triggered dissolution of outer $CaCO_3$ mineralized layer; GSH-triggered degradation of NMOF core Ablate the tumor completely	N/A	GSH pH	Chemodynamic/oncosis/photodynamic therapy	268
$CaCO_3$@COF-BODIPY-2I@GAG NPs	Reversible imine bond formation at room temperature	BODIPY2I	Hydrodynamic diameter: 319.4 nm	GAG	NIR	Photodynamic and Ca^{2+}-overload synergistic therapy	269

Table 3 (*continued*)

$CaCO_3$-Based nanocarriers	Synthesis methods	Therapeutic compound	Physicochemical characterization	Targeting ligand	Stimulus sensitivity	Therapy modalities	Ref.
	Bonding defect functionalization method		A significantly enhanced and selective antitumor effect on the colon tumor		pH		
$Cu_2O@CaCO_3@HA$ NPs	*In situ* gas diffusion method	Cu_2O	Average hydrodynamic diameter: 180 Turn "cold" tumors "hot" by reprogramming TAMs from protumoral M2 phenotype to tumoricidal M1 phenotype	HA	H_2S pH	Photothermal/photodynamic/chemodynamic/Ca^{2+}-overload mediated therapy	270
Alg-$CaCO_3$-PDA-PGED NPs	Biomineralization	Plasmid DNA PDA	Hydrodynamic particle size: 429 nm Gene transfection efficiency with irradiation:46.10% pH-responsive strong echogenic signals	N/A	NIR pH	Dual-modal ultrasound and photoacoustic imaging-guided photothermal heating-enhanced gene therapy	271
DOX-$CaCO_3$ hybrid NPs	Block copolymer templated *in situ* mineralization approach	DOX	Mean hydrodynamic diameter: ~200 nm pH-dependent generation of the echogenic signals	N/A	pH	Ultrasound imaging-guided chemotherapy	222
Ce6–BMNs	Anionic block copolymer-templated *in situ* mineralization method	Ce6	Mean hydrodynamic diameter: 354 nm pH-dependent generation of the echogenic signals	N/A	pH	Ultrasound imaging-guided photodynamic therapy	223
Ce6@$CaCO_3$-PDA-PEG NPs	Gas diffusion procedure	Ce6; imaging ions (*e.g.*, Mn^{2+})	Average size: ~170 nm Simultaneous loading of both imaging and therapeutic molecules pH-sensitive sustained release	N/A	NIR pH	Magnetic resonance/photoacoustic imaging-guided photodynamic therapy	42

Ce6: chlorin e6; Ce6-BMNs: Ce6-loaded bubble-generating mineralized NPs; DHA: dihydroartemisinin; HA: hyaluronic acid; HB: Hypocrellin B; GAG: glycosaminoglycan; GSH: glutathione; ICG: indocyanine green; NCOF: nanoscale covalent organic framework; NIR: near-infrared light; NMOF: nanoscale metal-organic framework; OVA: ovalbumin; PAA: polyacrylic acid; PDA: polydopamine; rGO-TEPA: tetraethylenepentamine-graphene; TCPP 4,4,4,4-(porphine-5,10,15,20-tetrayl) tetrakis(benzoic acid)

exhibit excellent biodegradability and biocompatibility properties compared to other synthetic bone substitutive cements such as CaP, tricalcium phosphate, and hydroxyapatite, both *in vitro* and *in vivo*, and they can enhance gene expression in specific osteogenic markers.[226,227] Moreover, $CaCO_3$ is not only a possible calcium source for the preparation of calcium-based materials such as hydroxyapatite and other CaP salts due to its fast biodegradability,[228] but is also a functional additive that can be incorporated into CaP-based cements to improve their performances in bioresorbability and bone formation.[225,229] The slow resorption rate of bone graft substitutes, such as CaP cements and apatite, inhibits their replacement by new bone tissues and ultimate bone defect repair.[230] Biological resorption mainly depends on the solubility of the mineral components.[231] Compared to apatite (solubility constant, $K_{\mathrm{Lps}} \approx 10^{-54}$), $CaCO_3$ (solubility constant, $K_{\mathrm{Lps}} \approx 10^{-8}$) has higher solubility. It would thus be interesting to prepare cements with injectability properties, low inflammability, and improved and tunable biodegradation rates.[232]

To fabricate $CaCO_3$-based bone substitutive cements for bone regeneration, the chosen material needs to mimic the unique structure and strength of bone and exhibit bone-forming bioactivity.[233] The main bottleneck in fabricating $CaCO_3$ ceramics is the difficulty in the sintering of $CaCO_3$, as $CaCO_3$ decomposes to CaO and CO_2 between 600 °C and 700 °C. The feasibility of sintering cements entirely made of $CaCO_3$ has already been demonstrated.[225] Employing a highly reactive ACC phase and a metastable vaterite crystalline phase, a calcareous cement was prepared that during setting recrystallized in full agreement with Ostwald's rule of stages. The structural analysis of the phase composition during the setting and hardening periods provided evidence of the (re)crystallization of the initial metastable $CaCO_3$ phases mostly into aragonite and/or calcite phases. The compressive strength of the $CaCO_3$ cements ($R_{\mathrm{comp}} \leq 13$ MPa) was poor, however, such mechanical properties do not hinder the use of these materials in *in vivo* applications such as bone filling, especially in low mechanical stress locations. Such $CaCO_3$ cements release Ca^{2+} and $CO_3{}^{2-}$ ions or CO_2 during the *in vivo* biodegradation with good cytocompatibility.

To achieve satisfactory clinical use, adequate tuning of the composition of $CaCO_3$ cements is required, which requires a good understanding of their (re)crystallization to optimize

$CaCO_3$ bone cements. The adsorption of octanoic acid on the $CaCO_3$ surface within the microstructure of $CaCO_3$ cements has been shown to have no effect on the $CaCO_3$ (re)crystallization progress.[229] This observation opens up the possibility of functionalizing $CaCO_3$ cements with other biomolecules such as proteins, growth factors, stem cells or antibiotics, which may enhance the protein adhesion, bactericidal effects, or drug release of cements without modifying the crystallization pathway of $CaCO_3$. These $CaCO_3$ cements functionalized with biomolecules exhibit high solubility, fast setting kinetics, and bioactive properties. Besides this, the creation of macropores in $CaCO_3$ ceramics is highly recommended because they enable tissue ingrowth and accelerated osteointegration. Pore size and porosity play important roles in tissue ingrowth, defining the internal surface area available for cell adhesion, spreading and expansion, adsorption of biological metabolites, and bioresorbability at controlled rates that can match that of bone repair.[234] Porous $CaCO_3$ ceramics can be obtained *via* strategic methods, such as the carbonation of $Ca(OH)_2$,[234] introduction of sintering agents at low melting temperature,[226] and sintering under a CO_2 atmosphere.[227] $CaCO_3$ with macropores of over 100 μm can be prepared using NaCl as a pore generator by means of the carbonation of $Ca(OH)_2$/NaCl composite solutions.[234] $CaCO_3$ composite ceramics were fabricated *via* the fast sintering of $CaCO_3$ at 650 °C using the sintering agent phosphate-based glass ($50P_2O_5{\cdot}18CaO{\cdot}12MgO{\cdot}20Na_2O$), which has a low melting temperature.[226] When implanted for *in vivo* study, the increase in bone formation and the associated degradation of the $CaCO_3$ composite ceramics were pronouncedly greater than those of a biphasic CaP ceramic in the early implantation stage for more prolonged implantation times.[226] Highly pure and monodisperse calcite can be assembled without any sintering aid under flowing CO_2 at atmospheric pressure to fabricate porous $CaCO_3$ ceramics with porosities in the range of 10–75%.[227] The obtained $CaCO_3$ ceramics exhibit faster resorption than β-tricalcium phosphate. Furthermore, both resorption and new bone formation are affected by the pore structure. However, such $CaCO_3$ ceramics cannot promote new bone formation during long-term implantation.

The poor compressive strength of $CaCO_3$ cements and ceramics has thus far hindered their utilization. However, in the biosphere, the precipitation of $CaCO_3$ occurs in many living organisms in which $CaCO_3$ acts as a structural support and solid endurable framework. In such organisms, the brittleness of pure $CaCO_3$ is overcome by the integration of organic and inorganic materials. Biogenic $CaCO_3$ has been considered and made into bioactive and biocompatible nacre-, and coral-based bone substitutes or porous ceramics.[235,236] To enhance the compressive strength of $CaCO_3$ cements into the range at which clinical applications (>30 MPa) are feasible and reasonable, ductile polymers have been used to reinforce brittle $CaCO_3$ cements. $CaCO_3$-based organic–inorganic cements exhibit strength and toughness. Myszka *et al.*[231] reinforced brittle $CaCO_3$ cement with a ductile polymeric 2-hydroxyethylmethacrylate. The compressive strength of $CaCO_3$-based cements was observed to increase to 33 MPa upon the addition of 50 wt% of 2-hydroxyethylmethacrylate to a simulated body fluid solution after two weeks of hardening.

4.1.2 $CaCO_3$-based hydrogels.

$CaCO_3$ NPs can be co-functionalized with biomolecules *via* physical or chemical crosslinking, or physical–chemical double crosslinking based on hydrogen bonding, ionic bonding, and van der Waals' forces to form $CaCO_3$-based nanostructured hydrogels.[48] Extracellular Ca plays an important role in bone metabolism. Enrichment of hydrogels with $CaCO_3$ thus improves their suitability as bone regeneration materials. For example, silica/collagen xerogels with added calcite can be used for calcium delivery and can mediate osteoblast proliferation and differentiation.[237]

Several enrichment strategies have been reported in the literature. The first method is the direct formation of $CaCO_3$ during hydrogel formation by delivery of CO_3^{2-} and Ca^{2+}.[238] The second method is alternately soaking hydrogels in solutions of CO_3^{2-} and carbonate Ca^{2+}.[239] Implantation of $CaCO_3$-mineralized agarose hydrogels into cranial defects in rats was found to promote bone regeneration, in which $CaCO_3$ was in the form of a mixture of calcite and vaterite. The third method involves incubation in solutions of Ca^{2+} and CO_3^{2-} ions.[240] The fourth is the diffusion of CO_2 into hydrogels containing Ca^{2+},[241] and double-diffusion systems where Ca^{2+} and CO_3^{2-} ions diffuse into hydrogels from different reservoirs.[242] Gong *et al.*[243] developed injectable fibrin–glue composite hydrogels containing BMP-2 loaded on $CaCO_3$ microspheres. In them, casein and heparin were dissolved in solutions of Ca^{2+} and CO_3^{2-}, respectively. $CaCO_3$ microspheres were co-functionalized with casein and heparin *via* strong affinity and thus showed osteoinductivity and specific binding sites for BMP-2 to achieve dual delivery of growth factors and Ca to promote bone regeneration. These $CaCO_3$-based injectable nanostructured hydrogels can be injected into defects with minimum surgical invasiveness.

A novel strategy to generate $CaCO_3$ formation inside hydrogels has been reported using enzymes such as urease, which catalyzes the conversion of urea and water to form HCO_3^- and NH_4^+. HCO_3^- can undergo deprotonation to form CO_3^{2-}, which then subsequently reacts with Ca^{2+} to form $CaCO_3$. The pH of the environment is raised by the formation of NH_4^+, which promotes the precipitation of $CaCO_3$. Rauner *et al.*[244] incorporated urease in polymer co-networks based on 2-hydroxyethyl acrylate and triethylene glycol dimethacrylate to form $CaCO_3$ crystals within the hydrogel network. The urease-entrapped polymer co-networks were subsequently incubated in an aqueous solution containing urea and $CaCl_2$. This resulted in the deposition of $CaCO_3$ in the form of aragonite and calcite within the hydrogel network. Enzymatic urease-mediated mineralization of gellan gum hydrogels with $CaCO_3$ and Mg-enriched $CaCO_3$ has been reported for bone regeneration,[245] wherein the prepared hydrogels stimulate the adhesion and growth of osteoblast-like cells.

Furthermore, $CaCO_3$ as a crosslinking agent can be used to prepare injectable composite hydrogels. Sodium alginate is a polysaccharide extracted from natural brown algae that readily combines with Ca^{2+} to form Ca^{2+}-crosslinked alginate hydrogels. However, these materials lack injectable properties due to their fast gelation time when the Ca^{2+} source is a $CaCl_2$ solution. The use of a $CaCO_3$ solution, a weak electrolyte, leads to a slower gelation rate due to the slow release of Ca^{2+}. The formation of injectable $CaCO_3$-crosslinked alginate composite hydrogels based on $CaCO_3$ as a Ca^{2+} source has been reported.[48] These $CaCO_3$-crosslinked alginate hydrogels were prepared by blending poloxamers with alginate and crosslinked with $CaCO_3$ *via* chemical and physical double crosslinking. The $CaCO_3$-crosslinked alginate hydrogels exhibit both higher mechanical strength and injectable properties compared with those of Ca^{2+}–alginate hydrogels. However, their shear performance needs to be improved for clinical use of the *in situ* hydrogels, especially in the use for knee joints.

4.1.3 $CaCO_3$-based scaffolds. In bone tissue engineering, a critical challenge is to develop an ideal 3D porous scaffold, which can be acellular or cells/drugs-loaded, acting as a temporary matrix for bone ingrowth and regeneration. Currently, the used scaffolds can be roughly divided into three types, including bioactive ceramics, degradable polymers, and composites. However, bioactive ceramics are rarely used alone as scaffold materials due to their brittleness and difficulty for processing.[246] Moreover, synthetic polymers such as poly(lactic acid), poly(glycolic acid), and their copolymers have drawbacks such as poor bioactivity and low ability to interact with cells.[247] Modification of scaffolds with $CaCO_3$ to form organic–inorganic composite scaffolds can lead to cell adhesion on the surface, which is particularly used for bone tissue regeneration. Composite scaffolds can be prepared *via* co-electrospinning, which combines the use of natural or synthetic polymers or their blends with inorganic $CaCO_3$ NPs.[248]

Natural coralline porous $CaCO_3$ scaffolds have been used for bone substitution since 1970.[249] Coral-derived scaffolds composed of aragonite have been reported to perform better than CaP materials when implanted *in vivo*[250] and enhance osteoblast growth and osteogenic differentiation *in vitro*.[251] $CaCO_3$ can be entrapped on fibrous scaffolds by *in situ* synthesis *via* the mixing of Ca^{2+} and CO_3^{2-} ions, providing a calcium source for bone repair.[252] From this material, a porous structure can be obtained by mineral dissolution and can also be coated with functional molecules such as antibacterial and anti-inflammatory drugs or functional enzymes.

A scaffold based on electrospun polymeric polycaprolactone (PCL) fibers entrapping porous $CaCO_3$ (vaterite) (PCL/$CaCO_3$) has been designed for tissue regeneration with drug delivery and release functionalities.[253] Due to the affinity of tannic acid (TA, $C_{76}H_{52}O_{46}$) for Ca^{2+}, it can be loaded on PCL/$CaCO_3$ scaffolds to improve their antioxidant properties. The *in vivo* recrystallization of vaterite to calcite induces the release of TA. PCL/$CaCO_3$ scaffolds with capabilities of carrying biologically-active molecules and release functionalities are promising candidates for implants in bone and tissue regeneration. The $CaCO_3$ mineralized scaffolds can alter their surface hydrophobicity, enhancing cell adhesion on the surface. For example, piezoelectric poly(3-hydroxybutyrate) (PHB) and poly(3-hydroxybutyrate-*co*-3-hydroxyvalerate) (PHBV) fibrous scaffolds have been assembled *via* electrospinning and mineralized with $CaCO_3$ in vaterite and calcite phases *in situ* using US.[45] The $CaCO_3$-mineralized PHB and PHBV scaffolds converted their surfaces from hydrophobic (for nonmineralized) to hydrophilic (for $CaCO_3$-mineralized), thus enhancing osteoblast cell adhesion and proliferation, and facilitating apatite formation and osteoblast cell growth.

The scaffolds that are used to entrap $CaCO_3$ are generally limited to polymer matrices obtained *via* electrospinning. However, recently, rapid prototyping processes have been used to create polymer/$CaCO_3$ scaffolds with hierarchically porous structures. For example, Woldetsadik *et al.*[254] prepared hierarchically porous $CaCO_3$ scaffolds *via* a template-free, scalable supercritical CO_2 process The supercritical-CO_2 based process introduces nanoscale features to the hierarchically porous $CaCO_3$ scaffolds. These hierarchically porous $CaCO_3$ scaffolds exhibit a well-defined interconnected pore structure, as well as mechanical properties (*e.g.*, hardness and Young's modulus) that are comparable to those of natural bone.

4.2 Hemostatic agents

Bleeding occurs in many clinical conditions, such as skin damage, perforation, and irregular bleeding.[255] Hemostatic materials thus face the challenging requirements of rapid hemostasis, biosafety, and adaptability to different bleeding sites. In traditional Chinese medicine, powdered cuttlebone, a hemostatic material that mainly consists of $CaCO_3$, can be orally administered to rapidly stop bleeding.[256,257] It is important to note that only 0.15 mM of $CaCO_3$ can be dissolved in water at room temperature, which is lower than the concentration of Ca^{2+} in human blood (2.15–2.65 mM).[52] $CaCO_3$, in the form of microspheres that exhibit high porosity and strong adsorption capacity, can be employed in irregular-shaped wounds. While the use of $CaCO_3$ microspheres alone does not stop rapid bleeding, $CaCO_3$–CS composites,[256] $CaCO_3$–CS acetate hydrogels,[51] thrombin (Thr)-loaded $CaCO_3$ microspheres,[52] and self-propelled $CaCO_3$-based hemostatic particles[258] have been developed and successfully employed in wound healing. Ca^{2+} ions together with Thr, are involved in the activation of coagulation factor XIII in the coagulation system. Ca^{2+} also stops bleeding by increasing clot rigidity.[259] $CaCO_3$–CS composites have been prepared *via* a freeze-drying process.[256] These composites can accelerate wound healing; healing wounds over 9 days compared to the 12 days taken for pure $CaCO_3$ to achieve the same goal. However, the low water solubility of CS in neutral pH solution limits its further application in clinical wound healing. Recently, a chitosan acetate–$CaCO_3$ hydrogel was developed to be used as a wound dressing, as illustrated in Fig. 16.[51] In the composite hydrogel, the protons (H^+) released from the charged amino groups ($-NH_3^+$) of chitosan acetate chains reacted with $CaCO_3$, producing Ca^{2+} and amino groups ($-NH_2$). $CaCO_3$ reduces the acidity of the chitosan acetate, decreasing the potential for skin irritation. Moreover, upon reacting with $CaCO_3$, the $-NH_3^+$ group of the chitosan acetate is no longer positively charged. As a consequence, Ca^{2+} ions from $CaCO_3$ cross-link with the $-NH_2$ groups of the chitosan acetate to form a strong and stiff

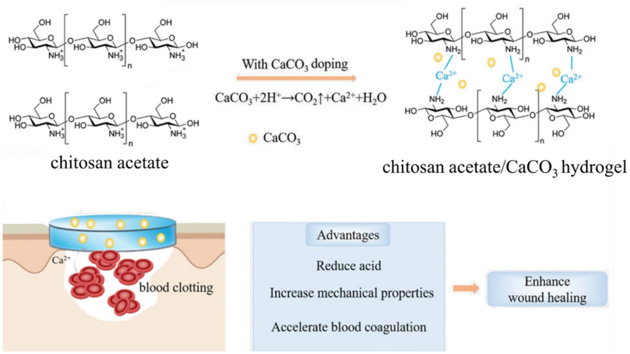

Fig. 16 Schematic illustration of reaction occurring between chitosan acetate and $CaCO_3$. The protons (H^+) from the protonated amino groups of chitosan acetate react with $CaCO_3$ producing Ca^{2+} and CO_2. The Ca^{2+} contribute, together with the $CaCO_3$ particles, to cross-link chitosan chains by coordination bonds involving amino and hydroxy (not shown) groups, increasing the mechanical properties. When the soft hydrogel adhered stably to a wound site, the released Ca^{2+} and remaining $CaCO_3$ accelerated blood coagulation Adapted and reprinted from ref. 51. Copyright (2018), with permission from John Wiley and Sons under the terms of the Creative Commons Attribution Non-Commercial (CC BY-NC 3.0) License.

colloidal hydrogel *via* electrostatic interactions (Fig. 16). In addition, when the hydrogel attaches to a wound site, Ca^{2+} ions participate in hemostasis, accelerating the formation of blood clots by favoring the conversion of prothrombin to Thr, as well as catalyzing many other coagulation-related reactions that promote the blood coagulation process.

Thr-loaded TA–$CaCO_3$ microspheres (Thr@TA–$CaCO_3$) have been prepared, wherein TA acts as a linker that connects the $CaCO_3$ microspheres and Thr,[52] and then when this material is used, Thr directly acts on the last step of the blood coagulation process together with coagulation factors to form insoluble fibrin. In particular, varying the amount of adsorbed Thr allowed control of the hemostatic time and the hemostatic ability of Thr@TA–$CaCO_3$. For example, the Thr@TA–$CaCO_3$ material when used reduced 94.9% of blood loss in an arterial injury in a rabbit.[52]

However, such $CaCO_3$-based hemostatic materials require an external force to prevent blood flow to ultimately reach deep bleeding sites, resulting in coagulation in the superficial layers of the wound only. Attempts have thus been made to develop a mobile $CaCO_3$-based powder hemostat with self-propelling properties so that the prepared material can overcome hemodynamic forces.[255] $CaCO_3$ rapidly produces CO_2 in acidic solutions, forming porous MPs that adsorb protein, thus making it an ideal substance for making self-fueled particles. Thr-loaded $CaCO_3$ particles with self-driving properties have been reported,[258] prepared *via* the mixing of porous $CaCO_3$ MPs with organic tranexamic acid (TXA–NH_3^+) in a 1 : 1 molar ratio and then injected into a buffered saline solution or whole blood. To create propelling particles that clot blood, Thr was adsorbed onto porous $CaCO_3$ MPs. Once the Thr-loaded self-fueled $CaCO_3$ MPs came into contact with blood, large amounts of microbubbles were generated and forced the MPs to move around in the bleeding wound. The Thr-loaded self-fueled $CaCO_3$ MPs were pulled into the bleeding wound, allowing them to reach the deep bleeding site, thus increasing their efficiency. However, the microbubbles released from $CaCO_3$ dissolution are mostly non-direction-selective. Thus, a significant number of MPs moved into the superficial layers of the wound, resulting in a reduction in the efficiency of the $CaCO_3$-based hemostat. Additionally, acid–base reactions consumed the $CaCO_3$ vector. A possible solution to this issue is to improve the movement of $CaCO_3$-based hemostatic MPs so that they can be driven in a desired direction. Biphasic Janus self-propelled hemostatic particles (MSS@$CaCO_3$) were prepared *via* the uniaxial growth of flower-like $CaCO_3$ crystals on microporous starch (MSS) that was modified to be negatively charged (Fig. 17).[255] The as-synthesized hemostatic Janus particles were then loaded with Thr (MSS@$CaCO_3$T) and powered by the internal component $CaCO_3$, in collaboration with protonated TXA (Fig. 17A–C). The prepared Janus MSS@$CaCO_3$T self-propelled itself against flowing blood *via* a bubble detachment mechanism (Fig. 17D). $CaCO_3$ loading on such unilateral Janus MSS@$CaCO_3$T particles resulted in the preparation of a motorized hemostat with self-propelling properties that were shown

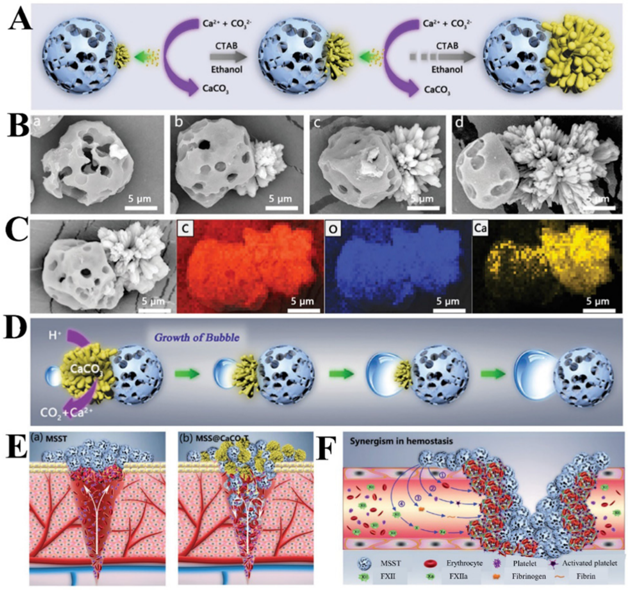

Fig. 17 Schematic diagram showing synthetic procedure for preparing Janus MSS@$CaCO_3$T particles for the control of perforating and irregular hemorrhages. (A) Illustration of the growth of flower-like $CaCO_3$ crystals on negative-potential-charged microporous starch (MSS) during the synthesis of the Janus MSS@$CaCO_3$ particles. (B) SEM images of MSS@$CaCO_3$ Janus particles with different ratios of [MSS]/[$CaCO_3$]: (a) 1 : 0.1, (b) 1 : 0.5, (c) 1 : 1, and (d) 1 : 2. (C) EDS mapping of the C, O, and Ca elements of the MSS@$CaCO_3$ Janus particles with an aspect ratio of 1 : 1. (D) Illustration of bubble growth over a Janus particle during its self-propelling motion. (E) Illustration of the proposed hemostatic process of (a) MSST and (b) Janus MSS@$CaCO_3$T in hemorrhage models. (F) Illustration of the proposed blood coagulation mechanism. Reprinted from ref. 255. Copyright (2020), with permission from John Wiley and Sons under the terms of the Creative Commons Attribution Non-Commercial (CC BY-NC 3.0) License.

to be able to reach deep bleeding sites (Fig. 17E and F) of the liver and femoral artery hemorrhage models, wherein the hemorrhages were rapidly controlled in ≈50 s and ≈3 min, respectively.

4.3 pH-Sensitive $CaCO_3$ NPs as bioimaging contrast agents

US is one of the most powerful non-invasive, diagnostic imaging tools that is currently available. Tumor and normal body tissues have similar ultrasonic properties, thus making it difficult to distinguish between them.[260] To this aim, $CaCO_3$ has been used to construct enhanced contrast agents to improve the resolution of ultrasound imaging. The developed $CaCO_3$-based enhanced contrast agents for US imaging have been shown to exhibit strong echogenic signals at the site of tumor tissue and excellent echo persistence.[222] The prepared pH-sensitive $CaCO_3$ NPs are stable at neutral pH and decompose to generate hyperechogenic CO_2 bubbles under acidic conditions. The $CaCO_3$ NPs can be activated under stereotypical tumoral acidic conditions.[261] In addition, by combining $CaCO_3$ NPs with paramagnetic ions such as Gd^{3+}, pH-responsive $CaCO_3$-based composites can be used for MR/US dual-modal imaging.

4.3.1 US Imaging. $CaCO_3$ NPs circulate stably in the bloodstream and can effectively accumulate in tumor tissues *via* enhanced permeation and retention effects. Thus, gas-generating $CaCO_3$ NPs may overcome the limitations of currently used gas-filled microbubbles such as perfluorocarbons.[56] The pH-sensitive $CaCO_3$ NPs continuously generate CO_2 nanobubbles that coalesce into microbubbles, allowing for the persistent strong echogenic US imaging.[222] For instance, a $CaCO_3$-based US imaging agent ($CaCO_3$AlgNC) that is stable in serum-containing media was prepared by encapsulating $CaCO_3$ NPs in a flexible and biocompatible alginate-loaded pluronic-based nanocarrier (AlgNC).[262] Upon injection, $CaCO_3$AlgNC shows CO_2 generation that increases with time and US contrast enhancement at the tumor site within 1 h, in comparison to no change in US contrast observed in the liver, followed by its fast clearance from the body within 24 h.[53] In another case, Lee *et al.*[54] encapsulated $CaCO_3$ in poly(D,L-lactide-coglycolide) NPs using a water-in-oil-in-water double emulsion method and created pH-sensitive CO_2-generating $CaCO_3$/polymer NPs. The $CaCO_3$/polymer NPs were found to release CO_2 bubbles under acidic conditions and enhance ultrasound imaging signals.

4.3.2 Multimodal imaging. For accurate diagnosis to be achievable from images, $CaCO_3$-based multimodal imaging agents have been developed. A pH-sensitive US and MR dual-modal imaging agent ($NaGdF_4$@$CaCO_3$–PEG) was developed to simultaneously improve tissue discrimination ability and provide real-time images by depositing a $CaCO_3$ shell on the surface of a $NaGdF_4$ NP core *via* a microemulsion method.[263] In the acidic tumor microenvironment (TME), the $CaCO_3$ shell gradually dissolves and the $NaGdF_4$ releases, contributing to the interaction between $NaGdF_4$ and the external aqueous environment to enhance water proton relaxation. The $NaGdF_4$@$CaCO_3$–PEG NPs display strong elastic echo and enhancement of the MRI signal by triggering the previously silenced $NaGdF_4$ release with CO_2 bubbles generated *via* the dissolution of $CaCO_3$ in the acidic TME. Thus, $NaGdF_4$@$CaCO_3$–PEG exhibits strong dual-modal MR/US imaging abilities in the acidic TME.

4.4 Drug and gene nanocarriers for therapy

Inorganic NPs, such as SiO_2, CaP, tricalcium phosphate, hydroxyapatite, and layered double hydroxides are promising drug and gene nanocarriers that exhibit high drug and gene loading.[272] However, the poor biodegradability of these inorganic NPs and the lack of a controllable pH-responsive mechanism often hinder their clinical application.[267] Organic NPs, such as dendrimers, liposomes, micelles, and polymer NPs, display excellent pH sensitivity, yet their use under physiological conditions is limited because of their organic composition. These limitations are not applicable to $CaCO_3$ NPs due to their nontoxicity, biocompatibility, biodegradability, and acid sensitivity, as well as their finely controlled synthesis and ease of functionalization, thus meaning that they can be used for pH-responsive drug/gene/protein delivery (Fig. 18).[95,273] The structure of the $CaCO_3$ NPs is well maintained in normal tissues, while drug release can be triggered in the acidic environments of tumor tissues (pH 6.5–6.8) and endosomes/lysosomes (pH 4.5–6.5) (Fig. 18A and B).[273] The positively-charged Ca^{2+} that are exposed on the surface of the $CaCO_3$ NPs have a high affinity toward negatively-charged groups, thus making it possible to functionalize them with targeting agents to advance precision-targeted therapy and controlled drug release (Fig. 18C).[274] Thus, the pH-sensitive properties of $CaCO_3$ NPs provide a new possibility for targeting and controlling the release of drugs and genes in the human body (Table 3).

4.4.1 Drug delivery

(1) Porous $CaCO_3$ nanocarriers. Porous $CaCO_3$ nanocarriers exhibit a high specific surface area and high drug loading capacity, which make them suitable for use in drug delivery. Zhang *et al.*[275] studied the biocompatibility of porous $CaCO_3$ toward HeLa cells, with the results implying that porous $CaCO_3$ shows good biocompatibility. For maximizing therapeutic activity by increasing the concentration of $CaCO_3$, the effect of high dosages of reactive oxygen species (ROS) and glutathione (GSH) should be judiciously considered. Haruta *et al.*[276] performed an insulin-loading study, which took advantage of the non-toxicity and biocompatibility of porous $CaCO_3$. In this context, animal and clinical studies have shown that the nasal delivery of insulin loaded with porous $CaCO_3$ can act quickly to control blood sugar levels, especially in diabetics, but longer-term toxicity tests are needed to ensure safety in humans. Ibuprofen, nifedipine, losartan potassium, metronidazole benzoate, and other poorly water-soluble drugs have been effectively loaded onto porous $CaCO_3$ *via* solvent evaporation, with the loading capacity equivalent to the pore capacity of the carrier and no drug loss experienced during the process.[277]

(2) Hybrid $CaCO_3$/active molecular single crystals. $CaCO_3$ single crystals are an ideal nanoplatform to construct smart

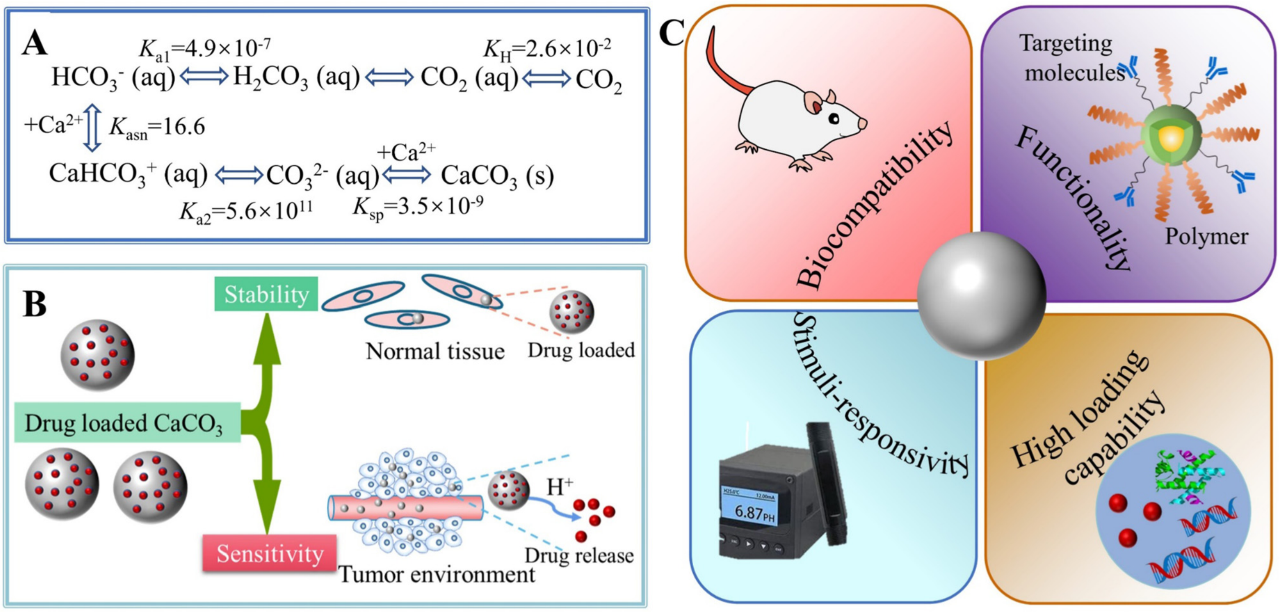

Fig. 18 Schematic diagram showing $CaCO_3$-based drug and gene nanocarriers. (A) The pH-dependent solubility of $CaCO_3$: equilibrium relationship between CO_2 and $CaCO_3$. Data were taken from ref. 264. (K_{sp}, the solubility product; K_{asn}, the association constant of calcium and bicarbonate; K_a, the equilibrium constant of carbonate and bicarbonate). (B) Drug-loaded $CaCO_3$ NPs: slow dissolution at normal physiological pH (7.4) and faster dissolution and release of drugs at acidic pH (<6.5) in the tumor environment. (C) Function and characteristics of $CaCO_3$ NPs for their use as a nanocarrier.

vehicles for drug-targeted delivery due to their capability to adsorb and entrap drugs. The pH-sensitive solubility of $CaCO_3$ can be exploited to release entrapped molecules only when the dissolution of the crystals occurs to achieve zero leakage of drugs at physiological pH. In pioneering research, complete structural and biological characterization of doxorubicin (DOX)/$CaCO_3$ single crystals has led to the following points being highlighted: (i) calcite can load DOX molecules efficiently; (ii) DOX molecules are entrapped along specific crystallographic directions of calcite; (iii) the release of DOX molecules is pH-responsive and occurs preferentially close to the surface of cancer cells; and (iv) the released drug molecules are uptaken by the cancer cells, which leads to their death.[278] Hybrid calcite single crystals can also be used as micro-carriers for the controlled local release of retinoic acid, which is entrapped within single crystal lattice of calcite. The release of retinoic acid occurred only in the proximity of stem cells, upon dissolution of the hybrid calcite crystals that were dispersed in a fibrin scaffold. The environment provided by this composite scaffold enabled differentiation towards neuronal cells that form a 3D neuronal network.[279]

(3) Organic–inorganic hybrid nanocarriers. The functionalization of $CaCO_3$-based nanocarriers by polyelectrolytes to form organic–inorganic hybrid nanocarriers *via* a layer-by-layer assembly method not only leads to the formation of a material with increased drug loading capacity and controlled drug release properties, but improved thermodynamic stability and tumor targeting capability.[280] In a research, $CaCO_3$ and lentinan have been employed in a biomineralization inspired process to produce $CaCO_3$–lentinan composites with a hierarchical composite pore structure *via* the hierarchical assembly of NPs.[281] The hierarchical $CaCO_3$–lentinan composites were observed to obviously reduce the release rate and prolong the release time of the anticancer drug DOX. Reduced graphene oxide–tetraethylenepentamine (rGO–TEPA) sheet matrices have been mineralized with $CaCO_3$ to produce a $CaCO_3$/rGO–TEPA drug carrier with a hollow structure and rough surface. $CaCO_3$/rGO–TEPA exhibited a DOX loading efficiency of 94.7% and release efficiencies at pH 7.4 and 5.0 of 13.8% and 91.7%, respectively.[266] Mesoporous PAA/$CaCO_3$ NPs have also been synthesized that exhibit a high drug loading capacity for DOX, achieved due to the electrostatic interactions between the negatively-charged carboxyl groups ($-COO^-$) of PAA and positively-charged DOX NPs.[282]

$CaCO_3$-based nanocarriers can be functionalized with targeting agents, such as peptides, antibodies, polymers, and aptamers, to achieve targeted delivery and controlled drug release simultaneously. Surface modification of the NPs with PEG leads to their higher stability in the bloodstream as well as preventing them from being captured by macrophages, and/or adjustment of their active targeting capability so that these carriers can accumulate at a specific site.[283] For example, mesoporous $CaCO_3$ NPs were functionalized *via* a layer-by-layer assembly technique using SA and CS as alternating assembly materials and FA as a target molecule and then surface modified with PEG before being loaded with DOX.[273] Due to the acid-mediated targeting of cells by mesoporous $CaCO_3$ NPs, DOX-loaded FA-targeted polyelectrolyte hybrid mesoporous $CaCO_3$ NPs exhibited significant cell-inhibitory effects. Analogously, porous $CaCO_3$ NPs of 250 nm in size acted as a carrier to encapsulate and deliver the photosensitizer Hypocrellin B in the body for photo-dynamic therapy.[267]

In addition, anticancer drugs can be encapsulated *via in situ* $CaCO_3$ mineralization, preventing a loss of drugs during circulation and the need for post treatment. DOX@$CaCO_3$–hesperidin nanospheres were prepared using hesperidin as a crystallization pathway modifier at room temperature.[284] The crystallization of $CaCO_3$ was initiated by the gradual diffusion of CO_2 and NH_3 into a mixed solution of $CaCl_2$, hesperidin, and DOX. DOX@$CaCO_3$–hesperidin nanospheres, with a narrow size range of ~200 nm, showed a drug loading efficiency of 83%, a drug loading content of 14 wt%, and pH-responsive drug release performance. A small number of cells were killed at pH = 7.4 (cell viability = 99 ± 9%), indicating very little DOX release. However, when the pH value was decreased to pH = 5.0, the cell viability dropped to 38%.

(4) $CaCO_3$-Based synergistic therapy nanoplatform. Construction of a multifunctional stimuli-responsive $CaCO_3$-based nanoplatform enabling improved intratumoral penetration of therapeutics and reversal of multiple-drug resistance is an important goal in achieving effective cancer treatment. For example, a nanocomposite consisting of $CaCO_3$-modified magnetic polydopamine (PDA) NPs loaded with indocyanine green (ICG), namely Fe_3O_4@PDA@$CaCO_3$/ICG (FPCI) NPs, were developed to integrate the photothermal capability of PDA with the photodynamic capability of ICG.[50] In particular, $CaCO_3$ not only entraps ICG in the form of a stable aggregate to evade blood clearance, but also facilitates the controlled release of ICG in response to the acidic TME *via* a self-decomposition process. The release of ICG was subsequently activated through the acidolysis of $CaCO_3$ in the presence of protons (H^+). Therefore, the acidic TME serves as a key to switch on the dissolution of the $CaCO_3$ layer and release the entrapped ICG. Subsequently, the PDA nanoshell and released ICG function as NIR light-energy photoabsorbers for achieving photothermal therapy, while ICG also serves as a photosensitizer for inducing PDT.

A $CaCO_3$-based multifunctional nanoplatform can be used to realize synergistic therapies (Table 3). A multifunctional therapeutic agent makes it possible to achieve a combination of PTT, PDT, Ca^{2+} interference, and chemodynamic therapy. To this aim, a nanoscale covalent organic framework (NCOF)-based nanoagent, $CaCO_3$@COF–BODIPY-2I@GAG, was embedded with $CaCO_3$ NPs and surface modified with a photosensitizer (PS) (BODIPY-2I) and a glycosaminoglycan (GAG) targeting agent for CD44 receptors on digestive tract tumor cells (Fig. 19A). Under light irradiation, the surface covalently attached BODIPY-2I generates $^1O_2$, while the NCOF matrix-protected $CaCO_3$ NPs are safely delivered into tumor cells *via* endocytosis without any premature leakage. Moreover, the pH-sensitive $CaCO_3$ NPs dissolve in the endo/lysosomes (pH = 5.0) and release Ca^{2+} (Fig. 19A–C). The $CaCO_3$@COF–BODIPY-2I@GAG coated with GAG, a specific targeting agent

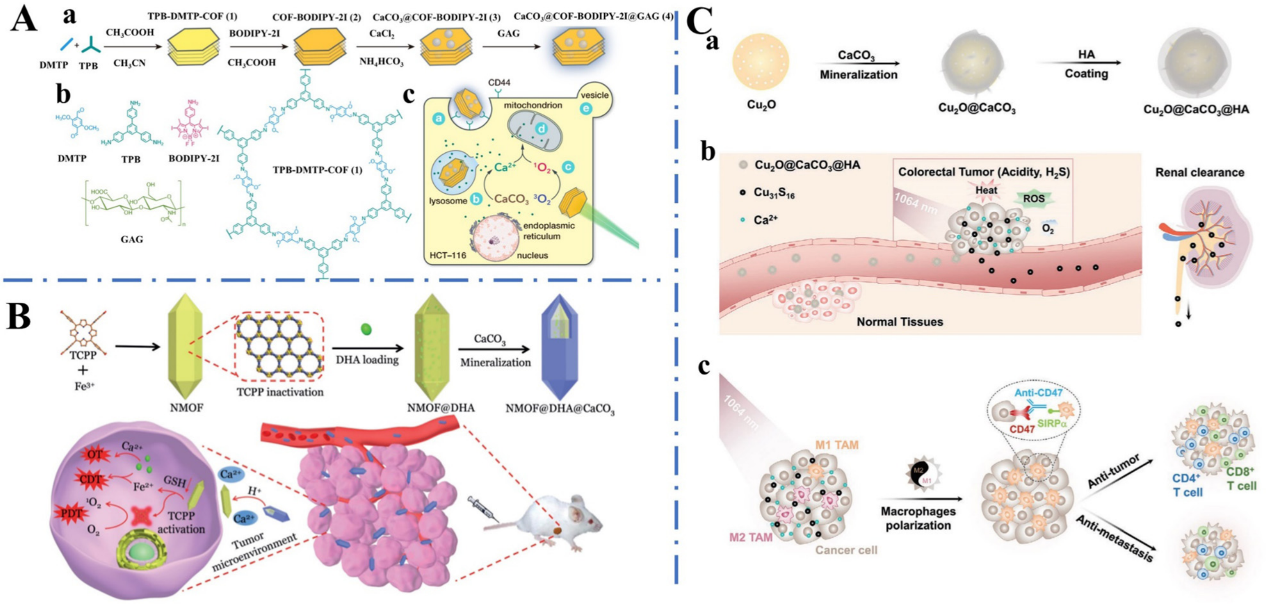

Fig. 19 Schematic diagram of a $CaCO_3$-based multifunctional nanoplatform. (A) A glycosylated covalent organic framework equipped with BODIPY and $CaCO_3$ for synergistic tumor therapy. (a) Synthetic procedure of $CaCO_3$@COF–BODIPY-2I@GAG. (b) Molecular structure of DMTP, TPB, BODIPY-2I, GAG, and TPB–DMTP–COF. (c) Synergistic intracellular Ca^{2+} overload and PDT. Reprinted from ref. 269. Copyright (2020), with permission from John Wiley and Sons under the terms of the Creative Commons Attribution Non-Commercial (CC BY-NC 3.0) License. (B) Preparation of the nanoplatforms and the programmed drug release for cancer therapy. Reproduced from ref. 268. Copyright (2019), with permission from John Wiley and Sons under the terms of the Creative Commons Attribution Non-Commercial (CC BY-NC 3.0) License. (C) A colorectal tumor microenvironment-activated bio-decomposable and metabolizable Cu_2O@$CaCO_3$ nanocomposite for synergistic oncotherapy a) Synthetic route of Cu_2O@$CaCO_3$@HA. (b) The tumor microenvironment-triggered bio-decomposition, anti-tumor responses, and renal clearance of Cu_2O@$CaCO_3$@HA. (c) The antitumor immune responses activated by the tumor microenvironment in combination with CD47 blockade. Reprinted from ref. 270. Copyright (2020), with permission from John Wiley and Sons under the terms of the Creative Commons Attribution Non-Commercial (CC BY-NC 3.0) License.

for CD44 receptors on digestive tract tumor cells, significantly promoted the uptake in HCT-116 cells. The $CaCO_3$@COF–BODIPY-2I@GAG therapeutic agent thus displays significantly enhanced antitumor efficiency *via* synergistic PDT and $^1O_2$-triggered Ca^{2+} overload both *in vitro* and *in vivo*.

Triple synergistic therapy in the form of chemodynamic, oncosis, and PDT, can be achieved using $CaCO_3$ mineralized nanoplatforms. A NMOF@DHA@$CaCO_3$ nanoplatform was constructed from a Fe-TCPP [(4,4,4,4-(porphine-5,10,15,20-tetrayl) tetrakis (benzoic acid)] NMOF (nanoscale MOF) coated with a $CaCO_3$ mineralized layer (Fig. 19B).[268] Dihydroartemisinin (DHA) was encapsulated within the pores of the NMOF coated with the $CaCO_3$ mineralized layer, preventing leakage during its transport in the bloodstream. When the nanoplatform reaches tumor sites, the outer $CaCO_3$ layer dissolved in the weakly acidic TME to generate NMOF@DHA and Ca^{2+}. Then NMOF@DHA enters cancer cells and the Fe^{3+} of NMOF is reduced to Fe^{2+} due to the high concentration of intracellular glutathione (GSH), resulting in structural collapse of the NMOF structure. With this structural collapse, the release of DHA and the activation of TCPP contributed to the synergistic treatment *via* Fe^{2+}–DHA-mediated chemodynamic, Ca^{2+}–DHA-mediated oncosis, and TCPP-mediated PDT. This triple synergistic therapeutic action allows the highest cancer therapeutic efficiency to be achieved by the system, promoting the complete ablation of the tumor. Cu_2O can be used as a precursor for preparing $Cu_{2-x}S$ therapeutic agents to perform promising H_2S-activated PTT/PDT. Classic research evidence has demonstrated that the upregulation of the cystathionine-β-synthase enzyme increases the production of endogenous H_2S in the acidic microenvironment of colorectal tumors. In this pursuit, acidic dissolvable $CaCO_3$ was selected as a protective shell to prevent Cu_2O from reacting with sulfide to produce active $Cu_{2-x}S$ before reaching the colorectal cancer sites. A core–shell Cu_2O@$CaCO_3$ nanocomposite was first prepared (Fig. 19C-a),[270] before functionalizing it with HA (Cu_2O@$CaCO_3$@HA) to endow the Cu_2O@$CaCO_3$ nanocomposite with desirable targeting ability and biocompatibility. Once the Cu_2O@$CaCO_3$@HA reaches colorectal cancer sites, the $CaCO_3$ mineralized layer dissolves and releases Ca^{2+}, resulting in intracellular Ca^{2+} overload, thus resulting in Ca^{2+} interference therapy (Fig. 19C–b). Subsequently, the nanocomposite decomposes into $Cu_{31}S_{16}$ NPs when the exposed Cu_2O comes into contact with H_2S, exhibiting prominent photothermal performance, photocatalytic properties, and Fenton-like activity toward PTT/PDT/chemodynamic therapy. The hyperthermia and oxidative stress generated from the Cu_2O@$CaCO_3$ nanocomposite can efficiently reprogram macrophages from the M2 phenotype to the M1 phenotype and initiate a vaccine-like immune effect after primary tumor removal (Fig. 19C–c), further inducing an immune-favorable TME and intense immune responses toward anti-CD47 antibodies to simultaneously inhibit colorectal cancer distant metastasis and recurrence *via* immunotherapy.

4.4.2 Gene delivery. Gene nanocarriers based on biomineralized $CaCO_3$ have received increasing attention because their degradation facilitates transfection and clearance from the body to minimize toxicity.[271] The technique of the co-precipitation of Ca^{2+} with DNA in the presence of inorganic anions such as CO_3^{2-} present in the body is an attractive option because of its good biocompatibility and biodegradability. $CaCO_3$/CaP/DNA NPs have been fabricated *via* the co-precipitation of Ca^{2+} with DNA in the presence of CO_3^{2-} and PO_4^{3-} simultaneously.[285] The co-existence of CO_3^{2-} and PO_4^{3-} efficiently slows crystallization, and the size of the $CaCO_3$/CaP/DNA NPs prepared can be well controlled to <200 nm in aqueous media, with a DNA encapsulation efficiency of around 90%. Due to their enhanced cellular uptake and nuclear localization, the gene delivery efficiency of the $CaCO_3$/CaP/DNA NPs can be significantly enhanced. To this aim, to improve colloidal stability, gene loading capacity, and cellular uptake efficacy, Wu *et al.*[286] developed lipid-coated $CaCO_3$/CaP hybrid NPs for the delivery of dsDNA/siRNA. The lipid-coated $CaCO_3$/CaP NPs release the loaded dsDNA/siRNA mainly under mildly acidic conditions (pH 6.0–5.5), which enables fast siRNA release during endocytosis as well as fast mRNA downregulation. Ternary NPs protamine sulfate–$CaCO_3$–plasmid DNA NPs have been prepared by adding protamine sulfate during the co-precipitation of $CaCO_3$ and DNA.[287] The overgrowth and aggregation of the $CaCO_3$-based NPs are inhibited by the stabilizing properties of protamine sulfate. The gene delivery efficiency of the protamine sulfate–$CaCO_3$–plasmid DNA NPs was found to be better than those of Lipofectamine 2000–DNA complexes.

More interestingly, mild photothermal heating (~43 °C) increased the permeability of the cell membrane, thereby enhancing cellar uptake and gene transfection efficiency. Thus, the intergration of mild photothermal heating and biomineralized $CaCO_3$-based gene carrier enhanced gene therapy could lead to improved therapeutic effects without causing inflammation in the body. The assembled structures of polysaccharides are supposed to induce the crystal nucleation and growth of $CaCO_3$ *via* electrostatic interactions or hydrogen bonds. One-dimensional (1D) Alg–$CaCO_3$ NPs were produced by assembling micelles of polysaccharide SA as a template for their mineralization (Fig. 20).[271] Then, a PDA coating was applied to conjugate the cationic polymer PGED (ethylenediamine functionalized poly(glycidyl methacrylate)) to the surface of the 1D Alg–$CaCO_3$ NPs *via* a Schiff base/Michael addition reaction to endow the NPs with mild hyperthermia and p53 gene delivery functions. Under NIR-light irradiation, mild hyperthermia was triggered to enhance cellular uptake of the NPs. The pH-responsive degradation of the Alg–$CaCO_3$–PDA–PGED gene carrier further promoted gene release, thereby enhancing gene transfection efficiency. Meanwhile, tumor cell apoptosis was induced effectively without causing any pro-inflammatory responses in the body. In addition, taking advantage of the photothermal effect of PDA and the generation of CO_2 bubbles from $CaCO_3$ dissolution in the acidic TME, dual-modal US imaging and photoacoustic imaging (PAI) was realized to monitor and guide the therapy. The $CaCO_3$-based multifunctional platform thus represents a desirable system for the construction of photothermal gene carriers for enhanced therapeutic effects in an inflammation-free manner.

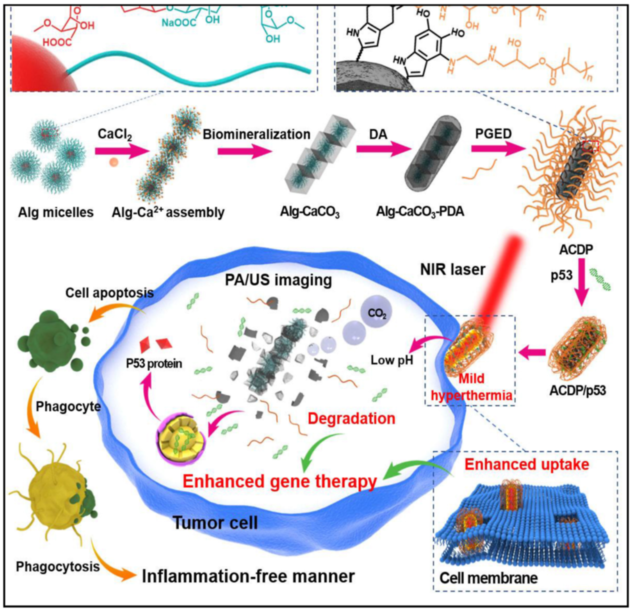

Fig. 20 Schematic diagram of the preparation of an Alg–$CaCO_3$–PDA–PGED gene carrier and its application in mild hyperthermia-enhanced gene therapy. Alg: alginate; PDA: polydopamine; PGED: ethylenediamine functionalized poly (glycidyl methacrylate). Reprinted from ref. 271. Copyright (2021), with permission from Elsevier.

$CaCO_3$-based nanocarriers can be further designed for efficient co-delivery of gene and drugs. Alg-modified $CaCO_3$ NPs have been used for the co-delivery of a therapeutic gene (p53 plasmid) and DOX. The Alg/$CaCO_3$/DNA/DOX NPs exhibited a high cell inhibition rate of around 80%, indicating that the Alg/$CaCO_3$/DNA/DOX NPs effectively mediated gene transfection and delivered the drug to the cells. To further impart active targeting properties to $CaCO_3$-based delivery systems, Liang *et al.*[288] introduced a biotin moiety to a $CaCO_3$-based nanocarrier and prepared heparin–biotin/heparin/$CaCO_3$/CaP hybrid NPs *via* co-precipitation. p53 and DOX were co-loaded simultaneously on the hybrid NPs during their co-precipitation. Due to the presence of the $CaCO_3$/CaP inorganic component and biotin moiety in the polymer chain, the heparin–biotin/heparin/$CaCO_3$/CaP/DNA/DOX NPs exhibited both pH sensitivity and tumor-targeting properties, respectively.

4.4.3 Bioactive substance carrier. Despite their excellent therapeutic effect, target specificity, and biosafety, bioactive substances have limitations when used in clinical applications because they are degraded by proteolytic enzymes, making it difficult for them to permeate target cells. The encapsulation of bioactive substances into $CaCO_3$ NPs thus not only protects the bioactive substances from harsh environments but also ensures their efficient delivery. The $CaCO_3$-based nanocarrier can also be further functionalized with ligands for targeted delivery. When doping polyanionic heparin into $CaCO_3$ microparticles is performed to endow the $CaCO_3$ with a negative charge, this increases the interaction between $CaCO_3$ and cationic lysozyme. Moreover, the activity of the encapsulated lysozyme is almost completely retained.[289] Cancer recurrence after surgical resection remains a significant cause of treatment failure. $CaCO_3$ NPs can therefore be incorporated into fibrin gel to serve as a release reservoir for immunomodulatory therapeutics and a proton scavenger to modulate the acidity of the TME. An immunotherapeutic fibrin gel (aCD47@$CaCO_3$@fibrin) can be formed *in situ* by quickly spraying and mixing of a fibrinogen solution containing anti-CD47 antibody-loaded $CaCO_3$ NPs (aCD47@$CaCO_3$) and Thr solution within the tumor resection cavity after surgery.[290] $CaCO_3$ NPs embedded in the gel matrix gradually dissolve and release the encapsulated anti-CD47 antibodies in the acidic TME. Furthermore, the anti-CD47 antibodies locally released from $CaCO_3$ NPs block CD47 and SIRPα interactions and boost antitumour T cell responses in cancer cells, thus removing cancer cell by macrophages. To effectively enhance antitumor immune responses, pH-sensitive $CaCO_3$ NPs and a reactive oxygen species (ROS)-responsive hydrogel have been used for the codelivery of anti-PD1 antibodies and Zebularine.[291] The Zebularine-anti-PD1-gel enabled controlled release of payloads by responding to the acidic pH and ROS conditions associated with the TME.

$CaCO_3$ MPs are intrinsically hydrophilic with a net neutral charge, meaning that they can enhance ovalbumin–$CaCO_3$ nanocomposite (OVA@$CaCO_3$) translocation across a mucus barrier. Furthermore, they can be surface modified *via* simple adsorption with ligands that specifically target receptors on antigen-presenting cells for targeted vaccine delivery.[292] Peptide nanofiber–$CaCO_3$ composite MPs have been synthesized *via* a precipitation reaction between $CaCl_2$ and Na_2CO_3 and the growing $CaCO_3$ cores captured antigenic peptide OVA nanofibers within them.[292] The peptide nanofiber–$CaCO_3$ composite MPs can be used as self-adjuvant oral vaccine delivery vehicles. They were found to efficiently penetrate the mucus barrier and localize to immune inductive sites where they elicited the production of the protective IgA isotype. Encapsulation of the nanofibers into $CaCO_3$ microparticles not only protected the nanofibers from the harsh gastric environment but also ensured efficient delivery and antigen dose sparing for oral delivery. Traditional $CaCO_3$ particles with bulk structures remain unsuitable for efficient antigen loading. Hierarchical $CaCO_3$ NPs ($\approx$500 nm) were fabricated using the soft template antigen OVA (Fig. 21A and B). The crystallization of $CaCO_3$ was affected by the presence of the OVA soft template at the start of particle formation, leading to the formation of primary grains ($\approx$30 nm) of vaterite. The vaterite grains were further stacked into hierarchical NPs (Fig. 21C), inside which OVA was embedded NPs (Fig. 21D). The hierarchical OVA@$CaCO_3$ NPs were shown to express high-performance antigen delivery and cross-presentation (Fig. 21E).[40] Taking advantage of the unique physicochemical properties of crystalline vaterite, cluster structure, and its high loading with OVA, the OVA@$CaCO_3$ NPs can efficiently ferry the cargo antigen to dendritic cells and blast lysosomes for antigen escape to the cytoplasm (Fig. 21F). After navigation to acidic lysosomes, the OVA@$CaCO_3$ NPs dissolved, generating drastic CO_2 release that blasts the lysosomal membranes mechanically (Fig. 21G). The CO_2 produced from the

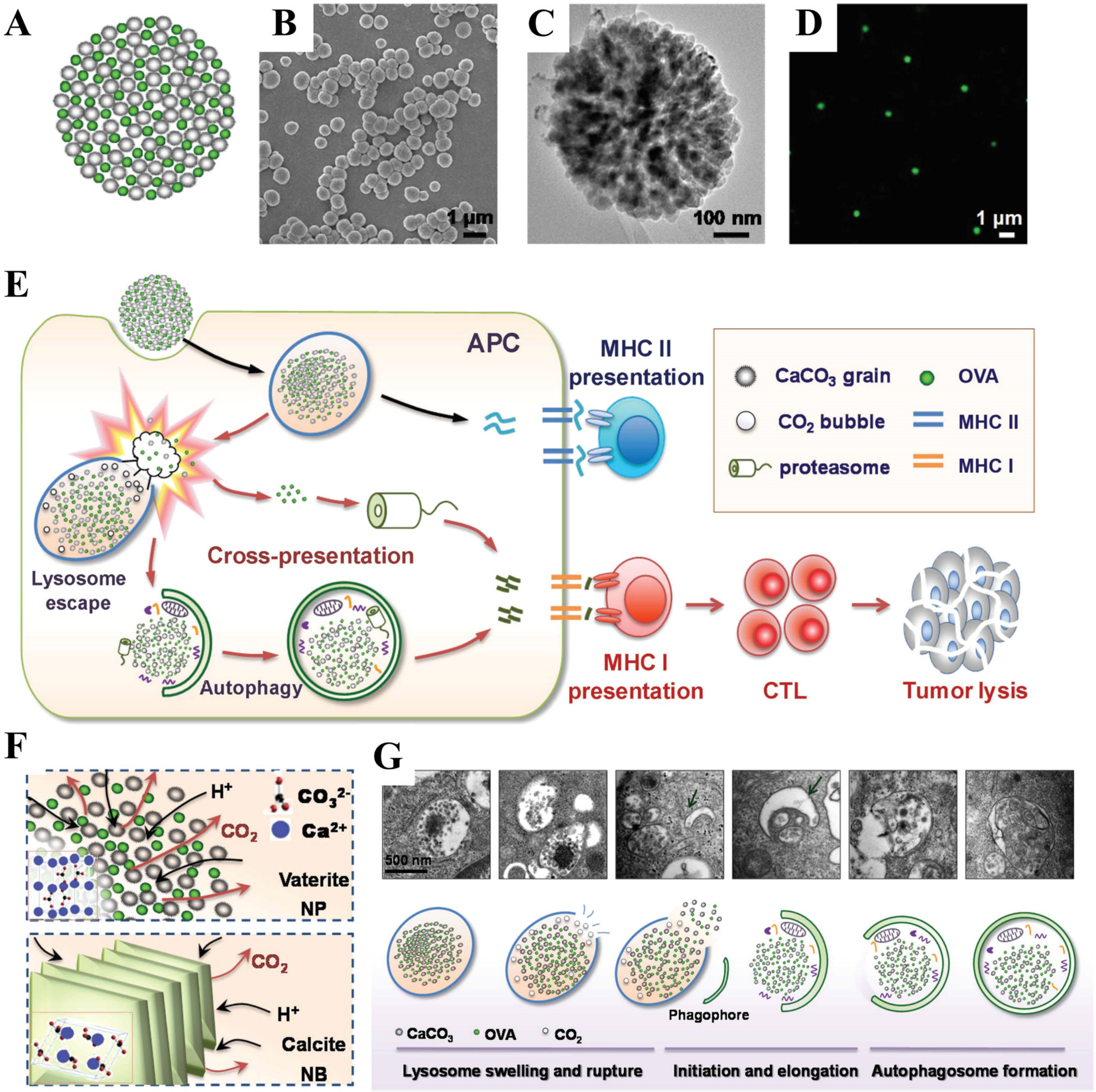

Fig. 21 Schematic diagram illustrating characterization of an ovalbumin@$CaCO_3$ nanoparticles (OVA@$CaCO_3$ NP) and its application in potential antigen cross-presentation. (A) Schematic illustration, (B) SEM image, and (C) TEM image showing the hierarchical structure of an OVA@$CaCO_3$ NP; (D) CLSM image demonstrating the successful doping of OVA (green) inside NPs. (E) Antigen cross-presentation induced by OVA@$CaCO_3$ NP-related lysosome escape and autophagy. (F) The OVA@$CaCO_3$ NP/NB (traditional $CaCO_3$ nanobulk (NB, 500 nm, lamellae stacking, calcite crystal form)) dissolution mechanism. (F) TEM images and a corresponding scheme illustrating lysosome escape and autophagy. Reprinted from ref. 40. Copyright (2018), with permission from John Wiley and Sons under the terms of the Creative Commons Attribution Non-Commercial (CC BY-NC 3.0) License.

dissolution of $CaCO_3$ induces physical stress and autophagy *via* the LC3/Beclin 1 pathways.

4.5 Microenvironment-activated $CaCO_3$-containing nanocomposites as diagnostic and therapeutic agents

4.5.1 Multi-modality imaging-guided therapy. The development of activatable $CaCO_3$-based nanoplatforms can reduce side effects while improving diagnostic and therapeutic performance, which is highly attractive for precision cancer treatment. $CaCO_3$ combined with ICG can allow the integration of US and fluorescence imaging into one diagnostic nanoplatform for dual-modality imaging-guided therapy. To this aim, $CaCO_3$ NPs were encapsulated with DOX and ICG to form $CaCO_3$–DOX/ICG NPs.[56] The smart pH-responsive $CaCO_3$–DOX/ICG NPs were shown to significantly inhibit tumor growth enhanced US imaging by triggering the effective release of DOX with CO_2 bubble generation under an acidic TME. Furthermore, the encapsulation of ICG allowed detection of the tumor using fluorescence. Thus, these

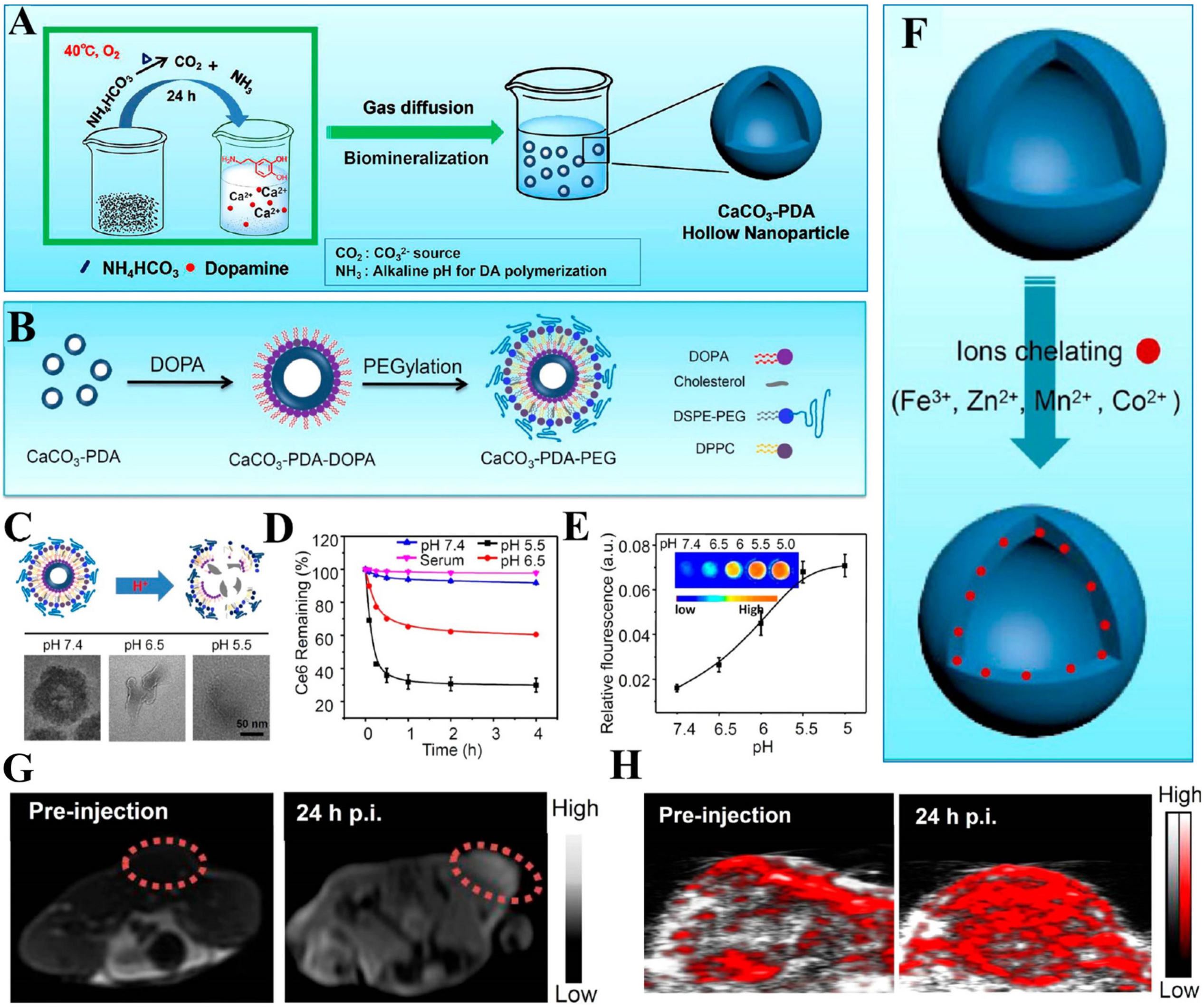

Fig. 22 Schematic diagram showing preparation and application of $CaCO_3$–PDA–PEG hollow NPs as a tumor acidic pH-activatable nanoplatform for multimodal imaging-guided cancer therapy. (A) Synthesis of $CaCO_3$–PDA. (B) The PEGylation process of $CaCO_3$–PDA. (C) The acid-responsive decomposition of $CaCO_3$–PDA–PEG NPs and their corresponding TEM images after incubation in PBS at three different pH levels for 2 h. (D) Time-dependent release profiles of Ce6 from Ce6@$CaCO_3$–PDA–PEG incubated in PBS or serum at different pH levels. (E) pH-dependent fluorescence intensity of Ce6@$CaCO_3$–PDA–PEG after being incubated in PBS at various pH levels for 2 h. The inset shows the corresponding fluorescence image. (F) The metal ion-doping process of $CaCO_3$–PDA–PEG. (G) T_1-weighted MR images of 4T_1 tumors taken before injection (left) and 24 h after i.v. injection (right) of $CaCO_3$–PDA(Mn)–PEG. (H) Photoacoustic images of 4T_1 tumors taken before injection (left) and 24 h after i.v. injection (right) of $CaCO_3$–PDA–PEG. Ce6: chlorin e6; PDA: polydopamine; PEG: polyethylene glycol. Reprinted with permission from ref. 42. Copyright (2018) American Chemical Society.

theranostic NPs are promising for use in US and fluorescence dual-modal imaging and cancer treatment.

To further enrich the properties of $CaCO_3$, surface modification is an effective strategy by which to prepare a multifunctional $CaCO_3$ diagnostic and therapeutic nanoplatform. The hollow $CaCO_3$–PDA nanocomposite was prepared *via* a one-pot, dopamine-mediated biomineralization inspired method using a gas diffusion procedure (Fig. 22A).[42] The as-synthesized $CaCO_3$–PDA was then modified with PEG and loaded with the effective photosensitizer chlorin e6 (Ce6) to form Ce6@$CaCO_3$–PDA–PEG hollow NPs (Fig. 22B). The photoactivity of the loaded Ce6 was quenched by the strong absorption of PDA at neutral pH, which was activated with recovered fluorescence and improved singlet oxygen generation ability at reduced pH within the TME (Fig. 22C–E). These Ce6@$CaCO_3$–PDA–PEG hollow NPs are thus promising for use in fluorescence imaging-guided cancer PDT with reduced skin phototoxicity. In addition, the M-loaded (M = Fe^{3+}, Zn^{2+}, Mn^{2+}, or Co^{2+}) $CaCO_3$–PDA–PEG NPs were formed NPs *via* metal ion chelation and then modified with PEG (Fig. 22F), with the resultant material showing excellent T_1-contrasting ability for PAI (Fig. 22H). In particular, the $CaCO_3$–PDA–PEG hollow NPs allow the simultaneous loading of both imaging (*e.g.*, Mn^{2+}) and therapeutic molecules (*e.g.*, Ce6) for fluorescence/MRI/PAI-guided cancer therapy (Fig. 22E, G and H).

4.5.2 US imaging and therapy. US is used to destroy necrosis-mediated tumors. In this process, a pH-sensitive $CaCO_3$-containing nanocomposite can be used to induce necrotic cell death by releasing CO_2 bubbles at the tumor site, thus exhibiting anticancer activity. Cancer-targeting and gas-generating NPs (RVG–GNPs) have been successfully constructed by encapsulating $CaCO_3$ into poly(D,L-lactide-coglycolide) and then modifying this with the rabies virus glycoprotein (RVG) peptide.[54] When gas-generating $CaCO_3$-based NPs are modified using the RVG peptide, a targeting moiety for neuroblastoma, the resultant RVG–GNPs effectively accumulate at the tumor site and generate CO_2 gas bubbles under acidic tumor conditions to enhance ultrasound imaging signals. In addition, intravenous administration of RVG–GNPs without the use of other therapeutic agents can inhibit tumor growth *via* the release of CO_2 bubbles $CaCO_3$ NPs can be integrated with therapeutic agents such as a chemotherapeutic drug and photosensitizer to form multifunctional theranostic nanoplatforms. As an example, DOX-loaded $CaCO_3$ hybrid NPs (DOX– $CaCO_3$–MNPs) have been developed using a block copolymer (PEG-*b*-poly(L-aspartic acid) (PEG–PAsp)) *via* a mineral-nucleating and growth template *in situ* mineralization approach (Fig. 23A).[222] The $CaCO_3$ NPs serve not only as a CO_2 bubble-generating precursor for ultrasound imaging but also as a cargo for the stable loading of DOX. The DOX–$CaCO_3$–MNPs exhibit effective antitumor therapeutic activity (Fig. 23E) by triggering DOX release simultaneously with CO_2 bubble generation in the TME (pH 6.8–7.2) (Fig. 23B and C) and strong echogenic signals (Fig. 23D), thus making it an excellent theranostic agent for simultaneous US imaging and therapeutic functions.

The combination of $CaCO_3$-based US imaging and PDT functions into a rationally designed nanoplatform can allow the realization of the real-time monitoring of PDT. Ce6-Loaded bubble-generating mineralized NPs (Ce6-BMNs) comprising a Ce6-loaded $CaCO_3$ core and hydrated PEG shell were fabricated for US imaging and PDT.[223] The Ce6-BMNs effectively inhibited Ce6 release at physiological pH (7.4) and generated CO_2 gas bubbles, simultaneously triggering the release of Ce6 at tumoral acidic pH for contrast-enhanced diagnostic US imaging and NIR-absorbing photosensitizers for remote PDT. Moreover, Ce6 release can be accelerated with CO_2 bubble generation due to the dissolution of the $CaCO_3$ mineral core in the tumoral environment, enhancing the delivery efficacy of Ce6 and the generation of singlet oxygen into the TME.

4.5.3 Fluorescence imaging and therapy. $CaCO_3$-Based nanocomposites with a combination of drug-loaded $CaCO_3$ and inorganic nanomaterials (carbon dots) or organic fluorophores (*e.g.*, tetracycline,[44] Ce6,[42] and ICG[56]) can be activated by tumor-specific endogenous stimuli. For instance, a porous

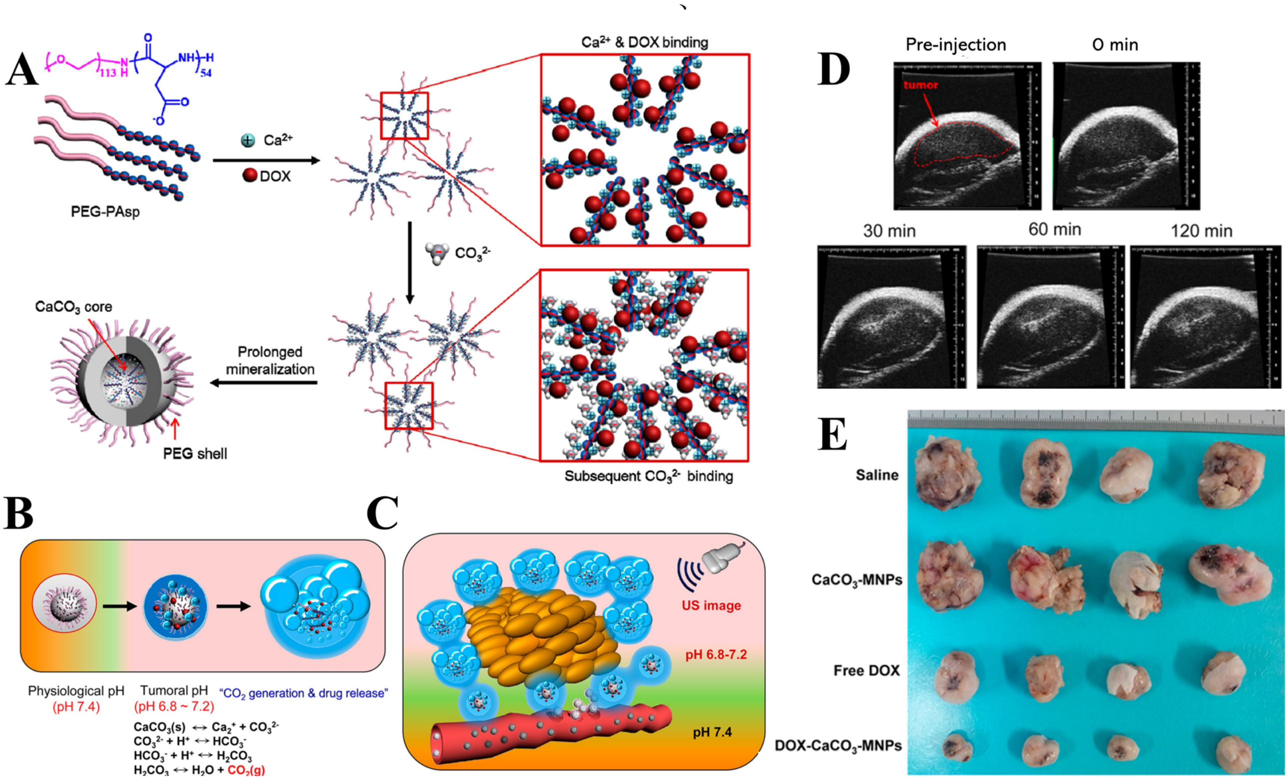

Fig. 23 Schematic diagram of DOX–$CaCO_3$–MNPs for simultaneous ultrasound imaging and therapy. (A) Fabrication process of the DOX–$CaCO_3$–MNPs. (B) Mechanism of the CO_2 generation and drug release of the DOX–$CaCO_3$–MNPs. (C) Bubble generation and drug release after the accumulation of DOX–$CaCO_3$–MNPs in tumor tissue. (D) *In vivo* US imaging of a squamous cell carcinoma tumor *via* the intratumoral injection of the DOX–$CaCO_3$–MNPs. (E) Images of excised tumors of each group with controls (saline and $CaCO_3$–MNPs), free DOX, and the DOX–$CaCO_3$–MNPs 16 days post-treatment. Reprinted with permission from ref. 222. Copyright (2015) American Chemical Society.

carbon dot–PAA–$CaCO_3$ nanocomposite has been designed[293] in which the fluorescent carbon dots not only serve as a template for the crystallization and assembly of $CaCO_3$, but also have fluorescence properties and are very small in size. The carbon dot–PAA–$CaCO_3$ nanocomposite was found to be porous with a rough surface, exhibiting colloidal stability in cell medium and non-cytotoxicity. Therefore, this nanocomposite allowed for the occlusion of anticancer drugs within the $CaCO_3$ matrix, making it a material that holds great potential for fluorescence imaging-guided therapy. Moreover, a fluorescence imaging-guided therapy nanoplatform can be constructed by integrating drug-loaded $CaCO_3$ NPs with an organic fluorophore. A facile one-pot encapsulation stragety *via* the macromolecular assembly of an anionic polypeptide with a cationic peptide oligomer was developed for the *in situ* encapsulation of tetracycline in a $CaCO_3$ microstructure.[44] These tetracycline-loaded $CaCO_3$ microspheres exhibited pH-sensitive *in vitro* drug release profiles and antibacterial activity for cancer therapy applications. In addition, the encapsulated tetracycline or the dye-conjugated peptide emitted fluorescence suitable for detecting and locating malignant tissue, thereby making tetracycline-loaded $CaCO_3$ microspheres an ideal fluorescence imaging-guided therapy nanoplatform.

4.5.4 MRI and therapy. By integrating $CaCO_3$ NPs with the MRI element Mn and a chemotherapeutic agent, a tumor-pH-responsive $CaCO_3$-containing nanoplatform enables real-time release monitoring and combination treatment of cancer. Dong *et al.*[55] developed mono-dispersed PEG-modified $CaCO_3$ NPs as a multifunctional nanocarrier for loading with both a photosensitizer (Mn^{2+}-chelated Ce6 (Ce6(Mn))) and chemotherapeutic drug (DOX) (Fig. 24A). The $CaCO_3$@Ce6(Mn)–PEG(DOX) NPs were found to be stable at a physiological pH of 7.4, whereas they were shown to be highly sensitive to reduced pH and rapidly degraded in a slightly acidic environment, resulting in effective release of the loaded Ce6(Mn) and DOX (Fig. 24B and C). These NPs exhibited pH-dependent T_1 signal enhancement

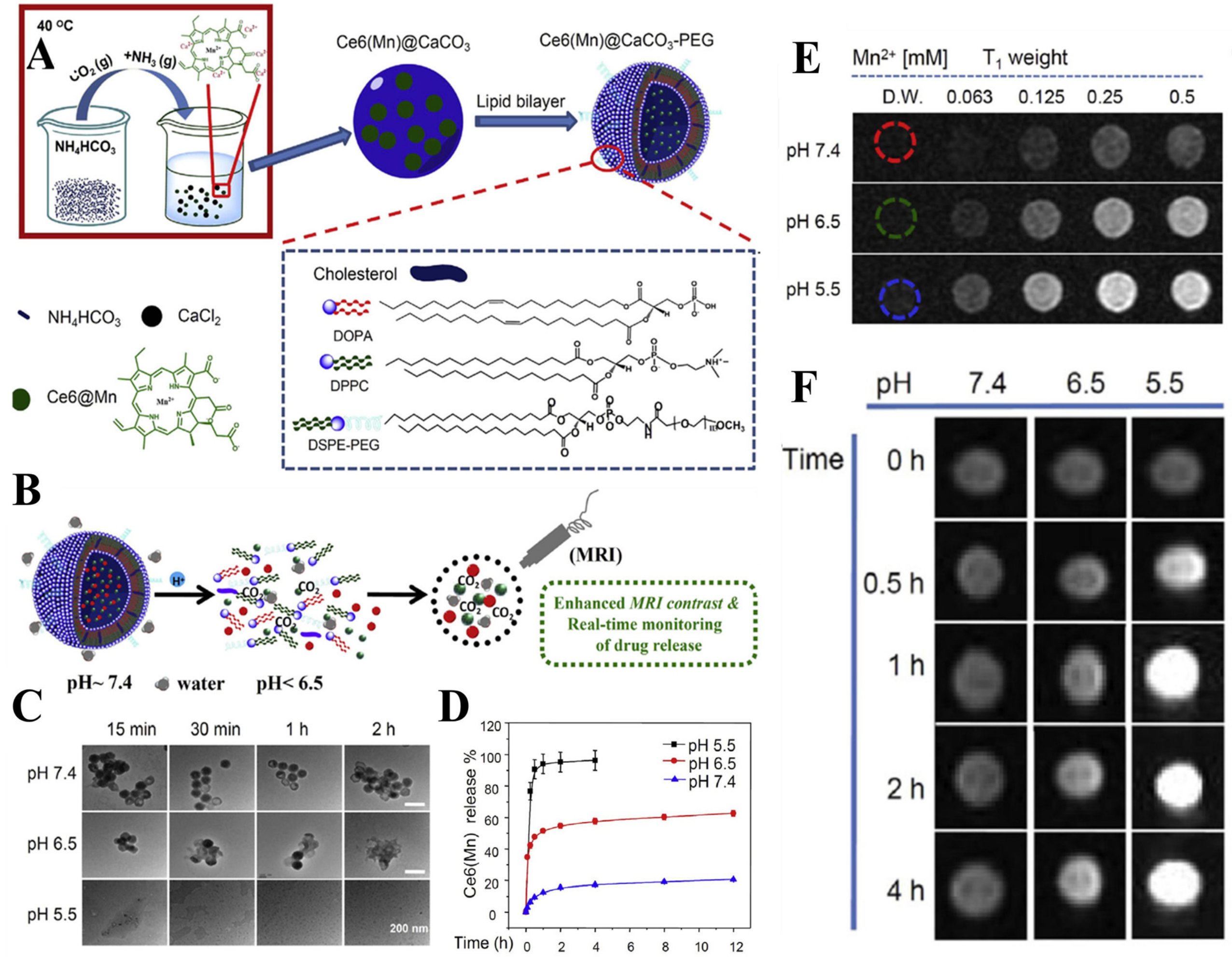

Fig. 24 Schematic diagram of Ce6(Mn)@$CaCO_3$–PEG NPs for MRI-monitored drug release. (A) Synthesis and structure of the Ce6(Mn)@$CaCO_3$–PEG NPs. (B) pH-responsive decomposition of the Ce6(Mn)@$CaCO_3$–PEG NPs. (C) TEM images of the Ce6(Mn)@$CaCO_3$–PEG NPs after being immersed in PBS at three different pH levels. (D) Time-dependent Ce6(Mn) release from the NPs Ce6(Mn)@$CaCO_3$–PEG NPs in PBS at different pH levels. (E) T_1 relaxivities of Ce6(Mn)@$CaCO_3$–PEG at different pH levels. (F) Time-dependent T_1 MR images of Ce6(Mn)@$CaCO_3$–PEG(DOX) after incubation in PBS at different pH levels. Reprinted from ref. 55. Copyright (2016), with permission from Elsevier.

in MRI due to the release of Ce6(Mn) (Fig. 24D–F), which was utilized for the real-time monitoring of the drug release. By combining chemotherapy with PDT, the acidic pH-activated theranostic nanoplatform based on $CaCO_3$ NPs shows excellent synergistic anti-tumor effects to realize MRI-guided cancer therapy.

5. $CaCO_3$ for mimetic nacre composites

In nature, living organisms can produce hierarchically structured lightweight $CaCO_3$-based materials with outstanding structures, good stiffness, remarkable strength, and toughness.[7] Such organisms include mollusks, echinoderms, calcisponges, corals, and certain types of algae.[6,20,297,298] Recent studies have revealed that $CaCO_3$ plays a role in the integrated visual system of chitons,[299] in the bioceramic hard buoyancy tanks of cuttlefish,[8] and in both the light-focusing eye lenses and mechanical support of brittlestars.[9] More recently, Li *et al.*[300] discovered that high-magnesium calcite [$CaMg(CO_3)_2$] armor overlays the exoskeletons of major workers of the leaf-cutter ant *Acromyrmex echinatior*, affording them mechanical protection. Nacre (mother-of-pearl) is a lightweight hierarchically $CaCO_3$-based material with high strength and toughness, which has been the subject of much research attention toward the preparation of macroscopic artificial materials that mimic its micro/nanostructure.[301,302]

It is well-known that nacre, the pearly internal layer of many mollusk shells, exhibits a bricks-and-mortar structure comprising 95% aragonite and 5% organic components (proteins and polysaccharides) by volume (Fig. 25).[294] Nacre is formed by the deposition of crystal precursors (Ca^{2+} and CO_3^{2-}) as well as ACC to form aragonite tablets on the surface of an insoluble matrix under the regulation of soluble biomacromolecules such as polysaccharides and proteins (Fig. 25B).[296] The aragonite tablets and thin sheets of organic matrix are alternately arranged to form a highly organized, 'bricks-and-mortar' or 'brick-wall' microstructure,[294] wherein each aragonite-rich plate is uniformly aligned vertically in the *c*-axis [001] direction (Fig. 25A). The organization of aragonite tablets and organic composites in the nacre and the formed hierarchical structure have been shown to significantly increase the toughness of nacre composites.[303] For example, the shell of *Strombus gigas* comprises 99% aragonite and 1% organic phase (proteins and chitin) by volume. The nacre in this shell with a "crossed lamellar microarchitecture" is 3000 times tougher than single crystals of aragonite.[303,304]

The outstanding mechanical properties of $CaCO_3$-based nacre materials can be primarily attributed to two key factors. First, the fractions of the stiff minerals such as aragonite within the nacres are relatively high. Second, the aragonite is typically assembled into ordered microstructures to slow crack propagation.[305] Stimulated by the remarkable mechanical performance of such a nacre, significant efforts have made to biomimetically engineer $CaCO_3$ materials into hierarchical structured composites that exhibit exceptional stiffness, strength, and toughness.[306] Over the past few decades, many nacre-inspired structural materials have indeed been synthesized.[307–309] The strategies used to prepare these materials can be categorized as self-assembly,[310,311] layer-by-layer,[312] and freezing-induced assembly-and-mineralization techniques.[313,314] The focus here is on studies and advances made over the last decade or so in using $CaCO_3$ as an inorganic building block to produce nacre mimetic materials. Self-assembly seems to be a promising and economical strategy for the large-scale production of $CaCO_3$-based nacre.

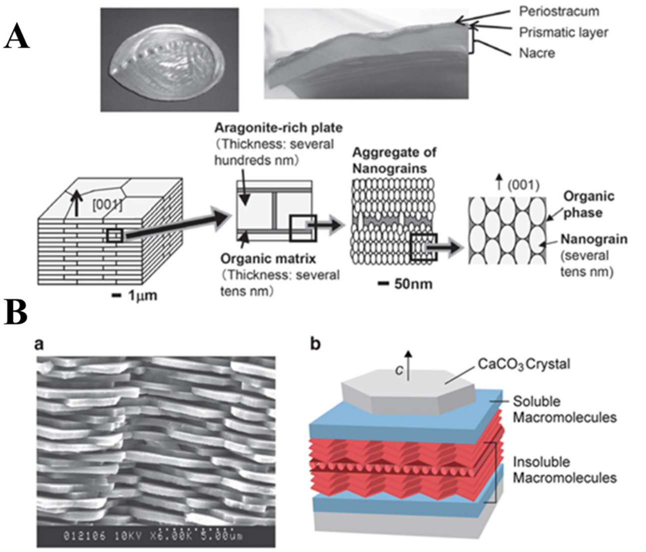

Fig. 25 Schematic diagram showing the bricks-and-mortar structure of nacre. (A) Photographs of the abalone H. gigantea: bottom view (top left) and cross-section (top right) showing nacre at the inner surface. The platelet consists of 'nanograins,' aragonite particles on the order of several tens of nanometers, and the organic phase surrounding the nanograins. Reprinted from ref. 294. Copyright (2011), with permission from National Institute for Materials Science. (B) (a) Scanning electron microscopy (SEM) image of the fractured nacre. (b) Schematic illustration of the composite structure of nacre. Reprinted from ref. 295 and 296. Copyright (2000), with permission from John Wiley and Sons under the terms of the Creative Commons Attribution Non-Commercial (CC BY-NC 3.0) License.

The challenging issue in this arena lies in the lack of methods available for preparing $CaCO_3$ in a thin tablet form with a thickness of <500 nm.[315] Li *et al.*[315] developed a vacuum-evaporation-induced self-assembly method by which to synthesize single-crystalline $CaCO_3$ nanotablets in large quantities as primary building blocks for constructing nacreous inorganic–organic hybrid films. The $CaCO_3$ NPs were first obtained in the presence of CTAB ($R–N^+–(CH_3)_3$) and polyoxyethylene sorbitan monolaurate surfactants in a water–ethylene glycol co-solvent. The $CaCO_3$ NPs were in the size range of 1–3 nm and appeared to be stable for months in a mixed water/ethylene glycol solution. When $CaCO_3$ NPs were prepared in the absence of surfactants, $CaCO_3$ nanotablets were formed instantaneously. It was suggested that the formation of $CaCO_3$ nanotablets could be formed during the washing treatment of $CaCO_3$ NPs. Nacre-like $CaCO_3$–gelatine inorganic–organic hybrid films have also been prepared using $CaCO_3$ nanotablets as inorganic building blocks and gelatine (a protein derived from bovine skin) as a gluing matrix *via* a casting-then-assembling process. Typically, the ultimate tensile strength of the prepared $CaCO_3$ (33 wt%)–gelatine films is around 97 MPa, comparable to that of nacre.

A layer-by-layer deposition method has been used to combine hard inorganic $CaCO_3$ NPs with a soft organic phase in the design of a multilayered material featuring precisely ordered nanoscale building blocks.[306] By mimicking the natural layer-by-layer approach employed to fabricate nacre, Finnemore and coworkers used the interplay between polymer-mediated $CaCO_3$ growth and the layer-by-layer deposition of porous organic films to successfully replicate nacre for the first time using $CaCO_3$.[312] Use of an $(NH_4)_2CO_3$ diffusion technique employing a PAA-containing aqueous solution of $CaCl_2$ and $MgCl_2$ yielded stable polymer-induced liquid precursor droplets, which were used to wet a carboxyl-terminated substrate and coalesce into an ACC film rich in Mg and PAA (Fig. 26A). The ACC was then crystallized by exposure to high humidity, resulting in a calcite structure featuring stacked crystalline layers interconnected with porous organic films. An advantage of this approach to prepare artificial nacre is the fabrication of the porous organic inter-crystalline layers (Fig. 26A). These pores allow the propagation of the crystallization of $CaCO_3$ across the organic layers, providing vertical crystalline $CaCO_3$ continuity, which enhances the mechanical stability of the resultant nacre. In terms of its morphology, growth route, and iridescence, the artificial nacre prepared was found to be comparable to natural nacre (compare Fig. 26B–a–c with d–g). In particular, a comparison of the SEM image of the fractured surfaces of natural (Fig. 26B-b) and artificial (Fig. 26B–e) nacre reveal very similar multilayers of 400 nm-thick calcite tablets with a nanogranular texture, characteristic of nacre.

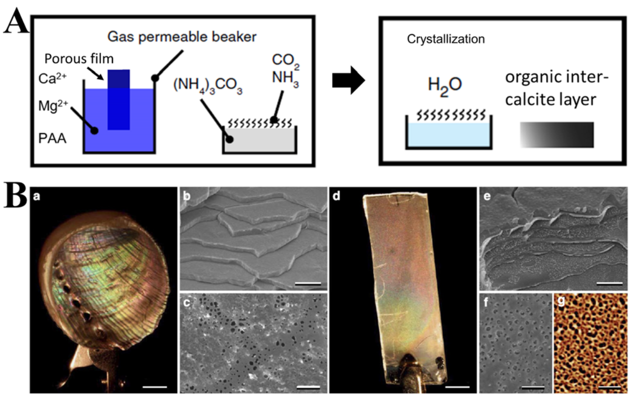

Fig. 26 Biomimetic layer-by-layer assembly of artificial nacre. (A) Artificial nacre synthesis. (B) Comparison between biogenic and artificial nacre. (a) Photograph showing the bright iridescence of nacre. (b) Fractured surface SEM image of a stack of mineral tablets. (c) Organic inter-crystalline film that allows for vertical crystal continuity between tablets. (d) Artificial nacre, exhibiting a similar coloration to that in (a). (e) SEM image of a fractured surface showing seven aligned CaCO3 tablets separated by organic films. f) SEM image of a polymer (PVP) film on calcite showing a similar pore distribution to that in (c). (g) Atomic force microscopy (AFM) height image of the porous film. Adapted and reprinted by permission from [Springer Nature Customer Service Centre GmbH]: [Springer Nature]: [ref. 312], [Copyright] (2012).

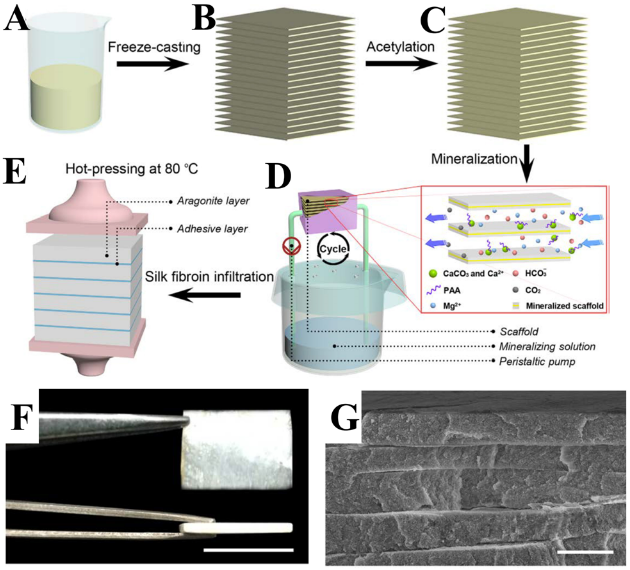

Fig. 27 Schematic diagram showing fabrication scheme of the synthetic nacre. (A) Starting solution, chitosan/acetic acid solution. (B) Freeze-casted laminated chitosan matrix. (C) Matrix after acetylation, where chitosan is converted to β-chitin. (D) Mineralization of the matrix. (E) Laminated synthetic nacre is obtained after silk fibroin-infiltration and hot-pressing processes. (F) The as-prepared synthetic nacre. (G) SEM image of a cross section of the synthetic nacre. Scale bar: 1 cm for F; 3 mm for G. From ref. 314. Copyright (2016), Adapted and reprinted with permission from AAAS.

Considering that mollusks construct their nacre *via* mineralization in a preformed laminated matrix, Mao and colleagues developed a freezing-induced assembly-and-mineralization process (Fig. 27) to fabricate $CaCO_3$-based nacre-like materials using mesoscale tactics in which the nanostructure and the microstructure are controlled simultaneously.[314] Using a freezing-induced assembly process (Fig. 27A and B), a chitosan matrix with a predesigned laminated structure was fabricated, which was subsequently acetylated (Fig. 27C) and transformed to β-chitin to avoid unnecessary swelling or dissolution. The acetylated matrix was then mineralized in the presence of PAA and Mg^{2+} by decomposing $Ca(HCO_3)_2$ in a peristaltic pump-driven circulatory system (Fig. 27D). Synthetic nacre was finally obtained *via* silk fibroin infiltration and hot-pressing of the mineralized chitin matrix (Fig. 27E). The resultant millimeter-thick synthetic nacre comprised alternating organic layers and aragonite platelet layers (91 wt%), exhibiting remarkable ultimate strength and fracture toughness (Fig. 27F and G).

6. Engineering $CaCO_3$ into environmental and energy nanostructured materials

6.1 Environmental remediation

6.1.1 Heavy metal ion remediation. Currently, due to its simple operation and high efficiency, adsorption methods are most widely used for the remediation of wastewater.[316] In such processes, ion exchange occurs between $CaCO_3$ and heavy metal ions, followed by MCO_3 (M: metal ion) precipitation.[317] Based on this principle, $CaCO_3$ has been used to remove various metal ions from water, including Hg^{2+},[318] Pb^{2+},[316,319,320] Ni^{2+},[321] Cd^{2+},[322] Cr^{3+},[323] Fe^{3+},[67] Mn^{2+},[324] and Cu^{2+}.[324] In addition, $CaCO_3$ has been combined with magnetic NPs to form $CaCO_3$/magnetic composite materials for the effective removal of heavy metal ions from water, with such materials being easy to separation from solution and reuse. Hierarchical meso-/microporous $CaCO_3$ as an adsorbent exhibits excellent adsorption due to its high specific surface area and mass transport that occurs through its large pore channels.[325]

$CaCO_3$ removes heavy metals from wastewater primarily *via* adsorption and precipitation processes. At a low metal concentration, the adsorption process mainly occurs *via* the replacement of Ca^{2+} by heavy metal ions,[326] whereas at high metal concentrations the precipitation process is dominant.[327] Traditional wastewater treatment with $CaCO_3$ from geological sources (geo-$CaCO_3$, *e.g.*, calcite and aragonite) can reduce the residual Pb^{2+} content of the water to 1 mg L^{-1}. Yet, there are still issues in using this material to meet the new standards stipulated by the Centers for Disease Control & Prevention, which are that discharge must contain no more than 0.05 mg L^{-1} of Pb^{2+}.[328] Geo-$CaCO_3$ has an intrinsically dense crystal structure, which results in it exhibiting low pollutant removal efficiency and the potential to generate a significant amount of sludge. Recent studies have shown that biogenic $CaCO_3$ (bio-$CaCO_3$) derived from marine shells, eggshells, and oyster shells, exhibits better performance than geo-$CaCO_3$ in terms of wastewater treatment, especially in improved Pb^{2+} removal efficiency and producing less sludge.[323,326,329] The hierarchical porous organic–inorganic hybrid structure of bio-$CaCO_3$ allows deeper penetration of Pb^{2+} into the $CaCO_3$ material *via* pores/slits in the particles, with it eventually becoming immobilized. Meanwhile, the organic functional groups of bio-$CaCO_3$ (*e.g.*, –COOH) assist in the adsorption of Pb^{2+} (Fig. 28A). For example, bio-$CaCO_3$ derived from oyster shells shows remarkable performance in removing Pb^{2+} from wastewater.[326] Since to some extent Ca^{2+} and $CO_3{}^{2-}$ are dissolved on the surface of $CaCO_3$, the generation of $CO_3{}^{2-}$ leads to the supersaturation of Pb^{2+}, thus favoring the nucleation and growth of $PbCO_3$ and $Pb_3(CO_3)_2(OH)_2$. Pb^{2+} forms a complex with the functional groups of bio-$CaCO_3$, followed by the interaction of Pb^{2+} with the bio-$CaCO_3$. As a result, the maximum adsorption capacity of bio-$CaCO_3$ toward Pb^{2+} is three times that of geo-$CaCO_3$, reaching 1667 mg g^{-1}. The adsorption of Cd^{2+} on bio-$CaCO_3$ ($CaCO_3$ formed by *Bacillus subtilis*) is a spontaneous endothermic process that can be described in terms of its kinetics as a pseudo-second order process.[322] Similarly, during the removal of heavy metal ions from water, $CaCO_3$ in the form of vaterite continuously releases Ca^{2+} due to participating in an ion exchange reaction with metal ions.

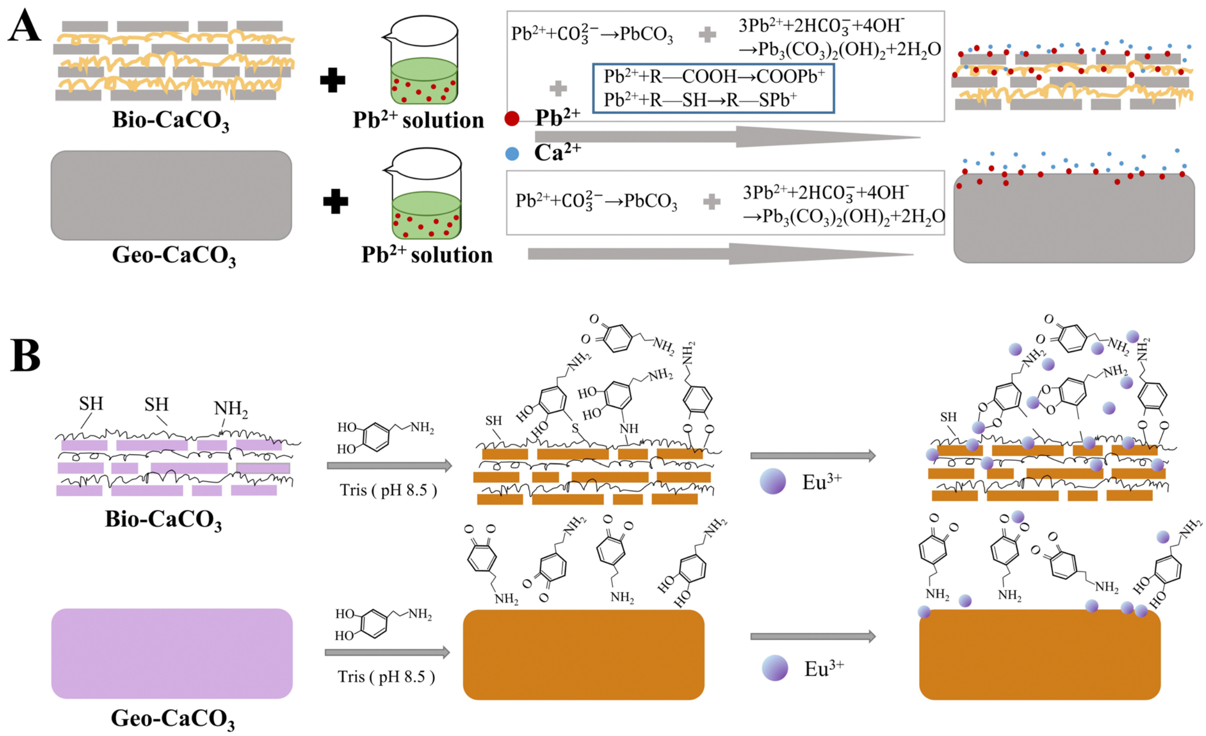

Fig. 28 Schematic diagram illustrating bio-$CaCO_3$ with a hierarchical organic–inorganic composite structure that enhances the removal of metal ions from wastewater. (A) Schematic illustration of Pb^{2+} sequestration on bio-$CaCO_3$ and geo-$CaCO_3$. Reprinted and adapted with permission from ref. 326. Copyright (2017) American Chemical Society. (B) Schematic illustration of PDA coating on bio-$CaCO_3$ and geo-$CaCO_3$, and the corresponding Eu^{3+} adsorption mechanism. Reprinted and adapted from ref. 330. Copyright (2018), with permission from Elsevier.

In this process, Pb^{2+} and Ca^{2+} ions exchange and recrystallize. For this reason, vaterite prepared from oyster shells exhibits the following removal efficiencies for ions: Pb^{2+} (99.9%), Cr^{3+} (99.5%), Fe^{3+} (99.3%), and Cu^{2+} (57.1%).[323] The organic–inorganic hierarchical microstructure and organic matter of bio-$CaCO_3$ are conducive to the adsorption of rare earth elements, resulting in rare earth elements being recycled from wastewater. Recently, taking the advantages of mussel-inspired PDA chemistry, Zhou *et al.*[330] modified the surface of bio-$CaCO_3$ from waste oyster shells with PDA *via* a facile oxidative polymerization route to increase its organic matter content, and eventually promote its Eu^{3+} adsorption capacity. The anti-oxidation properties of the organic matter of amino- or thiol-containing molecules of the groups used to modify bio-$CaCO_3$, as well as the high surface area provided by bio-$CaCO_3$ hierarchical structure, significantly improve the affinity of PDA to bio-$CaCO_3$ (Fig. 28B), which is anchored on bio-$CaCO_3$ *via* bidentate metal coordination. The abundant catechol and amine groups of the uniform PDA coating on bio-$CaCO_3$ are then able to capture a large amount of Eu^{3+} ions from solution. In contrast, the surface of geo-$CaCO_3$ is smooth, with only a few dopamine molecules anchored on its tight surface.

As for the adsorption and precipitation of heavy metals on $CaCO_3$ surfaces, a puzzling issue is that generally $CaCO_3$ is hard to dissolve ($K_{sp} = 3.36 \times 10^{-9}$), and thus only slowly reacts with metal ions.[325,331] Such low level of potential interaction means that a large amount of $CaCO_3$ has to be used in an application to achieve a high removal efficiency. A recent study demonstrated that ball milling can be used to improve the reactivity of $CaCO_3$ with Pb^{2+}.[209] During the ball milling process, the surface of $CaCO_3$ is constantly activated due to continuous mechanical collisions, extrusion, and shearing. The originally stable $CaCO_3$ is thus broken up into smaller particles with more active fresh surfaces exposed, thus improving its solubility and chemical reactivity in solution. In the ball milling process, CO_3^{2-} generated from the hydrolysis of $CaCO_3$ ($K_{sp} = 3.36 \times 10^{-9}$) was reacted with Pb^{2+} from acidic mine drainage to form the more stable material $PbCO_3$ ($K_{sp} = 7.40 \times 10^{-14}$). This process allowed less $CaCO_3$ to be used to achieve effective Pb^{2+} removal from the drainage and also led to less sludge being produced. However, the reactivity of the activated $CaCO_3$ was not sufficient to precipitate Zn^{2+} ($ZnCO_3$, $K_{sp} = 1.46 \times 10^{-10}$) at the same time. Such a difference might lead to the development of a new way of efficiently separating Pb^{2+} from Zn^{2+}.

In addition, different crystal structures of $CaCO_3$ exhibit different electron densities around the Ca atoms. As such, this inevitably affects the replacement of Ca atoms by heavy metal ions. This has been evidenced in a few new studies that have shown that crystal phase is related to both reactivity with and selectivity toward heavy metal ions.[323,332,333] Magnetic mesoporous $CaCO_3$ nanocomposites (MCCRs) with vaterite and aragonite phases exhibit stronger adsorption ability toward Cd^{2+} than for Pb^{2+}, while MCCRs with a calcite phase show better adsorption of Pb^{2+} than Cd^{2+}.[316] These adsorption differences may be mainly due to the different degrees of matching of the crystal lattice between Pb^{2+}- and Cd^{2+}-bearing precipitates and the different crystal phases of $CaCO_3$. These findings provide valuable information for the design and enhancement in the reactivity and selectivity of $CaCO_3$-based adsorbents toward heavy metal ions for application in environmental remediation.

$CaCO_3$/porous carbon composites are harmless to humans and hold the potential to be used in the removal of heavy metals from water and soil. A hierarchical porous carbon sorbent has recently been successfully fabricated *via* the pyrolysis of rice straw in the presence of $CaCO_3$ NPs for the effective removal of metal ions from water.[334] The calcite–biochar composites prepared at 700 °C exhibit the efficient removal of Pb (99.9%). In the process, calcite acted as a catalyst for the catalytic carbonization of biochar and contributed toward changes in yield, pH, texture, and the surface functional groups of the $CaCO_3$–biochar composites. For the calcite–biochar composites, calcite formed a stronger bond with Pb under alkaline conditions. Upon an increase in pH in aqueous solution, more Pb^{2+} was likely to be precipitated by the CO_3^{2-} of the calcite.

A common challenge when using $CaCO_3$-based adsorbents is that they are difficult to separate from wastewater after use and often require further treatment of the sludge to be retrieved. To tackle this issue, a carbonate-based mesoporous magnetic adsorbent (IO@$CaCO_3$) consisting of needle-like iron oxide (IO) and calcite was synthesized *via* a hydrothermal synthetic strategy by Islam *et al.*[317] Due to synergistic effects between needle-like IO and $CaCO_3$, the IO@$CaCO_3$ material almost completely removed (99.99%) heavy metal ions from wastewater in only 9 min. The adsorption of the metal ions on IO@$CaCO_3$ was attributed to a specific adsorption mechanism (instead of non-specific Coulombic attraction), such as ion-exchange reactions that take place between the anionic metal ions (Cr(VI) and As(V)) and anionic surface groups (OH^- and CO_3^{2-}) or between the cationic metal ions (Pb^{2+}) and cations (Ca^{2+}) on the surface of the IO@$CaCO_3$ adsorbent. As it is magnetic, IO@$CaCO_3$ can be easily separated from solution using an external magnetic field, enabling it to be effectively recycled.

6.1.2 Phosphate removal and recovery. Excessive release of phosphate into bodies of water has led to eutrophication and the formation of algal blooms. In water, the Ca^{2+} of $CaCO_3$ combine with phosphate ions to form a stable precipitation of CaP ($Ca_3(PO_4)_2$). Electrochemical processes offer a membrane-free method of removing phosphate from water. However, in such a process described in the literature, the recombination of anode-produced protons (H^+) with cathode-generated hydroxide ions (OH^-) resulted in low removal efficiency of phosphate and long retention.[335] The introduction of $CaCO_3$, a byproduct from water softening processes, into a column-shaped electrochemical precipitation reactor, which was in contact with/or close to the anode, reacted with electrochemically produced H^+.[336] The $CaCO_3$ NPs facilitated $Ca_3(PO_4)_2$ precipitation by buffering the H^+ formed at the anode, releasing Ca^{2+}, which acted as a seed to establish a high pH environment in bulk solution in addition to in the vicinity of the cathode. Otherwise, this relatively low energy consumption (29–61 kW h kg^{-1} P) of the $CaCO_3$ packed electrochemical precipitation column has been used to overcome direct H^+–OH^- recombination.[337] This $CaCO_3$ packed electrochemical precipitation has shed light on a novel alternative to remove and recover phosphate from wastewater.[337]

Many ions can potentially interfere with the removal of phosphate from water. The hydrolysis of $CaCO_3$ results in cationic species, such as Ca^{2+}, $CaHCO_3^+$, and $CaOH^+$, being produced at a pH of <8 ($CaCO_3 = Ca^{2+} + CO_3^{2-}$, p$K$ = 3.25; $CO_3^{2-} + H_2O = HCO_3^- + OH^-$, p$K$ = 3.67; $Ca^{2+} + HCO_3^- = CaHCO_3^+$, p$K$ = −0.82; $Ca^{2+} + OH^- = CaOH^+$, pK = −1.40). $CaCO_3$-based adsorbents have been developed for the removal of phosphate from water. An abundance of Ca^{2+} ions has been shown to facilitate the removal of phosphate ions from water in the presence of $CaCl_2$. In addition, biochar–calcite composites appeared to outperform calcite alone in the removal of phosphate ions from water. The reduced phosphate adsorption in the presence of HCO_3^- may have been due to the increased competition for adsorption sites from HCO_3^-. More recently, with the aim of removing and recovering phosphate from water, Zhou *et al.*[337] used calcite and rice husk biochar at a pyrolysis temperature of 700 °C, pyrolysis time of 2.3 h, and a rice husk: calcite ratio of 4.2 : 1 (w/w) to prepare a rice husk biochar–calcite composite. $CaCO_3$ was converted into CaO at a high pyrolysis temperature, which then reacted with SiO_2 to form a calcium silicate, wollastonite ($CaSiO_3$), and increased the distribution of active Ca ions. The $CaSiO_3$ may contribute to remove phosphate from aqueous media *via* the precipitation of phosphate to $CaHPO_4$ under acidic conditions or $Ca_3(PO_4)_2$ under neutral conditions. The removal of phosphate by the rice husk biochar–calcite composite was shown to occur synergistically *via* pore filling, electrostatic interactions, and precipitation. The design of ecofriendly and cost-effective $CaCO_3$-based composites is thus a promising approach by which to remove phosphate and other organic and inorganic pollutants from wastewater.

6.1.3 Oil–water separation. The occurrence of oil spills from petrochemical, food, and machinery manufacturing industries that pollute water poses a serious threat to the environmental ecosystem and human health.[340] Over the past few decades, $CaCO_3$ has been shown to have potential for use in oil–water separation materials owing to its environmental friendliness, intrinsic hydrophilicity, and superior biocompatibility.

Highly flexible free-standing $CaCO_3$ films with only 5% sodium alginate (NaAlg) have been developed for oil–water separation (Fig. 29A).[338] The free-standing $CaCO_3$ films were prepared by strongly mixing $CaCl_2$ and alginate together in water to form a Ca–Alg network, then Na_2CO_3 was added to the mixture to combine with Ca^{2+} to produce $CaCO_3$, followed by filtering to obtain $CaCO_3$/CaAlg hybrid films.[341] These $CaCO_3$/CaAlg hybrid films exhibit a coarse surface with micropores and hydrophilicity. The superhydrophilicity and the highly rough surfaces of the films result in them having underwater superoleophobic properties with ultralow oil adhesion. Hence, a self-cleaning function was realized when black crude oil that was adhered to a prewetted $CaCO_3$ film was easily removed after its immersion in water.

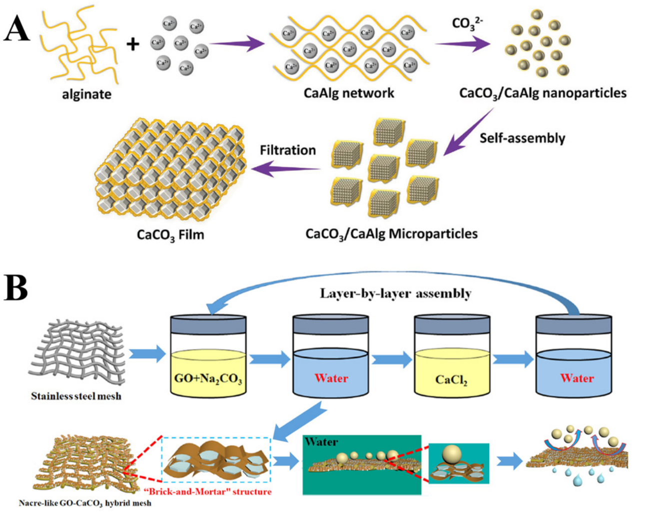

Fig. 29 Schematic diagram showing preparation of $CaCO_3$ hybrid materials for oil–water separation. (A) Flexible free-standing $CaCO_3$ film. Reprinted from ref. 338. Copyright (2017), with permission from John Wiley and Sons under the terms of the Creative Commons Attribution Non-Commercial (CC BY-NC 3.0) License. (B) A nacre-like graphene oxide (GO)–$CaCO_3$ hybrid mesh for oil–water separation. Reproduced with permission from ref. 339. Copyright (2020) American Chemical Society.

More recently, superhydrophilic/underwater superoleophobic cellulose films (FP@SA/$CaCO_3$) with good oil–water separation performance have also been developed.[342] Ca^{2+} was used to crosslink an SA film grafted on the surface of filter paper (FP) to improve the interface stability of the membrane. NaAlg–Ca was obtained *via* an ion-exchange mechanism between –COONa functional group and Ca^{2+} and the crosslinking reaction between the NaAlg molecular chains improved the stability of the material. During alternating soaking processes, the NaAlg–Ca coated composite membrane captured CO_3^{2-} to form $CaCO_3$ NPs, and the generated $CaCO_3$ NPs adhered stably to the membrane surface *via* NaAlg–Ca ionic bonds. $CaCO_3$ particles increase the surface roughness of FP@NaAlg/$CaCO_3$ films and are beneficial for promoting the superhydrophilicity of a material. For a petroleum ether–hexane–toluene–soybean oil–dichloroethane–water mixture, the separation efficiency of the FP@NaAlg/$CaCO_3$ films remained above 99% even after 20 cycles, indicating that they exhibit excellent stability and antifouling performance.

Furthermore, $CaCO_3$ can be formed on the surfaces of various meshes for the fabrication of superhydrophilic/superoleophobic $CaCO_3$-based hybrid films. The $CaCO_3$ coating of the surfaces of such hybrid films increases their dimensional stability, stiffness, and heat resistance.[342] On stainless steel mesh, a superhydrophilic and underwater superoleophobic GO–$CaCO_3$ hybrid mesh was fabricated *via* a layer-by-layer self-assembly method (Fig. 29B). Interestingly, the GO nanosheets in the material regulate the growth of the $CaCO_3$

nanocrystals between the GO oxide layers to construct ''bricks-and-mortar'' structures. The GO–$CaCO_3$ hybrid mesh exhibits strong mechanical properties, with a Young's modulus of 25.4 ± 2.6 GPa and a high separation efficiency of $>99\%$ toward a series of oil–water mixtures and a flux of 179 640 L m^{-2} h^{-1} for cyclohexane–water mixtures. A hierarchical $CaCO_3$ thin coating with structural continuity and uniformity has been deposited on a nylon mesh *via* seeded mineralization by the slow diffusion of CO_2 into $CaCl_2$ solution in the presence of PAA.[343] These hierarchical $CaCO_3$ thin coatings on the nylon mesh exhibit underwater superoleophobicity, very low adhesion of oil in water, and stiffness and strength similiar to the prismatic-type biominerals found in mollusc shells and can thus be employed in oil–water separation. This conventional mineralization process is complex and requires the pretreatment of the polymer surface and the addition of organic additives. Tang *et al.*[344] deposited $CaCO_3$ on stainless steel mesh *via* bacterially (*Bacillus subtilis*) induced biomineralization and subsequent surface modification with NaAlg. This bacterially-induced $CaCO_3$ biomineralization occurs at room temperature and in air without human intervention, thus representing an eco-friendly biomineralization strategy that is easy to conduct. The formed NaAlg/$CaCO_3$–stainless steel mesh with micro/nanostructured $CaCO_3$ coating and low surface energy exhibits oil fluxes in the range of $0.2–9.12 \times 10^4$ L m^{-2} h^{-1} and separation efficiencies of $>94.8\%$ toward various oil–water mixtures, showing great potential for use in oil–water applications under harsh conditions, such as slurry and dust environments, as well as at low temperature.

6.1.4 Removal of organic compounds. Waste shells (bio-$CaCO_3$) possess unique organic–inorganic hierarchical microstructures formed during biomineralization. It is thus important for researchers to consider the use of renewable $CaCO_3$ and green synthetic routes to create new $CaCO_3$ materials for environmental remediation. Murphy *et al.*[7] presented a renewable and absorbent $CaCO_3$ material in the form of soft calcite synthesized from waste blue mussel shells that exhibits a nest-like morphology. This material is soft and deformable with a texture like cotton candy and can absorb 1–24 wt% of common dyes from water, with both the dye and soft calcite recoverable *via* their complete desorption in methanol. Interestingly, soft calcite shows an absorption capacity of $977\% \pm 84\%$ for crude oil and recyclability over ten reuses.

Eggshell, which is composed of around 96% $CaCO_3$, can be used as a support and template upon which to immobilize metal NPs. For example, Ag NP-loaded eggshell catalysts have been prepared for the oxidation of volatile organic compounds.[345] The strong interaction between the Ag NPs and eggshell resulted in the decomposition temperature of the eggshell (*i.e.*, $CaCO_3$) being lower than that of pure eggshell. The layered eggshell membrane (proteins and polysaccharides) played a crucial role in the dispersion of Ag NPs on eggshell supports *via* strong metal–protein bonding interactions. The hierarchical porous structure of the eggshell increases the contact between volatile organic compounds and Ag NPs and enhances mass and energy transmission.

The $CaCO_3$ in the eggshell provides active carbonate radicals ($^{\bullet}CO_3^{-}$), which favor the degradation of organic compounds or microorganisms.[346] $CaCO_3$ provides the key chemical species (such as CO_3^{2-}, HCO_3^{-}, OH^{-}) in aqueous solution, which can react with $^{\bullet}OH^{-}$ to give rise to carbonate radicals, $^{\bullet}CO_3^{-}$. By employing eggshell as a $CaCO_3$ source and template, eggshell-derived $CaCO_3$/CuS and $CaCO_3$/PbS nanocomposites as photocatalytic systems have been reported (Fig. 30).[346,347] Using eggshell as a support allows the immobilization of CuS or PbS NPs onto a material with which to achieve the purification of wastewater (organic degradation and bacteria inactivation), thus preventing the agglomeration of the NPs. Moreover, $CaCO_3$ provides highly reactive radical species ($^{\bullet}CO_3^{-}$), which are essential in catalytic reactions and antibacterial applications. $CaCO_3$/CuS nanocomposites can be excited using NIR light. Their outstanding photocatalytic degradation of 4-nitrophenol (4-NP) and antibacterial activity against *E. coli*

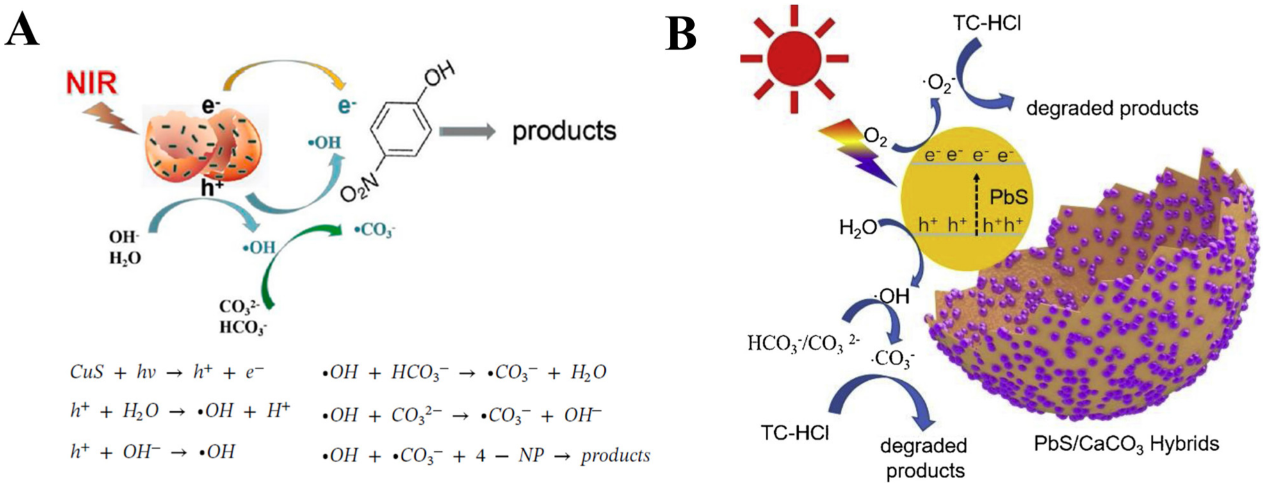

Fig. 30 Schematic diagram of $CaCO_3$-modified photocatalytically active semiconductor nanocomposites. (A) Schematic representation of 4-nitrophenol (4-NP) degradation using $CaCO_3$/CuS. Reprinted from ref. 347. Copyright (2020), with permission from Elsevier; (B) illustrative degradation of TC-HCl over a $CaCO_3$/PbS catalyst. Reprinted from ref. 346. Copyright (2020), with permission from Elsevier.

and *S. aureus* can be attributed to synergistic photocatalytic/PTT/PDT effects (Fig. 30A).[347] $CaCO_3$/PbS nanocomposites have been used for solar light-assisted photodegradation of tetracycline hydrochloride (TC-HCl) (Fig. 30B),[346] a process in which $^{\bullet}CO_3^-$ species make a remarkable contribution. $CaCO_3$-based photocatalysts thus hold promise for use in further studies on the design of cost-effective environmentally-benign systems for more sustainable development.

6.2 Energy materials

Phase change materials (PCMs) allow controllable and conditional energy storage and release.[348] Microencapsulated phase change materials (MEPCMs) with a rigid shell not only avoid the leakage associated with solid–liquid PCMs, but also enhance their heat transfer and thermal response.[349] $CaCO_3$ is rigid and dense, which gives it desirable thermal conductivity (2.167 $W m^{-1} K$) properties. The synthesis of $CaCO_3$ as an inorganic shell is cost-effective and can be achieved under mild synthetic conditions. Accordingly, $CaCO_3$-based MEPCMs do not exhibit the flammability, low thermal conductivity and mechanical strength, and poor thermochemical stability that are usually associated with organic shell materials, such as polystyrene,[350] phenolic resin,[351] and acrylic polymer.[352] Various paraffin PCMs, such as those based on n-alkanes, have been encapsulated with $CaCO_3$ or modified $CaCO_3$, including $CaCO_3$@*n*-eicosane,[348] $CaCO_3$@*n*-nonadecane,[353] $CaCO_3$@*n*-octadecane,[354] $CaCO_3$@paraffin,[355,356] $CaCO_3$@*n*-tetradecane,[357] GO-modified $CaCO_3$@paraffin,[358] and Ce^{3+}-doped $CaCO_3$@paraffin.[359] The thermal conductivity of $CaCO_3$-based MEPCMs increases with an increase in the content of the $CaCO_3$ shell.

On the surface of the PCM core, the $CaCO_3$ shell is usually formed *via* interfacial precipitation between water-soluble Ca^{2+} and CO_3^{2-}. Such a precipitation reaction is usually fast, and the self-assembly of $CaCO_3$ precursors at an oil–water interface is difficult to control, leading to the resultant $CaCO_3$-based MEPCMs exhibiting poor microstructures. A $CaCO_3$ shell resulting from the precipitation of Ca^{2+} and CO_3^{2-} onto the surface of oil droplets of PCMs *via* a self-assembly process has been investigated in various emulsion systems containing nonionic, cationic, anionic or complex surfactants.[348,349,354] For example, for $CaCO_3$@*n*-octadecane, $CaCO_3$ precipitated *via* self-assembly on the surfaces of *n*-octadecane micelles in an oil-in-water emulsion in the presence of Tween 80 and Span 80 mixed nonionic surfactants.[348] Such a $CaCO_3$ material assembled *via* complexation between Ca^{2+} and the hydroxyl groups of the mixed nonionic surfactants, followed by the precipitation of CO_3^{2-} at the interface of the micelles. Furthermore, a compact and thick highly thermally conductive $CaCO_3$ shell that was formed in a crystalline phase of vaterite can induce α-form crystallization *via* heterogeneous nucleation, thus enhancing the crystallinity of *n*-octadecane and improving its thermal conductivity. Moreover, it also enhanced the reliability, durability, and anti-osmosis properties of the $CaCO_3$@*n*-octadecane microcapsules. The stereochemical and geometric relationship between molecules of the anionic surfactant SDBS and $CaCO_3$ nuclei has been shown to favor the expression of specific crystalline facets, leading to different types of crystals being produced. Different concentrations of sodium dodecyl benzenesulfonic acid (SDBS) led to the synthesis of $CaCO_3$ shell with different morphologies.[348] At low concentrations of SDBS (<2.0 mmol L^{-1}), a calcite shell is formed on an *n*-eicosane core, whereas at high concentrations of SDBS (>5.0 mmol L^{-1}), a vaterite shell is formed. The $CaCO_3$@*n*-eicosane MEPCMs present rhombohedral and spherical morphologies, with the spherical $CaCO_3$@*n*-eicosane MEPCMs exhibited a higher encapsulation efficiency and energy-storage efficiency than their rhombohedral counterparts.

$CaCO_3$@*n*-Tetradecane MEPCMs have been prepared *via* a self-assembly technique using sodium dodecyl sulfate (SDS) and alkylphenol polyoxyethylene ether (OP-10) as mixed templates in an oil-in-water emulsion system.[357] In this process, OP-10 acts as an nonionic emulsifier to increase the stability of the emulsion system, thus decreasing the particle size of the $CaCO_3$@*n*-tetradecane MEPCMs. As a result of complexation between Ca^{2+} and SO_4^{2-} of the SDS, a large amount of concentrated Ca^{2+} can be self-assembled on the surface of the *n*-tetradecane micelles, with the formed $CaCO_3$ shell adopting a mixture of vaterite and calcite crystalline phases. By changing the core/shell mass ratio and the mass ratio of the SDS and OP-10 surfactants, a series of $CaCO_3$@*n*-tetradecane MEPCMs were obtained. The $CaCO_3$@*n*-tetradecane MEPCMs exhibit high thermal conductivity, thermal storage performance, good thermal stability, and show great potential for use in energy storage.

A $CaCO_3$ shell has also been used in the microencapsulation of a paraffin core to enhance thermal conductivity and to make it adjustable over a wide phase change temperature. For example, for $CaCO_3$@paraffin MEPCMs produced *via* a self-assembly pathway from a mixture of Tween 80 and Span 80 as a templating agent by changing the weight ratio of the paraffin core, the phase change temperature of the $CaCO_3$@paraffin MEPCMs can be adjusted over a temperature range of 25–50 °C.[355] The MEPCMs also exhibited significant enhancement in thermal conductivity, primarily due to the thermally conductive $CaCO_3$ shell. Jiang and co-workers fabricated a series of $CaCO_3$@paraffin materials with styrene–maleic anhydride (SMA) and different pH values *via* a self-assembly process.[356] The negatively charged carboxyl groups of the SMA molecules on the surface of paraffin droplets attracted positively charged Ca^{2+} ions to form calcite. The side chains of the SMA molecules were not conducive to forming vaterite crystals with a cationic coordination number of 12. In the paraffin emulsion, at high pH $CaCO_3$ crystals nucleated and grew rapidly, resulting in their irregular shape and the uneven particle size distribution of the MEPCMs. Low pH was not conducive to $CaCO_3$ deposition, thus the number of $CaCO_3$ particles deposited on the surface of paraffin emulsion was reduced. Moreover, $CaCO_3$@paraffin MEPCMs in a paraffin emulsion of pH 7 showed a high encapsulation efficiency of around 56.6%.

However, using $CaCO_3$ as a shell for MEPCMs, the encapsulation ratio was found to be low and did not prevent leaking of the core. Emir *et al.*[360] for the first time coated their thermal conductivity. The thermal storage capacities of $CaCO_3$@*n*-heptadecane and MEPCMs with Ag shells to produce multilayered Ag@$CaCO_3$@*n*-heptadecane MEPCMs to improve Ag@$CaCO_3$@*n*-heptadecane were found to be comparable to those of other paraffin-based materials microencapsulated with $CaCO_3$. Jiang and coworkers reported GO-modified paraffin MEPCMs with a $CaCO_3$ shell.[358] The paraffin was first emulsified with SMA to obtain negatively-charged paraffin droplets. The paraffin particles adsorbed Ca^{2+} on their surface, and the Ca^{2+} and the negatively-charged GO were then attracted to each other *via* an electrostatic interaction. The $CaCO_3$ shell formed after the addition of Na_2CO_3 was wrapped by and interconnected to the network of the GO. The GO-modified $CaCO_3$@-paraffin MEPCMs with perfect spherical core–shell structures were found to exhibit a high encapsulation ratio (73.19%) to improve the prevention of the core from leakage. In addition, the $CaCO_3$ shell was found to be compatible with GO, with GO sharing some of the external force and transfer, as well as consuming some of the external energy. Thus, the GO-modified $CaCO_3$@paraffin MEPCMs exhibited good thermal stability, thermal conductivity (0.857 W m^{-1} K), and mechanical properties.

$CaCO_3$-based MEPCMs can also be used as light-harvesting systems. However, the poor solar light-harvesting capability of the $CaCO_3$ shell limits the solar photothermal energy conversion and storage of these materials. A general route to achieving high photothermal energy conversion efficiency was developed in which energy-efficient photothermal materials were incorporated into $CaCO_3$-based MEPCMs. For example, $CaCO_3/Fe_3O_4$@*n*-docosane MEPCMs were successfully fabricated *via* a nonaqueous (O/W) emulsion-templated self-assembly technology using three types of surfactants: cationic cetrimonium bromide, anionic SDS, and nonionic PEO–PPO–PEO triblock copolymer (Fig. 31). The precipitation reaction rate of $CaCO_3$ can be adjusted and controlled in a nonaqueous (O/W) emulsion system prepared by formamide as the dispersion medium, thereby promoting the formation of a core-shell structure. Indeed, the use of a $CaCO_3/Fe_3O_4$ composite shell in $CaCO_3/Fe_3O_4$@n-docosane MEPCMs has been shown to enhance the efficiency of solar photothermal energy conversion and storage,[349] as the unique optical properties of the Fe_3O_4 NPs lead to an acceleration in the photothermal energy conversion and storage of the material. In this way, the photothermal conversion efficiency of the material was improved by 47.9%, which is much higher than that of $CaCO_3$@*n*-docosane MEPCMs.

In addition, $CaCO_3$ has been shown to act as a promising substrate for producing low-cost fluorescent materials that exhibit good luminescence properties.[361] In this arena, $CaCO_3$ has been used as a matrix to synthesize $CaCO_3$:Eu^{3+} phosphors[362] and Tb^{3+}/Eu^{3+} co-doped $CaCO_3$ phosphors.[363] $CaCO_3$ integrated with rare earth elements can be introduced into MEPCMs to enhance their thermal energy storage and photoluminescence. Ce^{3+}-Doped $CaCO_3$@paraffin MEPCMs have been designed *via* a self-assembly precipitation method to synthesize materials that exhibit thermal energy storage and

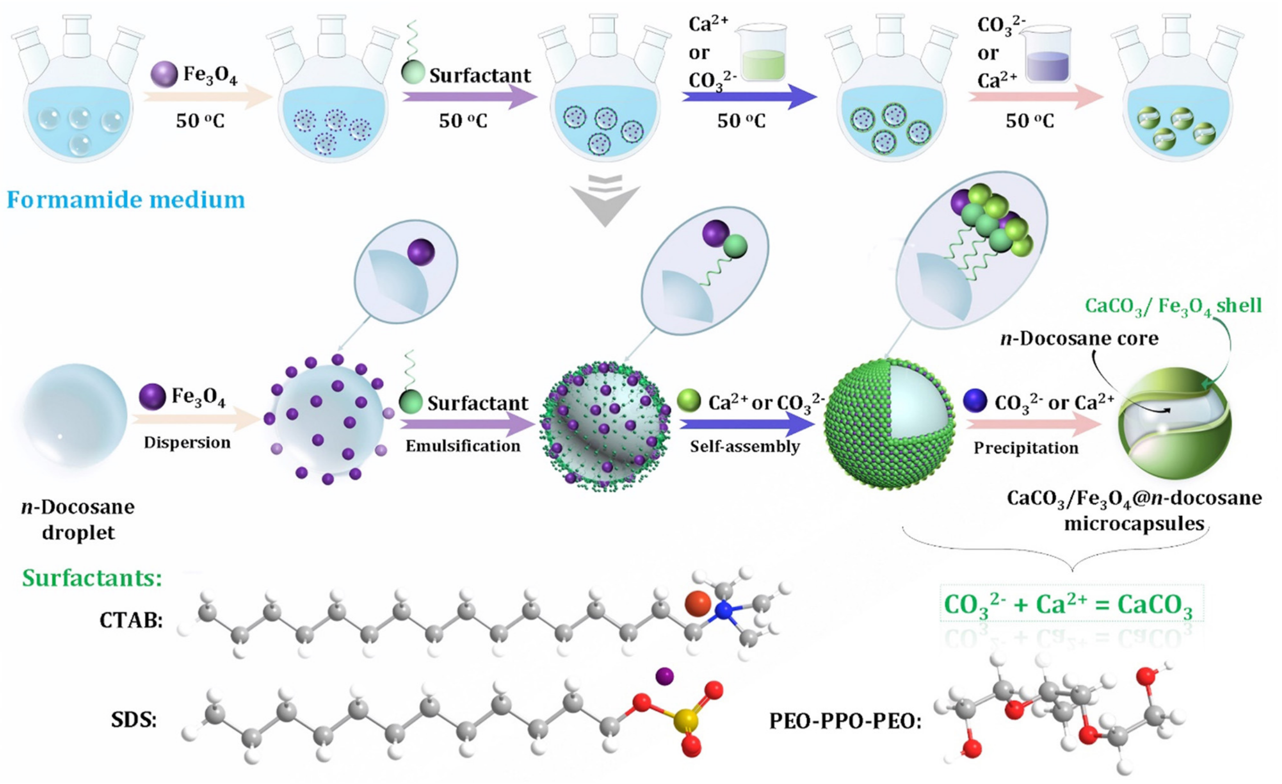

Fig. 31 Schematic diagram illustrating novel synthetic strategy for constructing $CaCO_3/Fe_3O_4$@*n*-docosane microencapsulated phase change materials. Reprinted from ref. 349. Copyright (2021), with permission from Elsevier.

photoluminescence properties.[359] Such dual-function Ce^{3+}-doped $CaCO_3$@paraffin MEPCMs might have potential applications in high-tech smart fiber or textiles systems, as well as in thermal and photosensitive sensors.

7. Amorphous calcium carbonate

ACC was first reported in the twentieth century by Addadi *et al.*[364,365] Since then, ACC has been discovered in many organisms, such as earthworms,[21] in the teeth of chitons,[366] nacre,[367] and in the exoskeletons of crustaceans.[368] ACC is a precursor of crystalline $CaCO_3$ in mollusks and sea urchins[188] and has been classified into proto-calcite, proto-aragonite and proto-vaterite types.[369,370] ACC can be further divided into transient precursor and hydrated forms. The stable hydrated form that contains at least one mole of water for every mole of $CaCO_3$ is usually the form adopted by synthetic ACC,[365] whereas the transient phase is essentially anhydrous and has thus far only been found in biominerals.[58,61]

Preparation conditions such as pH, temperature, solvent, and additives influence the composition, structure, hydration, and stability of ACC.[94] However, how organisms accurately control ACC formation under ambient conditions still remains unclear.[94,371] Recently, various inorganic ions such as Mg^{2+} and PO_4^{3-},[64,372] polymers,[67] and macromolecules[372] have been used to stabilize ACC in a short time frame. The preparation conditions and use of additives in the formation and stabilization of ACC have been shown to result in good control over the structure and morphology of the resultant ACC-based materials. Taking advantage of its flexible properties as an amorphous precursor,[373] or its mechanical properties in biomineral hybrid structures,[374,375] ACC can be used to design strong organic–inorganic hybrid materials. ACC NPs are active and high in energy, thus making them prone to hydrolysis in an intracellular environment.[25,30] Monodispersed ACC NPs have been reportedly used as templates to prepare a preloaded drug-delivery carrier and theranostic system.[39]

7.1 Preparation and stabilization of ACC

Several methods have thus far been reported to prepare ACC, such as the direct mixing of a Ca^{2+}–CO_3^{2-} aqueous reaction system with or without additives,[60,376] gas diffusion techniques,[369,377] the hydrolysis of carbonate,[378,379] and using a miniemulsion.[62] The preparation protocols, presence of co-precipitated ions such as CO_3^{2-} and Ca^{2+}, temperature, pH, solvent, and drying conditions are factors that have been shown to affect the preparation of ACC and impact upon its further transformation into crystalline $CaCO_3$.[380] Synthetic ACC contains water and its lifetime is related to its hydrate content as it transforms into a stable polymorph *via* a dissolution–(re)precipitation process accompanied by a loss of all of its water content.[61]

As the preparation of ACC usually involves the mixing of two aqueous solutions containing Ca^{2+} and CO_3^{2-}, traces of both salt from the counter ions and water are inevitably present in the final ACC material.[380] A fast-freezing technique can be employed to isolate ACC from mixed $CaCl_2$–Na_2CO_3. Dried pure ACC has been prepared by quenching aqueous saturated colloidal $CaCO_3$ suspension in liquid nitrogen (N_2) and then sublimating the solvent under vacuum.[381] Such treatments removed water from the reaction mixture quickly and prevented transformation of the ACC, resulting in an ACC with extended stability of up to 6 weeks when exposed to atmospheric conditions. Recently, it has been found that the instantaneous carbonation of $Ca(OH)_2$ aerosols with CO_2 followed by rapid drying of the ACC aerosols prevented the crystallization and resulted in the formation of a pure, stable, and dry ACC.[380] The ACC exhibited good stability against further crystallization for up to 3 weeks in air ($\sim$33% relative humidity). It has been demonstrated that mechanochemical treatment of ACC crystals leads to the structural collapse of ACC to smaller particles and the formation of defects in its structure.[382] The addition of Na_2CO_3 during milling was shown to lead to the incorporation of Na^+ cations into the ACC structure. As they were not easily incorporated into the lattice of the material, the Na^+ cations kinetically hindered the recrystallization of the resulting ACC. Moreover, the Ca in the ACC structure exhibited distorted octahedral coordination of six oxygen atoms, with an average coordination number of 5 reported for ball-milled ACC.

The drying process can affect the stability of ACC.[69] An ACC suspension obtained from two aqueous solutions containing Ca^{2+} and CO_3^{2-} was quenched in an organic solvent such as ethanol, isopropanol or acetone as part of its drying process.[69] The organic solvent was shown to isolate ACC from the water and slow its crystallization,[383] with monodisperse ACC NPs in the range of 100–200 nm produced from a water–ethanol system.[384] Furthermore, the formation and transformation of ACC in a mixed solvent of ethanol and water has been found to be affected by the pH of the solution. The solubility of ACC has been reported to decrease with an increase in the pH value of an aqueous solution from 5 to 12.5, and affect the formation and stability of ACC. A porous ACC, with a pore volume of $\sim$0.86 $cm^3\ g^{-1}$ and a pore-size distribution centered at around 8–9 nm has been developed from CaO and CO_2 using methanol as a solvent.[383] This ACC with a low water content (0.56 mol of H_2O per mol of $CaCO_3$) remains amorphous and retains its highly porous structure for over 3 weeks under semi-air-tight storage conditions.

The inclusion of additives, such as Mg^{2+},[64] PO_4^{3-},[67,372,385] SiO_2,[69] carboxyl species,[74,356] and polymers,[386] into ACC bulk have been well documented to improve the stability of ACC significantly. Mg^{2+} has been found in almost all biogenic ACC.[387] The incorporation of Mg^{2+} in ACC significantly slows its transformation into crystalline phases.[388] Such an effect of Mg^{2+} can be attributed to strong and well-hydrated Mg^{2+} cations that can delay the nucleation and growth of calcite and can either be incorporated within the calcite lattice to create a barrier to prevent the further growth of calcite nuclei.[389,390] Anions such as SiO_4^{4-}, PO_4^{3-}, and OH^- also influence the stability of ACC. The role of SiO_4^{4-} in stabilizing ACC has been evidenced by the presence of SiO_4^{4-} in cystoliths.[391] In these cystoliths, a high SiO_4^{4-} content in the ACC correlated with high thermal stability. Indeed, the negatively-charged tetrahedral SiO_4^{4-} in the ACC may conceivably destabilize calcite formation both by preventing regular structural packing and by perturbing the charge equilibrium.[391] Thus, the stabilization of ACC appears to be strictly related to the destabilization of calcite by "geometric frustration" of its crystal lattice. The PO_4^{3-} ion also has a tetrahedral structure and has been suggested to stabilize ACC in lobster carapace.[392] It has also been reported that PO_4^{3-} ions form a coating around ACC domains or enter into the ACC framework, thus preventing its transformation into calcite.[372] Moreover, PO_4^{3-} ions reduce particle nucleation and growth rate by binding to a crystal nucleus, thus effectively inhibiting the further crystallization of ACC.[65] The role of OH^- ions in the ACC stabilizer is negligible when they are added after the precipitation of ACC as OH^- ions are not able to alter the surface of the ACC NPs due to the ion association between Ca^{2+} and CO_3^{2-} being much stronger than that between Ca^{2+} and OH^-. However, when OH^- ions are incorporated in the bulk of ACC NPs rather than adsorbing on their surface, they have a remarkable influence on particle size.[371]

By inducing various carboxyl-based additives, such as citric acid (CA), adipic acid (AA), and hexanoic acid (HAA), into a suspension of ACC in methanol, followed by a fast drying process, the adsorption and incorporation of these additives can improve the stability of ACC.[68] In this process, the CA, AA and HA molecules adsorb onto the surface of the ACC NPs *via* electrostatic interactions (Fig. 32A, B and D), with the adsorbed CA and AA molecules forming hydrogen bonds *via* their carboxyl groups (Fig. 32A and B), while HA cannot form further interactions due to it only containing one carboxyl group (Fig. 32D). The concentrations of citrate in ACC extracted from exoskeletons and gastroliths has been found to be higher than those of high-molecular weight phosphoenolpyruvate and 3-phosphoglycerate.[393] Citrate strongly chelates Ca^{2+}, thus reducing the activity of free Ca^{2+} in solution. ACC synthesized in the presence of citrate is thus more stable than pure ACC. Besides this, the adsorption and incorporation of citrate in ACC increases both the lifetime and thermal stability ACC. An increase in the lifetime of the ACC corresponds to an increase in the adsorption and incorporation of citrate in ACC NPs that has the effect of slowing the dehydration and decomposition of ACC.[68]

According to the "non-classical" nucleation pathway, small $CaCO_3$ pre-nucleation clusters of 0.6–2 nm in size exist in a stearic acid monolayer as a template deposited on a supersaturated 9 mM $Ca(HCO_3)_2$ solution.[80,394] It is possible to stabilize such small $CaCO_3$ entities using specific ligands to produce monolayer-protected $CaCO_3$ clusters. For example, Sun and coworkers reported a solvothermal method by which to prepare monolayer-protected ACC clusters using 10,12-pentacosadiynoic acid (PCDA) as the ligand, ethanol as the solvent, and $NaHCO_3$ decomposition as a CO_2 source.[395] The ethanol both solubilizes the ligand and assists in the formation of kinetically stable ACC. Two main reactions successively occur, according to eqn (10) and (11). The PCDA chains are bound to the ACC core *via* chelation between their terminal –COOH groups and Ca^{2+} ions. The chemical formula of a monolayer protected ACC cluster with an average size of ~4.9 nm is suggested to be: $(CaCO_3)_7(H_2O)_4(PCDA)_3$.

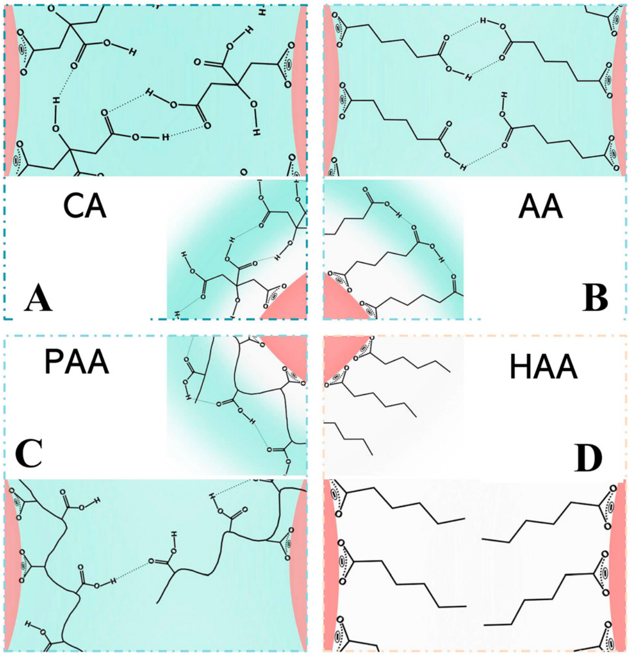

Fig. 32 Schematic diagram showing possible interactions in carboxyl-based additive-stabilized ACC NPs. (A) Citric acid (CA); (B) adipic acid (AA); (C) poly(acrylic acid) (PAA) and (D) hexanoic acid (HAA) (the red color indicates additives attached to the surface of ACC NPs *via* electrostatic interactions; the light green color indicates hydrogen bonds). Reprinted from ref. 69. Copyright (2020), with permission from Elsevier.

$$2NaHCO_3 \triangleq Na_2CO_3 + H_2O + CO_2 \uparrow \tag{10}$$

$$CaCl_2 + CO_2 + NH_4OH \rightarrow CaCO_3{\cdot}xH_2O(ACC) + NH_4Cl \tag{11}$$

The formation of ACC can also be influenced by many types of polymers and macromolecules, such as PDA,[396] PAA,[69] proteins[94] and dendrimers.[397] The inhibition in the transformation of ACC to a crystalline phase might involve the confining of the hydrated ACC within a hydrophobic polymer coating so that the water cannot escape. The small ACC particles are therefore isolated from the aqueous environment, making ACC stable.[365] Wang *et al.*[396] demonstrated that ACC NPs can be stabilized *via* a dopamine polymerization process at room temperature using an aqueous solution of $CaCl_2$, dimethyl carbonate, and dopamine. The Ca^{2+} ions were found to strongly interact with the flexible chains of the PDA, which were not only incorporated into but also coated the surface of the primary ACC NPs. The PDA network stabilizes the ACC, preventing the ACC NPs from growing bigger. Moreover, the PDA coating inhibits the dissolution of the ACC dissolution, thus slowing the subsequent Ostwald ripening. Moreover, such a coating creates isolated confinement spaces for ACC that prevent the contact and merger of ACC NPs, which further restricts the possible solid-phase transformation of ACC to a crystalline phase.

Similarly, PAA, a long-chain polymer additive, can stabilize ACC NPs by surrounding them to form a shell-like structure around the central ACC NP core (Fig. 32C).[68] Although the carboxyl groups on PAA could form hydrogen bondings with another ACC–PAA NP, the bulky PAA molecules possibly have relatively weak bonds (Fig. 32C). The long carbon chain of PAA prevents the further aggregation of the ACC–PAA NPs. When very small amounts of double hydrophilic block copolymers (DHBCs) comprising poly(ethylene oxide) (PEO) and PAA blocks are used as controlling agents, the adsorption layer of the block copolymer protects the liquid precursor of ACC from coalescence and/or coagulation.[386] Subsequently, spherical NPs of ACC with a narrow size distribution were obtained. The PAA not only interacts with Ca^{2+} but also induces the formation of $CaCO_3$-rich liquid phases, referred to as PILP phases.[398,399] Instead of being incorporated into the ACC bulk, PAA adsorbs to the ACC surface, which results in the ACC nanospheres being highly stable.[400] Biomacromolecules, polysaccharides, and proteins can also bind to the surface of ACC, isolating it from water and inhibiting its dissolution and subsequent crystallization to crystalline phases.[401,402] Such bio-macromolecules can also bind strongly to free Ca^{2+}, thus inhibiting or slowing its interaction with HCO_3^- and CO_3^{2-} during the formation and transformation of ACC.[21] Dendrimers are monodisperse macromolecules with a regular and highly branched 3D structure that can prolong the incubation time of ACC due to dendritic effects. By alternating the concentration of a carboxylic acid-terminated G0.5 poly(amidoamine) dendrimer that acts as a nucleation site at a fixed initial pH of 12 ± 0.2 at 15 °C with a $CaCl_2$–Na_2CO_3 liquid–liquid phase, spherical ACC NPs have been produced.[397] The surface of the dendrimer was proposed to act as a nucleation site, whereas its surface branch cells were found to compete with CO_3^{2-}. In the reaction, G0.5 acts as a stabilizer and inhibitor for ACC, preventing its crystallization to form calcite and vaterite, possibly resulting from the effects of the G0.5 dendrimer and its coordination of Ca^{2+} ions.

In the absence of biologically relevant additives such as divalent cations, negatively-charged polymers, and PO_4^{3-}, the binding between positively-charged Ca^{2+} ions and negatively-charged CO_3^{2-} ions resulted in the formation of $CaCO_3$ complex ions. The ACC phase separated from solution *via* a spinodal decomposition process wherein the overall concentration of the $CaCO_3$ complexes determined the average particle size of the ACC (Fig. 33A).[403] To tune the particle size of ACC and promote the phase separation process, the additives must be able to interact with Ca^{2+} or CO_3^{2-} ions simultaneously to induce the occurrence of long-range interactions between the $CaCO_3$ complex ions (Fig. 33B). The first way to this involves a cooperative ion-association process wherein the additives are attracted to either Ca^{2+} or CO_3^{2-} ions and provide additional effective interactions between the $CaCO_3$ complex ions. Such a cooperative ion-association process can be achieved by charged polymers with a long chain length, which attract either Ca^{2+} or CO_3^{2-} ions and their associated $CaCO_3$ complex ions along the chain (Fig. 33B). A similar result can be achieved using ions such as PO_4^{3-} that are able to form a dense structure with Ca^{2+} ions.[403]

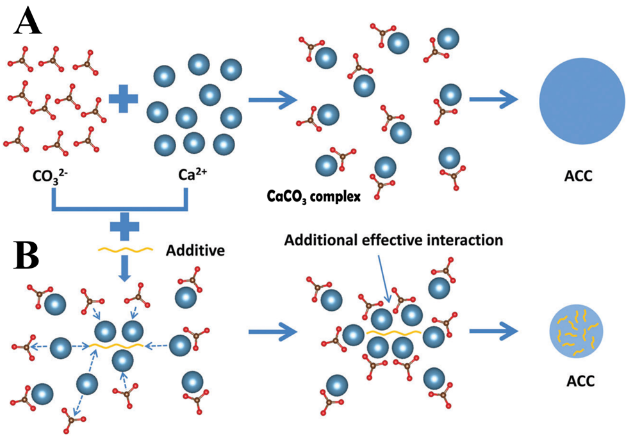

Fig. 33 Schematic diagram showing inherent mechanisms of ACC stabilization. (A) In the absence or presence of additives that are not able to influence the formation of ACC. (B) In the presence of charged polymers and PO_4^{3-} ions that are able to influence the formation of ACC. Adapted and reprinted from ref. 403. Copyright (2018), with permission from the Royal Society of Chemistry.

The lifespan of ACC is controlled by the type, structural arrangement, and quantities of the hydrous components (*i.e.*, mobile *vs.* rigid water, hydroxide ions) present in its structure.[404] The mobile water present within the structure of ACC is readily lost at temperatures of <150 °C, whereas rigid and less accessible water and hydroxide ions can only be removed at temperatures of >250 °C. Concomitant with the dehydration process, structural reorganization of the ACC has been observed from NMR analyses[405] and molecular modeling,[406] indicating that with increasing temperature a more ordered and stable atomic network forms. Besides the role that the structural arrangement of ACC plays in its lifespan, ACC that precipitates slowly in the range of pH 9–10 has been suggested to be more stable.[370]

7.2 Functionality and application of amorphous $CaCO_3$-based materials

Generally, ACC plays three major roles in biominerals. First, it acts as a transient, shapeable, amorphous precursor phase for crystalline $CaCO_3$.[407] Second, ACC is a rapidly accessible store of Ca for skeletal growth, as well as for the on demand production and repair of load-bearing structures.[408] For example, in the case of arthropods,[409] freshwater crayfish usually store protein-stabilized ACC in their gastroliths and use it to build their exoskeleton during molting.[94,393] Third, owing to its isotropic nature and ability to incorporate high concentrations of trace elements, ACC functions as a structural material. For example, crustaceans use ACC to stiffen exoskeletal cuticles. Owing to its adjustable properties as an amorphous precursor,[373] and the mechanical properties that it provides in biomineral hybrid structures,[374,375] ACC has been used as a precursor or final component for the design of new materials. In addition, because of their excellent transparent properties, strength, stiffness, and hardness, hydrogel films[57] with optical transparency and increased hardness can be created by incorporating ACC as an isotropic filler material in polymer phases.[386] Furthermore, ACC-based nanomaterials have shown great potential for use in biomedical applications as they are small in size and flexible toward further engineering.

7.2.1 ACC for forming films. The use of an ACC precursor is beneficial to the production of organic/inorganic hybrid films as it can be used to tune the optical properties, tensile strength, and hardness of the films.

By incorporation of 2–3 nm-sized ACC NPs into PAA, transparent, stable, and crack-free ACC/PAA thin films have been prepared.[60] Under ambient conditions, PAA and ACC are hybridized together (Fig. 34A), which results in the formation of ACC/PAA thin films consisting of ACC, PAA, and water. The complexation with a large amount of PAA and water molecules strongly inhibits the further crystallization of ACC in these ACC/PAA thin films. The ACC/PAA thin films possessed nanosegregated structures to form a new class of glassy functional materials.

Moreover, nanofibrillar cellulose-reinforced ACC/PAA free-standing composite films have been obtained by soaking a hydrogel sheet of carboxylated cellulose (CACell) in a colloidal ACC dispersion and drying it (Fig. 34B).[410] The CACell/ACC/PAA free-standing composite films were shown to mimic the organic/organic/inorganic nanocomposite structures of crustacean exoskeletons, in which the ACC component binds to chitin nanofibrils at the interface *via* acidic chitin-binding peptides (Fig. 34B-a). In such films, the reinforcing fibrils of the carboxylated cellulose capable of interacting with Ca^{2+} directly bind to ACC, which results in a strengthening of the interface of the fibrils and ACC (Fig. 34B-c). The stiff yet flexible and strong transparent CACell/ACC/PAA free-standing composite films exhibit elastic flexibility similar to those of natural crustacean exoskeletons (Fig. 34B-b).

Another example concerns the design and preparation of transparent and mechanically-tough CMC/CNF/ACC composite films *via* incorporating water-dispersible cellulose derivatives, namely carboxymethyl cellulose (CMC) and surface-decorated crystalline cellulose nanofibers (CNFs) into ACC/PAA composites (Fig. 34C).[411] The incorporation of ACC into cellulose-based materials was found to enhance the mechanical properties of the

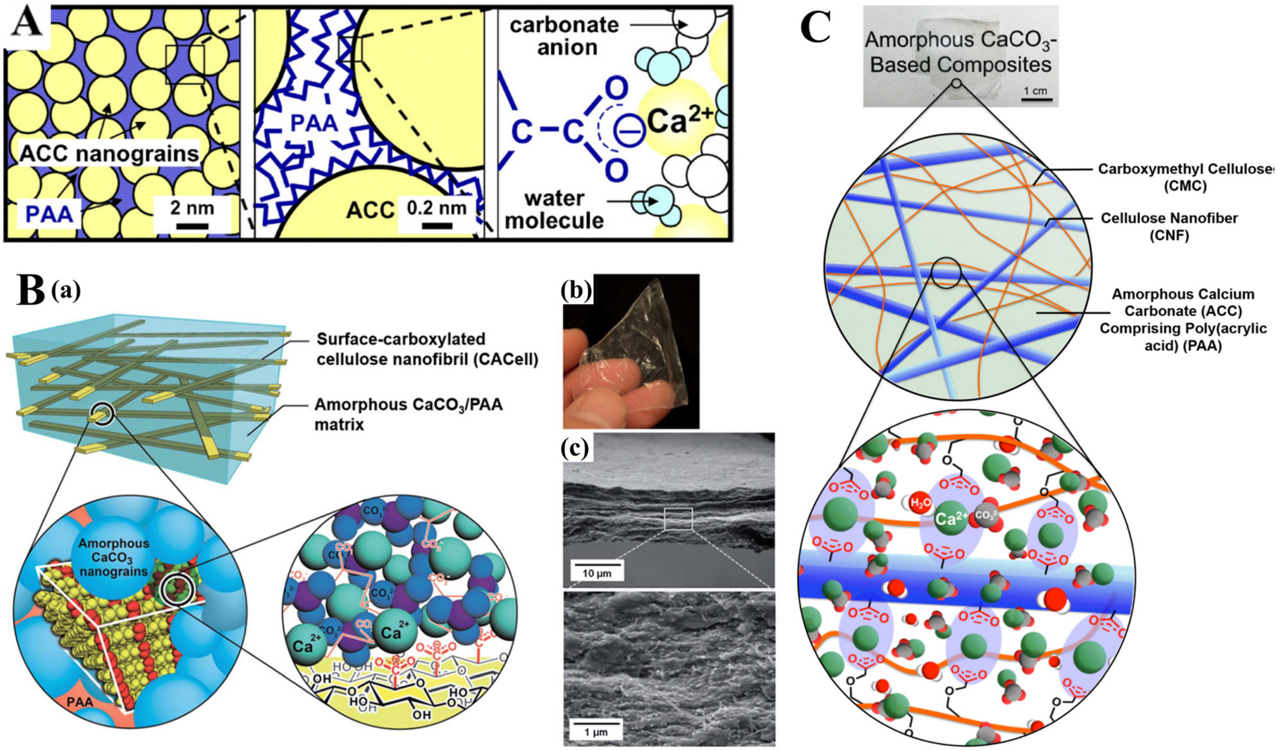

Fig. 34 Schematic diagram of novel ACC-based organic/inorganic hybrid films. (A) Nanosegregated amorphous composite consisting of ACC and PAA. Reprinted from ref. 60. Copyright (2008), with permission from John Wiley and Sons under the terms of the Creative Commons Attribution Non-Commercial (CC BY-NC 3.0) License. (B) Materials design and structures of CACell/ACC/PAA composites. (a) Schematic illustration of the design of CACell/ACC/PAA composites, showing the ACC/PAA matrix reinforced with the CACell network. Carboxyl groups on the nanofibril surfaces bound to calcium ions in the nanosegregated ACC/PAA matrix. (b) The prepared CACell/ACC/PAA composite film. (c) SEM images of a cross-section of the CACell/ACC/PAA composite. Reprinted from ref. 410. Copyright (2014), with permission from the Royal Society of Chemistry. (C) ACC-based (CMC/CNF/ACC) transparent films with biomimetic structures. Reprinted with permission from ref. 411. Copyright (2018) American Chemical Society. (CACell/ACC/PAA: carboxylated cellulose/amorphous calcium carbonate/poly (acrylic acid); CMC/CNF/ACC: carboxymethyl cellulose/cellulose nanofiber/amorphous calcium carbonate.)

resultant CMC/CNF/ACC composite films while maintaining their high transparency and environmental friendliness. Molecular-scale interactions between CMC and ACC *via* intermolecular forces between the carboxylate groups and Ca^{2+} were thought to enhance the stiffness and hardness of the flexible CMC/CNF/ACC composite films. Indeed, a CMC/CNF/ACC composite film with a ratio of 40, 40, and 20 wt% of CMC, CNFs, and ACC, respectively, showed a Young's modulus of 15.8 ± 0.93 GPa and a tensile strength of 268 ± 20 MPa. An appropriate amount of ACC interacting with the polymer fulfills the space between the organic matrices.

7.2.2 ACC for constructing supramolecular hydrogel. Incorporating ACC NPs into a hydrogel matrix leads to the formation of ACC-based nanocomposite hydrogels with good mechanical performance or a novel structure.[412,413] For example, by simply mixing $CaCl_2$, Na_2CO_3, and PAA (M_w = 100 000 g mol^{-1}) in water, an ACC/PAA supramolecular hydrogel can be obtained.[70] The resultant ACC/PAA hydrogel is a complex of ACC NPs physically cross-linked by PAA chains *via* electrostatic interactions between COO^- and Ca^{2+}. The hydrogel is a dough-like material, soft but tough, and can be shaped into films, cylinders, and stars. It can also be stretched into very long fibers with plastic deformation without any elastic recovery. Moreover, when the hydrogel is broken in half and ressembled, it can rapidly self-heal within 5 s. A SEM image of the freeze-dried ACC/PAA hydrogel shows that it has a porous internal structure. In addition, very small ACC NPs of 1.5–3 nm can be identified from the TEM image of the dry gel. Considering the increasing environmental concerns arising from the petroleum-based production of conventional plastics, the ACC/PAA hydrogel may be used as a new environmentally-friendly and sustainable plastic material or "mineral plastic."

7.2.3 ACC for drug nanocarriers. The use of crystalline $CaCO_3$ as a drug delivery system is impeded by its microscale size and slow degradation in the biological environment due to its high crystallinity, which severely undermines drug release efficiency.[274] In contrast, ACC NPs have a higher surface energy compared to crystalline $CaCO_3$ and are prone to hydrolysis in the intracellular environment. However, the high instability of ACC (rapid crystallization), which leads to it being difficult to store, has been recognized as a major obstacle in its further application in drug delivery.[414] Therefore, overcoming the high instability of ACC is the key to unlocking its applications in biological systems.[65] To overcome these limitations, Zhao *et al.*[39] developed an ACC–DOX@silica nanoreactor (Fig. 35), which was obtained *via* the self-assembly of an ACC–DOX core surface coated with a silica shell (Fig. 35A) wherein DOX chelates with Ca^{2+} to form a Ca–DOX complex (Fig. 35A). In this core–shell structured nanoreactor, acidic stimuli affect the silica shell, which triggers inner reactions within the ACC–DOX core. The DOX molecule dissociates from the core and then adheres to the negatively-charged SiO_2 shell *via* a pH-dependent electrostatic attraction instead of being directly released. Therefore, such nanoreactor maintains low drug leakage in physiological and lysosomal/endosomal environments, as well as selectively releasing the drug in the weakly acidic TME (pH 6.5) (Fig. 35B–E), leading to an efficient tumor-cell killing effect in a sustained manner.

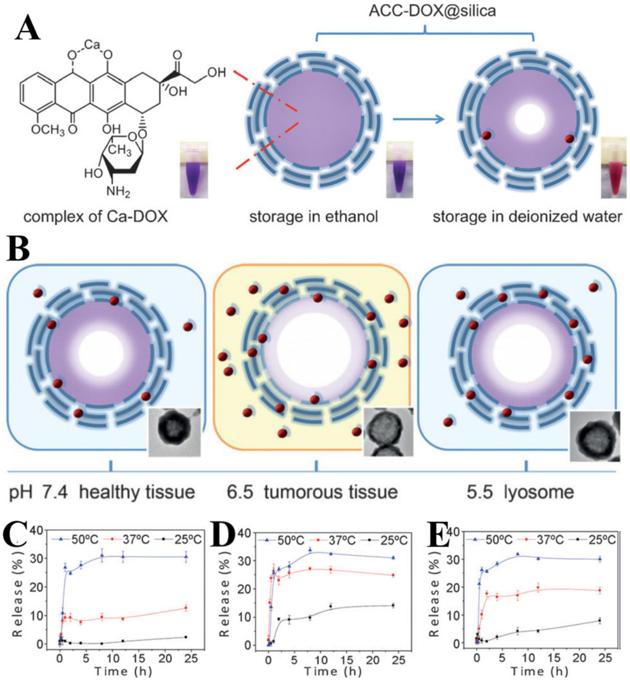

Fig. 35 Schematic diagram of ACC–DOX@silica nanoreactor for pH-responsive delivery in cancer therapy. (A) The ACC–DOX@silica nanoreactor and its stability in ethanol and water. The inset images (from left to right) show the suspensions of ACC–DOX in ethanol, ACC–DOX@silica in ethanol, and ACC–DOX@silica in water. (B) The release behavior of ACC–DOX NPs under various pH conditions. Cumulative release of DOX from ACC–DOX@silica suspensions in various aqueous buffers at (C) pH 7.4, (D) pH 6.5, and (E) pH 5.5 at different temperatures of 25, 37, and 50 °C. (A), (C), (D), (E) Reprinted from ref. 415. Copyright (2015), with permission from John Wiley and Sons under the terms of the Creative Commons Attribution Non-Commercial (CC BY-NC 3.0) License. (B) Reprinted from ref. 95. Copyright (2018), with permission from MDPI under the terms of the Creative Commons Attribution License.

However, the thick silica shell may induce adverse effects such as an increase in nanocarrier size, inadequate drug release, and hard degradation *in vivo*.[416] Therefore, a more appropriate biocompatible and biodegradable stabilizer is desirable for stabilizing the ACC NPs and achieving sustained drug release. When ACC–DOX was surface modified with phospholipid (PL) (containing an appropriate amount of DSPE–PEG and/or DSPE–PEG–FA), the PL substance acted as a biocompatible and water-resistant coating to improve the half-life period of the modified PL/ACC–DOX NPs and maintain the water responsiveness of the ACC (Fig. 36A).[417] The PL also acts as a diffusion barrier to prevent potential drug leakage. Using a facile solvent-diffusion method, mitoxantrone (MIT)-preloaded PL–ACC (PL/ACC–MIT) hybrid NPs containing the shielding polymer PEG and targeting moiety FA were prepared.[72] The PL/ACC–MIT NPs were shown to have satisfactory stability toward various aqueous environments with minimal drug leakage and good targeting capability. Xu *et al.*[272] developed tunable pH-responsive DOX@ACC/PAA NPs (pH 7.4–5.6) by encapsulating DOX in PAA-stabilized ACC NPs.

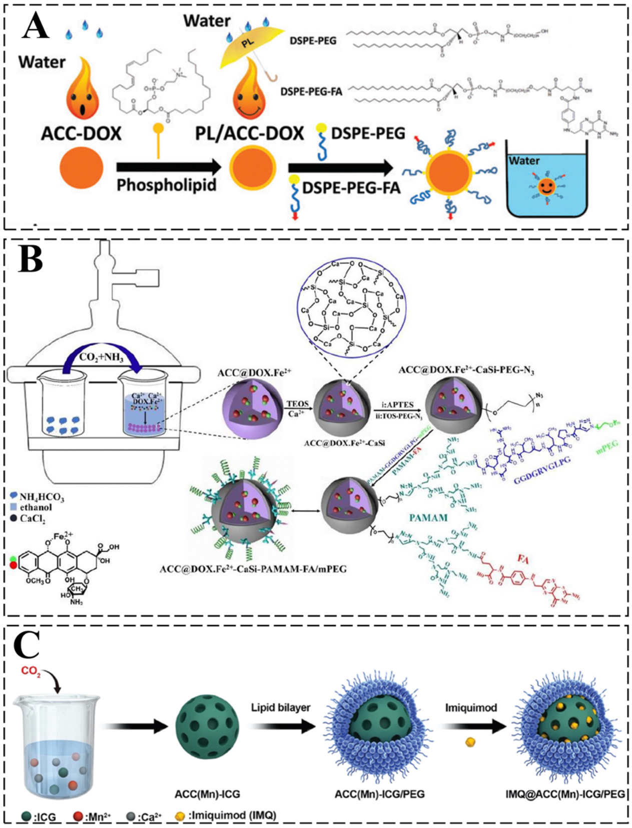

Fig. 36 Schematic diagram of ACC NPs for pH-responsive drug delivery. (A) PL/ACC–DOX hybrid NPs for controllable burst drug release and enhanced tumor penetration. Reprinted from ref. 417. Copyright (2018), with permission from the Royal Society of Chemistry. (B) TME-activatable Fe–DOX preloaded ACC nanoformulation triggers ferroptosis in target tumor cells. Reprinted with permission from ref. 73. Copyright (2020), with permission from AAAS under the terms of the Creative Commons Attribution NonCommercial License 4.0 (CC-BY-NC). (C) IMQ@ACC(Mn)–ICG/PEG NPs as immunoadjuvants for multimodal imaging and enhanced photoimmunotherapy. Reprinted from ref. 420. Copyright (2020), with permission from the Royal Society of Chemistry. ACC: amorphous $CaCO_3$; ICG: indocyanine green; IMQ: imiquimod; PEG: polyethylene glycol; PL: phospholipid.

The chelation between DOX and $Ca^{2+}$and the hydrogen bonding between DOX and PAA, enabled efficient DOX encapsulation into the ACC/PAA NPs. The resultant monodisperse DOX@ACC/PAA NPs were found to be small in size (62 ± 10 nm), have good serum stability, and high drug encapsulation efficiency ($>80\%$) and loading capacity ($>9\%$). Importantly, the release of DOX from the NPs could be further modulated to higher pH response ranges (pH 7.7–6.0) *via* the doping of specific amounts of Sr^{3+} or Mg^{2+} into the DOX@ACC/PAA NPs. The resultant Sr^{3+}- or Mg^{2+}-doped DOX@ACC/PAA NPs could be potentially utilized for specific domains of cells or tissues with a less acidic microenvironment.

To address inadequate drug release and poor drug penetration in cancer therapy, if the high instability of ACC could be harnessed while realizing drug burst release within specific targeted sites, it would be a beneficial material to use to improve drug release within cells in a water-responsive manner. To this aim, Wang *et al.*[418] locked ACC within a superhydrophobic oleic acid (OA) shell and then modified the shell with a PEG corona to form PEG/OA–ACC. The PEG/OA–ACC material exhibits greatly enhanced stability of ACC under neutral conditions and the high aqueous instability of ACC was demonstrated to realize drug burst release in an acidic environment within cancer cells, which resulted in a comparable anticancer effect being achieved to that of free drugs. Similarly, lipase-triggered water-responsive ''Pandora's box'' (MS/ACC–DOX) NPs have been constructed by coating DOX-preloaded ACC–DOX NPs with monostearin (MS).[419] During its application, the high aqueous instability of ACC led to a burst release of the encapsulated DOX, inducing apoptosis and cytotoxicity to kill tumor cells. The released MS/ACC–DOX NPs from the dead or dying cells continued to water-responsively release DOX after being unpacked in a ''Pandora's box'' manner, inducing apoptosis on untreated neighboring cells (neighboring effect). The severe neighboring effect of MS/ACC–DOX NPs with increased cytotoxicity and continuously released free DOX molecules from the exterior to the interior of the solid tumor contributed to enhance DOX penetration into deep tumor matrix, resulting in elevating antitumor efficacy.

ACC NPs can be simultaneously loaded with multiple molecules to achieve multimodal cancer treatment. The ACC substrate can synergize with the therapeutic interaction between DOX and Fe^{2+} to form a TME-activatable Fe–DOX preloaded ACC nanoformulation with complementary ferroptosis/apoptosis-inducing capability. For example, a tumor-targeted ACC-based nanoplatform (ACC@DOX.Fe^{2+}–CaSi–PAMAM–FA/mPEG) was developed for ferroptosis therapy (Fig. 36B).[73] ACC@DOX–Fe^{2+} cores were first established *via* a gas diffusion method, followed by coating with a thin layer of CaSi (Fig. 36B). The ACC@DOX·Fe^{2+}–CaSi material was then simultaneously conjugated with folate-modified and PEGylated polyamidoamine (PAMAM) dendrimers, which offered a functional balance between circulation longevity and tumor-specific uptake. The DOX and Fe^{2+} were released intracellularly in a self-regulated manner *via* the acidity-triggered degradation of ACC, where DOX amplifies the ferroptosis effects of Fe^{2+} by producing H_2O_2. In addition, the ACC NPs have the ability to clear H^+ from the tumor tissue, inhibiting the polarization of tumor-associated macrophages to M2-like phenotypes. Mn^{2+}-Doped ACC NPs have been designed as a multicarrier to co-deliver photosensitive ICG and the toll-like-receptor-7 agonist imiquimod (IMQ) to achieve pH-triggered controllable drug delivery and tumor-specific enhanced photoimmunotherapy guided by multimodal imaging (Fig. 36C).[420] In this study, ICG was chelated with Ca^{2+} ions and was finally embedded in ACC in the form of a Ca–ICG complex. ACC(Mn)–ICG NPs were modified with a self-assembled lipid bilayer, followed by loading of IMQ to form IMQ@ACC(Mn)–ICG/PEG NPs (Fig. 36C). ACC NPs scavenged the H^+ of the tumor to reverse the immunosuppression of the tumor environment, effectively inhibiting tumor metastases. The IMQ@ACC(Mn)–ICG/PEG NPs heavily accumulated in tumor tissues and significantly ablated the tumors after fluorescence/MRI-guided laser irradiation. These bioresponsive theranostic NPs based-on biodegradable ACC could thus become an effective tool for use in cancer theranostics.

8. Concluding remarks

The past decade has witnessed tremendous advances in experimental strategies for controlling the preparation and modification of $CaCO_3$ MNPs, as well as the stabilization of synthetic ACC. Focus has been on the investigation of the nucleation and growth mechanisms of specific $CaCO_3$ polymorphs and the development of new methods by which to engineer $CaCO_3$ into multifunctional nanostructured materials. Thus, various $CaCO_3$-based materials have been developed and used for bone repair, wound healing, bioimaging, theranostics, environmental maintenance, and clean energy production and storage. Despite impressive achievements, there are still open challenges in terms of developing new methodologies for controlled synthesis, surface modification, and engineering of $CaCO_3$ into nanostructured materials and their applications.

Previous studies have indicated that although $CaCO_3$ precipitation is not a simple process, the insights discussed above might play a role in predicting a particular form or shape of $CaCO_3$ precipitation to some extent. The control of the crystal size and morphology of $CaCO_3$ MNPs particles can be achieved even by slight variations in the temperature, pH, mixing of reactants, or by the addition of different organic or inorganic additives to reactions. Although it remains of major interest, special attention has been paid to polymorphism, which can be regulated *via* subtle interplay between thermodynamics and kinetic factors.[104] For example, high supersaturation causes the initial formation of small particles and metastable phases, such as ACC or vaterite, which then transforms *via* solution-mediated process into very stable calcite. However, if organic additives, including surfactants, macromolecules, and polyelectrolytes, or certain inorganic additives are present, the unstable phases can be stabilized more or less. In such systems, the shape of $CaCO_3$ particles could be significantly affected by the concentration and nature of additives, and particular crystal planes can be expressed as a consequence of specific interactions between additive and growing crystal surfaces. Formation of spherical or rounded particles could be a result of inhibited or spherulitic growth in the presence of additives and the aggregation of smaller primary particles. Under the conditions of high initial supersaturation, the interplay of kinetics of nucleation, crystal growth, dissolution, and ageing appear to be critical for the physical and chemical characteristics of the final $CaCO_3$ precipitate. In contrast, a lower initial supersaturation typically causes the direct formation of thermodynamically stable polymorph calcite, either by heterogeneous or homogeneous nucleation. The deviation from stable rhombohedral morphology in the absence of additives might be a consequence of a nonstoichiometric distribution of constituent ions (Ca^{2+} and CO_3^{2-}) or H^+ and OH^- and the dominant adsorption of ions that are in excess on specific crystal planes. The remarkable influence of additional inorganic ions on the $CaCO_3$ precipitation and its products has captured particular attention recently, and yet the understanding of it is still in infancy. It is now known that low temperatures and the presence of orthophosphate promote the formation of hydrated forms, such as ikaite (or monohydrocalcite). Higher temperatures and the presence of Mg^{2+}, promote the formation of aragonite and other metastable phases. Unfortunately, although the CO_2 carbonation process conducted using an economically and environmentally-friendly process provides $CaCO_3$ MNPs with a wide particle size distribution range, shapes and polymorphs, it cannot be well controlled. In contrast, $CaCO_3$ particles of various sizes (nanometer to micrometer), polymorph composition, and morphologies (needle-like, rod-like, whisker-like, spheres, porous spheres, hollow spheres, *etc.*) can be synthesized using different reactants, additives, and even different experimental set ups, for example Ca^{2+}–H_2O/organic solvents/additives/CO_3^{2-} precipitation systems, W/O reverse emulsion, or biomimetic $CaCO_3$ formation. However, the production of $CaCO_3$ in such systems is still hard to achieve on a large scale.

An in-depth understanding of the basic principles of $CaCO_3$ nucleation and growth is essential for achieving tunable synthesis. Currently, the predominant nucleation and growth mechanisms are still questionable. The classical nucleation mechanism, which assumes the formation of critically sized nuclei of a new solid phase, is challenged by the non-classical concept. On the contrary, the non-classical mechanism assumes the initial formation of thermodynamically-stable prenucleation clusters or the formation of a dense liquid precursor phase *via* liquid–liquid phase separation. Further studies are thus required to address the following issues. How can the pathway of a certain specific crystallization process be controlled? Which crystallization process is dominant under a specific set of conditions? In addition, the current research on non-classical $CaCO_3$ crystallization is mainly based on the assumption and the conditions of a homogeneous nucleation, so further questions are: what is the exact crystallization mechanism and growth process under heterogeneous nucleation? What is the exact mode of the molecular interactions between the substrates and precursors during the nucleation?

So far, the surface modification of $CaCO_3$ MNPs has been predominantly accomplished either *via* surface adsorption and coating with coupling agents, organic acids, or anionic and cationic surfactants, or using solid inorganic SiO_2. Such modification tunes the surface polarity, hydro- and oleophilicity, stability, and reactivity of the $CaCO_3$ particles. The surface-modified $CaCO_3$ can then be further engineered into functional hierarchical nanostructured materials, which show great potential in numerous fields, ranging from biomaterials and biomedicine to environmental remediation and energy storage. A characteristic of $CaCO_3$ NPs is their sensitivity to pH, which allows them to release the cargo conditionally at specific sites. Nevertheless, there is still much need for future work to enable better tune the pH-sensitivity of the $CaCO_3$ NPs. In this context, as the subtle changes in a TME are not only down to pH, other physiological factors, such as low-oxygen levels, abnormal cysteine metabolism or concentrations of relevant ions, are worth considering so as to match these factors to the features of $CaCO_3$ materials. At present, most of the biomedical applications of $CaCO_3$ have only reached the pre-clinical stage. Biomimetically ordered arrangements of $CaCO_3$ nanocrystals, as a prototype of advanced organic–inorganic composites, have led to nacre-like structures being produced, but their density and uniformity are far from those of the nacre in seashells or mollusks. It is thus expected that the aforementioned technologies of synthetic $CaCO_3$ will be extended to utilize biogenic $CaCO_3$ resources (*e.g.*, eggshell or mollusk shells), which are available in large quantities in the agriculture and food industries, with the aim of achieving good recyclability, sustainability, and a low-carbon footprint.

ACC also has great potential for use as a smart and pH-responsive hydrogel or drug carrier. Over the last decade, much effort has been made to develop an effective way of stabilizing ACC, however, the long-term stability of ACC has yet to be accomplished. Both the intrinsic properties of ACC and the adjacent environmental conditions (temperature, pressure, humidity, *etc.*) have been found to be critical in determining its stability. The correlation of the synthesis conditions with the ACC stability and the interactions between the additives and the resultant ACC still remain unclear. An unanswered question that remains is related to the inhibition of dehydration and transformation of ACC into crystalline $CaCO_3$. To tackle the complexity of ACC systems, it is necessary to further investigate the mechanisms of the biomineralization processes of specific organisms that are responsible for accurately controlling the formation and stabilization of ACC. Such detailed studies will be helpful toward the design and subsequent production of functional biomimetic $CaCO_3$ nanostructures and/or composites in an environmentally-friendly and even sustainable manner.

Author contributions

Yu-Qin Niu: investigation, writing original draft, writing-review and editing; Jia-Hui Liu: reviewing, revision and editing; Cyril Aymonier: revision and editing; Simona Fermani: revision and editing; Damir Kralj: reviewing, revision and editing; Giuseppe Falini: reviewing, revision and editing; Chun-Hui Zhou: conceiving the project, conceptualization, discussion, supervision, writing and reviewing, revision and editing.

Conflicts of interest

There are no conflicts to declare.

Acknowledgements

The authors wish to acknowledge the financial support from the National Natural Science Foundation of China (22072136). G. F. and S. F. thank the Bluebio ERANET for funding (project CASEAWA; grant number 161B0949).

Notes and references

1 J. W. Morse, R. S. Arvidson and A. Luttge, *Chem. Rev.*, 2007, **107**, 342–381.
2 W. Shi, S. Zhang, Y. Wang, J. Wang, B. Li, X. Liu, X. Liu, Q. Wang and J. Cheng, *ChemistrySelect*, 2018, **3**, 6050–6055.
3 H. Ehrlich, M. Motylenko, P. V. Sundareshwar, A. Ereskovsky, I. Zgłobicka, T. Noga, T. Płociński, M. V. Tsurkan, E. Wyroba, S. Suski, H. Bilski, M. Wysokowski, H. Stöcker, A. Makarova, D. Vyalikh, J. Walter, S. L. Molodtsov, V. V. Bazhenov, I. Petrenko, E. Langer, A. Richter, E. Niederschlag, M. Pisarek, A. Springer, M. Gelinsky, D. Rafaja, A. Witkowski, D. C. Meyer, T. Jesionowski and K. J. Kurzydłowski, *Adv. Funct. Mater.*, 2016, **26**, 2503–2510.
4 H. Ehrlich, E. Brunner, P. Simon, V. V. Bazhenov, J. P. Botting, K. R. Tabachnick, A. Springer, K. Kummer, D. V. Vyalikh, S. L. Molodtsov, D. Kurek, M. Kammer, R. Born, A. Kovalev, S. N. Gorb, P. G. Koutsoukos and A. Summers, *Adv. Funct. Mater.*, 2011, **21**, 3473–3481.
5 A. Kertmen, I. Petrenko, C. Schimpf, D. Rafaja, O. Petrova, V. Sivkov, S. Nekipelov, A. Fursov, A. L. Stelling, K. Heimler, A. Rogoll, C. Vogt and H. Ehrlich, *Int. J. Mol. Sci.*, 2021, **22**, 12588.
6 Y. Politi, T. Arad, E. Klein, S. Weiner and L. Addadi, *Science*, 2004, **306**, 1161–1164.
7 J. N. Murphy, C. M. Schneider, K. Hawboldt and F. M. Kerton, *Matter*, 2020, **3**, 2029–2041.
8 T. Yang, Z. Jia, H. Chen, Z. Deng, W. Liu, L. Chen and L. Li, *Proc. Natl. Acad. Sci. U. S. A.*, 2020, **117**, 23450–23459.
9 J. Aizenberg, A. Tkachenko, S. Weiner, L. Addadi and G. Hendler, *Nature*, 2001, **412**, 819–822.
10 P. Simon, W. Pompe, D. Gruner, E. Sturm, K. Ostermann, S. Matys, M. Vogel and G. Rodel, *ACS Biomater. Sci. Eng.*, 2022, **8**, 526–539.
11 H. Ehrlich, E. Bailey, M. Wysokowski and T. Jesionowski, *Biomimetics*, 2021, **6**, 46.
12 M. Wysokowski, P. Zaslansky and H. Ehrlich, *ACS Biomater. Sci. Eng.*, 2020, **6**, 5357–5367.
13 M. Wysokowski, I. Petrenko, R. Galli, C. Schimpf, D. Rafaja, J. Hubalkova, C. G. Aneziris, S. Dyshlovoy, G. von Amsberg, H. Meissner, Y. M. Yakovlev, K. R. Tabachnick, A. L. Stelling and H. Ehrlich, *Appl. Phys. A*, 2020, **126**, 727.
14 J. Aufort and R. Demichelis, *Cryst. Growth Des.*, 2020, **20**, 8028–8038.
15 Y.-B. Hu, D. A. Wolf-Gladrow, G. S. Dieckmann, C. Völker and G. Nehrke, *Mar. Chem.*, 2014, **162**, 10–18.
16 Z. Y. Zou, W. J. E. M. Habraken, G. Matveeva, A. C. S. Jensen, L. Bertinetti, M. A. Hood, C. Y. Sun, P. U. P. A. Gilbert, I. Polishchuk, B. Pokroy, J. Mahanid, Y. Politi, S. Weiner, P. Werner, S. Bette, R. Dinnebier,

U. Kolb, E. Zolotoyabko and P. Fratzl, *Science*, 2019, **363**, 396–400.

17 T. Mass, A. J. Giuffre, C. Y. Sun, C. A. Stifler, M. J. Frazier, M. Neder, N. Tamura, C. V. Stan, M. A. Marcus and P. Gilbert, *Proc. Natl. Acad. Sci. U. S. A.*, 2017, **114**, E7670–E7678.

18 A. Akiva-Tal, S. Kababya, Y. S. Balazs, L. Glazer, A. Berman, A. Sagi and A. Schmidt, *Proc. Natl. Acad. Sci. U. S. A.*, 2011, **108**, 14763–14768.

19 Y. U. Gong, C. E. Killian, I. C. Olson, N. P. Appathurai, A. L. Amasino, M. C. Martin, L. J. Holt, F. H. Wilt and P. U. Gilbert, *Proc. Natl. Acad. Sci. U. S. A.*, 2012, **109**, 6088–6093.

20 R. T. DeVol, C. Y. Sun, M. A. Marcus, S. N. Coppersmith, S. C. Myneni and P. U. Gilbert, *J. Am. Chem. Soc.*, 2015, **137**, 13325–13333.

21 M. E. Hodson, L. G. Benning, B. Demarchi, K. E. Penkman, J. D. Rodriguez-Blanco, P. F. Schofield and E. A. Versteegh, *Geochem. Trans.*, 2015, **16**, 4.

22 F. C. Meldrum, *Int. Mater. Rev.*, 2003, **48**, 187–224.

23 Y. Boyjoo, V. K. Pareek and J. Liu, *J. Mater. Chem. A*, 2014, **2**, 14270–14288.

24 T. Yang, J. Fu, L. Ma, H. Du, X. Yue, B. Zhao and C. Wang, *Mater. Sci. Eng., C*, 2020, **114**, 111019.

25 H. Bahrom, A. A. Goncharenko, L. I. Fatkhutdinova, O. O. Peltek, A. R. Muslimov, O. Y. Koval, I. E. Eliseev, A. Manchev, D. Gorin, I. I. Shishkin, R. E. Noskov, A. S. Timin, P. Ginzburg and M. V. Zyuzin, *ACS Sustainable Chem. Eng.*, 2019, **7**, 19142–19156.

26 T. M. Stawski, T. Roncal-Herrero, A. Fernandez-Martinez, A. Matamoros-Veloza, R. Kroger and L. G. Benning, *Phys. Chem. Chem. Phys.*, 2018, **20**, 13825–13835.

27 Y. Yu, J. Zhang, H. Wang and Z. Xin, *Polymers*, 2020, **12**, 2668.

28 N. A. J. M. Sommerdijk and G. de With, *Chem. Rev.*, 2008, **108**, 4499–4550.

29 F. C. Meldrum and H. Colfen, *Chem. Rev.*, 2008, **108**, 4332–4432.

30 L. Štajner, J. Kontrec, B. Njegić Džakula, N. Maltar-Strmečki, M. Plodinec, D. M. Lyons and D. Kralj, *J. Cryst. Growth*, 2018, **486**, 71–81.

31 J. A. Lopez-Berganza and R. M. Espinosa-Marzal, *Cryst. Growth Des.*, 2016, **16**, 6186–6198.

32 Y.-Y. Kim, J. D. Carloni, B. Demarchi, D. Sparks, D. G. Reid, M. E. Kunitake, C. C. Tang, M. J. Duer, C. L. Freeman, B. Pokroy, K. Penkman, J. H. Harding, L. A. Estroff, S. P. Baker and F. C. Meldrum, *Nat. Mater.*, 2016, **15**, 903–910.

33 C. Han, Y. Hu, K. Wang and G. Luo, *Powder Technol.*, 2019, **356**, 414–422.

34 Z. Liu, H. Onay, F. Guo, J. Chen, L. Poltorak, P. Hedayati and E. J. R. Sudhölter, *Energy Fuels*, 2021, **35**, 1358–1370.

35 D. Volodkin, *Adv. Colloid Interface Sci.*, 2014, **207**, 306–324.

36 N. T. Enyedi, J. Makk, L. Kotai, B. Berenyi, S. Klebert, Z. Sebestyen, Z. Molnar, A. K. Borsodi, S. Leel-Ossy, A. Demeny and P. Nemeth, *Sci. Rep.*, 2020, **10**, 8696.

37 A. Y. Cai, Y. J. Zhu and C. Qi, *Adv. Mater. Interfaces*, 2020, **7**, 2000819.

38 V. Vergaro, I. Pisano, R. Grisorio, F. Baldassarre, R. Mallamaci, A. Santoro, G. P. Suranna, P. Papadia, F. P. Fanizzi and G. Ciccarella, *Materials*, 2019, **12**, 1481.

39 Y. Zhao, Z. Luo, M. H. Li, Q. Y. Qu, X. Ma, S. H. Yu and Y. L. Zhao, *Angew. Chem., Int. Ed.*, 2015, **54**, 919–922.

40 S. Wang, D. Ni, H. Yue, N. Luo, X. Xi, Y. Wang, M. Shi, W. Wei and G. Ma, *Small*, 2018, **14**, e1704272.

41 Y. Zhao, L. N. Lin, Y. Lu, S. F. Chen, L. Dong and S. H. Yu, *Adv. Mater.*, 2010, **22**, 5255–5259.

42 Z. Dong, L. Feng, Y. Hao, M. Chen, M. Gao, Y. Chao, H. Zhao, W. Zhu, J. Liu, C. Liang, Q. Zhang and Z. Liu, *J. Am. Chem. Soc.*, 2018, **140**, 2165–2178.

43 L. Kang, M. Cui, F. Jiang, Y. Gao, H. Luo, J. Liu, W. Liang and C. Zhi, *Adv. Energy Mater.*, 2018, **8**, 1801090.

44 G. Begum, T. N. Reddy, K. P. Kumar, K. Dhevendar, S. Singh, M. Amarnath, S. Misra, V. K. Rangari and R. K. Rana, *ACS Appl. Mater. Interfaces*, 2016, **8**, 22056–22063.

45 R. V. Chernozem, M. A. Surmeneva, S. N. Shkarina, K. Loza, M. Epple, M. Ulbricht, A. Cecilia, B. Krause, T. Baumbach, A. A. Abalymov, B. V. Parakhonskiy, A. G. Skirtach and R. A. Surmenev, *ACS Appl. Mater. Interfaces*, 2019, **11**, 19522–19533.

46 M. Fujioka-Kobayashi, K. Tsuru, H. Nagai, K. Fujisawa, T. Kudoh, G. Ohe, K. Ishikawa and Y. Miyamoto, *J. Tissue Eng. Regen. Med.*, 2018, **12**, 2077–2087.

47 X. Li, X. Yang, X. Liu, W. He, Q. Huang, S. Li and Q. Feng, *Prog. Nat. Sci.: Mater. Int.*, 2018, **28**, 598–608.

48 N. Xu, J. Xu, X. Zheng and J. Hui, *ChemistryOpen*, 2020, **9**, 451–458.

49 H. Shi, L. Li, L. Zhang, T. Wang, C. Wang, D. Zhu and Z. Su, *CrystEngComm*, 2015, **17**, 4768–4773.

50 P. Xue, M. Hou, L. Sun, Q. Li, L. Zhang, Z. Xu and Y. Kang, *Acta Biomater.*, 2018, **81**, 242–255.

51 Y. Zhou, H. Li, J. Liu, Y. Xu, Y. Wang, H. Ren and X. Li, *Polym. Adv. Technol.*, 2019, **30**, 143–152.

52 P. Shi, D. Zhou, Y. Zhu, B. Peng, N. Shao and X. Zan, *ACS Appl. Bio Mater.*, 2021, **4**, 1030–1037.

53 M. Kim, J. H. Lee, S. E. Kim, S. S. Kang and G. Tae, *ACS Appl. Mater. Interfaces*, 2016, **8**, 8409–8418.

54 J. Lee, H. S. Min, D. G. You, K. Kim, I. C. Kwon, T. Rhim and K. Y. Lee, *J. Controlled Release*, 2016, **223**, 197–206.

55 Z. Dong, L. Feng, W. Zhu, X. Sun, M. Gao, H. Zhao, Y. Chao and Z. Liu, *Biomaterials*, 2016, **110**, 60–70.

56 H. Huang, W. Zhang, Z. Liu, H. Guo and P. Zhang, *Ultrasonics*, 2020, **108**, 106198.

57 B. Cantaert, D. Kuo, S. Matsumura, T. Nishimura, T. Sakamoto and T. Kato, *ChemPlusChem*, 2017, **82**, 107–120.

58 J. H. E. Cartwright, A. G. Checa, J. D. Gale, D. Gebauer and C. I. Sainz-Diaz, *Angew. Chem., Int. Ed.*, 2012, **51**, 11960–11970.

59 L. B. Gower, *Chem. Rev.*, 2008, **108**, 4551–4627.

60 Y. Oaki, S. Kajiyama, T. Nishimura, H. Imai and T. Kato, *Adv. Mater.*, 2008, **20**, 3633–3637.

61 I. Buljan Meić, J. Kontrec, D. Domazet Jurašin, A. Selmani, B. Njegić Džakula, N. Maltar-Strmečki, D. M. Lyons, M. Plodinec, M. Čeh, A. Gajović, M. D. Sikirić and D. Kralj, *CrystEngComm*, 2018, **20**, 35–50.

62 R. K. Pai and S. Pillai, *CrystEngComm*, 2008, **10**, 865–872.

63 H. Du, C. Courrégelongue, J. Xto, A. Böhlen, M. Steinacher, C. N. Borca, T. Huthwelker and E. Amstad, *Chem. Mater.*, 2020, **32**, 4282–4291.

64 S. Y. Yang, H. H. Chang, C. J. Lin, S. J. Huang and J. C. Chan, *Chem. Commun.*, 2016, **52**, 11527–11530.

65 C. Rao, M. Li, X. Sun, M. Li, X. Lian, H. Wang, L. Jia, B. Niu and W. Li, *Mater. Chem. Phys.*, 2020, **255**, 123552.

66 M. Milovanovic, M. T. Unruh, V. Brandt and J. C. Tiller, *J. Colloid Interface Sci.*, 2020, **579**, 357–368.

67 G. B. Cai, G. X. Zhao, X. K. Wang and S. H. Yu, *J. Phys. Chem. C*, 2010, **114**, 12948–12954.

68 D. J. Tobler, J. D. Rodriguez-Blanco, K. Dideriksen, N. Bovet, K. K. Sand and S. L. S. Stipp, *Adv. Funct. Mater.*, 2015, **25**, 3081–3090.

69 R. Sun, C.-W. Tai, M. Strømme and O. Cheung, *Microporous Mesoporous Mater.*, 2020, **292**, 109736.

70 S. T. Sun, L. B. Mao, Z. Y. Lei, S. H. Yu and H. Colfen, *Angew. Chem., Int. Ed.*, 2016, **55**, 11765–11769.

71 S.-C. Huang, T. Minami, K. Naka and Y. Chujo, *Polym. Compos.*, 2015, **36**, 330–335.

72 C. Wang, M. Han, X. Liu, S. Chen, F. Hu, J. Sun and H. Yuan, *Int. J. Nanomed.*, 2019, **14**, 1503–1517.

73 C. C. Xue, M. H. Li, Y. Zhao, J. Zhou, Y. Hu, K. Y. Cai, Y. L. Zhao, S. H. Yu and Z. Luo, *Sci. Adv.*, 2020, **6**, 2008732.

74 L. Shi, M. Tang, Y. Muhammad, Y. Tang, L. He, W. Wang, Z. Tong and L. Li, *CrystEngComm*, 2021, **23**, 3033–3042.

75 C. Qi, J. Lin, L. H. Fu and P. Huang, *Chem. Soc. Rev.*, 2018, **47**, 357–403.

76 Y. I. Svenskaya, H. Fattah, O. A. Inozemtseva, A. G. Ivanova, S. N. Shtykov, D. A. Gorin and B. V. Parakhonskiy, *Cryst. Growth Des.*, 2018, **18**, 331–337.

77 O. A. Jimoh, K. S. Ariffin, H. B. Hussin and A. E. Temitope, *Carbonates Evaporites*, 2017, **33**, 331–346.

78 B. Rugabirwa, D. Murindababisha, Y. Li, Y. Hong, Y. Su, H. Wang and J. Li, *ACS Sustainable Chem. Eng.*, 2019, **7**, 6251–6258.

79 R. Salomão, L. M. M. Costa and G. M. Olyveira, *Adv. Tissue Eng. Regen. Med.*, 2017, **3**, 336–340.

80 D. Gebauer, A. Volkel and H. Colfen, *Science*, 2008, **322**, 1819–1822.

81 D. Gebauer and H. Cölfen, *Nano Today*, 2011, **6**, 564–584.

82 N. Wada, N. Horiuchi, M. Nakamura, K. Nozaki, A. Nagai and K. Yamashita, *ACS Omega*, 2018, **3**, 16681–16692.

83 J. Jiang, C. Chen, B. Xiao, Z. Bai, C. Jiang, C. Yang, Y. Wu and X. Wang, *CrystEngComm*, 2017, **19**, 7332–7338.

84 V. Vergaro, E. Carata, F. Baldassarre, E. Panzarini, L. Dini, C. Carlucci, S. Leporatti, B. F. Scremin, D. Altamura, C. Giannini, F. P. Fanizzi and G. Ciccarella, *Adv. Powder Technol.*, 2017, **28**, 2445–2455.

85 J. Q. Qi, R. Guo, Y. Wang, X. W. Liu and H. L. Chan, *Nanoscale Res. Lett.*, 2016, **11**, 120.

86 J. A. Juhasz-Bortuzzo, B. Myszka, R. Silva and A. R. Boccaccini, *Cryst. Growth Des.*, 2017, **17**, 2351–2356.

87 B. Njegić Džakula, J. Kontrec, M. Ukrainczyk, S. Sviben and D. Kralj, *Cryst. Res. Technol.*, 2014, **49**, 244–256.

88 N. M. Mlinarić, J. Kontrec, B. N. Džakula, G. Falini and D. Kralj, *Crystals*, 2021, **11**, 250.

89 Z. M. Liu, C. Y. Shao, B. Jin, Z. S. Zhang, Y. Q. Zhao, X. R. Xu and R. K. Tang, *Nature*, 2019, **574**, 394–398.

90 Z. Mu, K. Kong, K. Jiang, H. Dong, X. Xu, Z. Liu and R. Tang, *Science*, 2021, **372**, 1466–1470.

91 P. J. M. Smeets, A. R. Finney, W. Habraken, F. Nudelman, H. Friedrich, J. Laven, J. J. De Yoreo, P. M. Rodger and N. Sommerdijk, *Proc. Natl. Acad. Sci. U. S. A.*, 2017, **114**, E7882–E7890.

92 E. M. Pouget, P. H. H. Bomans, J. A. C. M. Goos, P. M. Frederik, G. de With and N. A. J. M. Sommerdijk, *Science*, 2009, **323**, 1455–1458.

93 Y. Y. Kim, E. P. Douglas and L. B. Gower, *Langmuir*, 2007, **23**, 4862–4870.

94 H. Du and E. Amstad, *Angew. Chem., Int. Ed.*, 2020, **59**, 1798–1816.

95 A. D. Trofimov, A. A. Ivanova, M. V. Zyuzin and A. S. Timin, *Pharmaceutics*, 2018, **10**, 167.

96 A. Sarkar and S. Mahapatra, *Cryst. Growth Des.*, 2010, **10**, 2129–2135.

97 I. Buljan Meić, J. Kontrec, D. Domazet Jurašin, B. Njegić Džakula, L. Štajner, D. M. Lyons, M. Dutour Sikirić and D. Kralj, *Cryst. Growth Des.*, 2017, **17**, 1103–1117.

98 W. Ostwald, *Z. Phys. Chem.*, 1897, **22**, 289–330.

99 G. Montes-Hernandez, F. Renard, N. Findling and A. L. Auzende, *CrystEngComm*, 2015, **17**, 5725–5733.

100 T. Zheng, H. Yi, S. Zhang and C. Wang, *J. Cryst. Growth*, 2020, **549**, 125870.

101 B. V. Parakhonskiy, A. M. Yashchenok, S. Donatan, D. V. Volodkin, F. Tessarolo, R. Antolini, H. Mohwald and A. G. Skirtach, *ChemPhysChem*, 2014, **15**, 2817–2822.

102 L. Brečević and D. Kralj, *Kinetics and mechanisms of crystal growth in aqueous systems*, Interfacial Dynamics, 2000.

103 D. Konopacka-Łyskawa, *Crystals*, 2019, **9**, 223.

104 Y. Mori, T. Enomae and A. Isogai, *Mater. Sci. Eng., C*, 2009, **29**, 1409–1414.

105 R. Evík, M. Pérez-Estébanez, A. Viani, P. Aek and P. Mácová, *Powder Technol.*, 2015, **284**, 265–271.

106 S. Yamanaka, Y. Sugawara, T. Oiso, T. Fujimoto, Y. Ohira and Y. Kuga, *CrystEngComm*, 2015, **17**, 1773–1777.

107 A. T. Nagaraja, S. Pradhan and M. J. McShane, *J. Colloid Interface Sci.*, 2014, **418**, 366–372.

108 G. J. Price, M. F. Mahon, J. Shannon and C. Cooper, *Cryst. Growth Des.*, 2011, **11**, 39–44.

109 Ç. M. Oral and B. Ercan, *Powder Technol.*, 2018, **339**, 781–788.

110 B. Rugabirwa, D. Murindababisha, H. Wang and J. Li, *Cryst. Growth Des.*, 2018, **19**, 242–248.

111 C. Y. Tai and C.-k Chen, *Chem. Eng. Sci.*, 2008, **63**, 3632–3642.

112 J. Jiang, Y. Ma, T. Zhang, Z. Liang and Z. Cui, *RSC Adv.*, 2015, **5**, 80216–80219.

113 A. U. Badnore and A. B. Pandit, *Chem. Eng. Process.*, 2015, **98**, 13–21.

114 K. Murai, T. Kinoshita, K. Nagata and M. Higuchi, *Langmuir*, 2016, **32**, 9351–9359.

115 B. Parakhonskiy, M. V. Zyuzin, A. Yashchenok, S. Carregal-Romero, J. Rejman, H. Mohwald, W. J. Parak and A. G. Skirtach, *J. Nanobiotechnol.*, 2015, **13**, 53.

116 D. Kralj, J. Kontrec, L. Brecevic, G. Falini and V. Nothig-Laslo, *Chemistry*, 2004, **10**, 1647–1656.

117 L. N. Plummer and E. Busenberg, *Geochim. Cosmochim. Acta*, 1982, **46**, 1011–1040.

118 D. Kralj, L. Brečević and A. E. Nielsen, *J. Cryst. Growth*, 1990, **104**, 793–800.

119 B. Njegić Džakula, S. Fermani, Z. Dubinsky, S. Goffredo, G. Falini and D. Kralj, *Chem. – Eur. J.*, 2019, **25**, 10616–10624.

120 Y. Zhao, W. Du, L. Sun, L. Yu, J. Jiao and R. Wang, *Colloid Polym. Sci.*, 2013, **291**, 2191–2202.

121 H. Tang, J. Yu, X. Zhao and D. H. L. Ng, *J. Alloys Compd.*, 2008, **463**, 343–349.

122 J. Kontrec, N. Tomašić, N. Matijaković Mlinarić, D. Kralj and B. Njegić Džakula, *Crystals*, 2021, **11**, 1075.

123 T. E. Reilly, L. N. Plummer, P. J. Phillips and E. Busenberg, *Water Resour. Res.*, 1994, **30**, 421–433.

124 J. L. Bischoff, J. A. Fitzpatrick and R. J. Rosenbauer, *J. Geol.*, 1993, **101**, 21–33.

125 D. Kralj and L. Brecevic, *Colloids Surf., A*, 1995, **96**, 287.

126 L. Brečević and A. E. Nielsen, *J. Cryst. Growth*, 1989, **98**, 504–510.

127 Q. Hu, J. Zhang, H. Teng and U. Becker, *Am. Mineral.*, 2012, **97**, 1437–1445.

128 J. Kawano, N. Shimobayashi, A. Miyake and M. Kitamura, *J. Phys.: Condens. Matter*, 2009, **21**, 425102.

129 M. Ma, Y. Wang, X. Cao, W. Lu and Y. Guo, *Cryst. Growth Des.*, 2019, **19**, 6972–6988.

130 Y.-B. Hu, M. Wolthers, D. A. Wolf-Gladrow and G. Nehrke, *Cryst. Growth Des.*, 2015, **15**, 1596–1601.

131 J. Chen and L. Xiang, *Powder Technol.*, 2009, **189**, 64–69.

132 R. Ševčík, M. Pérez-Estébanez, A. Viani, P. Šašek and P. Mácová, *Powder Technol.*, 2015, **284**, 265–271.

133 S. Sovova, A. Abalymov, M. Pekar, A. G. Skirtach and B. Parakhonskiy, *J. Mater. Chem. B*, 2021, **9**, 8308–8320.

134 J.-P. Andreassen, *J. Cryst. Growth*, 2005, **274**, 256–264.

135 J.-P. Andreassen and M. J. Hounslow, *AIChE J.*, 2004, **50**, 2772–2782.

136 E. Altay, T. Shahwan and M. Tanoğlu, *Powder Technol.*, 2007, **178**, 194–202.

137 S. Gopi, V. K. Subramanian and K. Palanisamy, *Mater. Res. Bull.*, 2013, **48**, 1906–1912.

138 S. Fermani, B. Njegić Džakula, M. Reggi, G. Falini and D. Kralj, *CrystEngComm*, 2017, **19**, 2451–2455.

139 D. Gebauer, *Minerals*, 2018, **8**, 179.

140 R. Demichelis, A. Schuitemaker, N. A. Garcia, K. B. Koziara, M. De La Pierre, P. Raiteri and J. D. Gale, *Annu. Rev. Mater. Sci.*, 2018, **48**, 327–352.

141 J. J. De Yoreo and P. G. Vekilov, *Rev. Mineral. Geochem.*, 2003, **54**, 57–93.

142 T. N. Ramesh, S. A. Inchara and K. Pallavi, *J. Chem. Sci.*, 2015, **127**, 843–848.

143 X. Ji, G. Li and X. Huang, *Mater. Lett.*, 2008, **62**, 751–754.

144 J. P. Zou, H. Z. Yang, P. Xiao and Y. F. Pan, *J. Inorg. Mater.*, 2016, **31**, 711–718.

145 N. Hanafy, M. Giorgi, C. Nobile, M. Cascione and S. Leporatti, *Beni-Suef Univ. J. Basic Appl. Sci.*, 2015, **4**, 60–70.

146 J. Bolze, B. Peng, N. Dingenouts, P. Panine, T. Narayanan and M. Ballauff, *Langmuir*, 2002, **18**, 8364–8369.

147 D. Pontoni, J. Bolze, N. Dingenouts, T. Narayanan and M. Ballauff, *J. Phys. Chem. B*, 2003, **107**, 5123–5125.

148 A.-R. Ibrahim, J. B. Vuningoma, X. Hu, Y. Gong, D. Hua, Y. Hong, H. Wang and J. Li, *J. Supercrit. Fluids*, 2012, **72**, 78–83.

149 C. Y. Wang, P. Xiao, J. Z. Zhao, X. Zhao, Y. H. Liu and Z. C. Wang, *Powder Technol.*, 2006, **170**, 31–35.

150 M. Ukrainczyk, J. Kontrec, V. Babić-Ivančić, L. Brečević and D. Kralj, *J. Powder Technol.*, 2007, **171**, 192–199.

151 L. Du, Y. Wang and G. Luo, *Particuology*, 2013, **11**, 421–427.

152 F. C. Donnelly, F. Purcell-Milton, V. Framont, O. Cleary, P. W. Dunne and Y. K. Gun'ko, *Chem. Commun.*, 2017, **53**, 6657–6660.

153 C. W. Turner and D. W. Smith, *Ind. Eng. Chem. Res.*, 1998, **37**, 439–448.

154 G. Zhu, H. Li, S. Li, X. Hou, D. Xu, R. Lin and Q. Tang, *J. Cryst. Growth*, 2015, **428**, 16–23.

155 W. Chuajiw, K. Takatori, T. Igarashi, H. Hara and Y. Fukushima, *J. Cryst. Growth*, 2014, **386**, 119–127.

156 X. Chen, Y. Zhu, Y. Guo, B. Zhou, X. Zhao, Y. Du, H. Lei, M. Li and Z. Wang, *Colloid Surf., A*, 2010, **353**, 97–103.

157 N. Matijaković, G. Magnabosco, F. Scarpino, S. Fermani, G. Falini and D. Kralj, *Crystals*, 2019, **9**, 16.

158 Y. Lai, L. Chen, W. Bao, Y. Ren, Y. Gao, Y. Yin and Y. Zhao, *Cryst. Growth Des.*, 2015, **15**, 1194–1200.

159 D. Walsh, B. Lebeau and S. Mann, *Adv. Mater.*, 1999, **11**, 324–328.

160 Y. Fukui and K. Fujimoto, *J. Mater. Chem.*, 2012, **22**, 3493–3499.

161 T. Beuvier, B. Calvignac, G. J.-R. Delcroix, M. K. Tran, S. Kodjikian, N. Delorme, J.-F. Bardeau, A. Gibaud and F. Boury, *J. Mater. Chem.*, 2011, **21**, 9757–9761.

162 N. McCann, D. Phan, M. Attalla, G. Puxty, D. Fernandes, W. Conway, X. Wang, R. Burns, I. van Altena, G. Lawrance and M. Maeder, *Energy Procedia*, 2009, **1**, 995–1002.

163 J. Kontrec, M. Ukrainczyk, B. N. Džakula and D. Kralj, *Cryst. Res. Technol.*, 2013, **48**, 622–626.

164 Y. Shen, A. Xie, Z. Chen, W. Xu, H. Yao, S. Li, L. Huang, Z. Wu and X. Kong, *Mater. Sci. Eng., A*, 2007, **443**, 95–100.

165 C. Kosanović, S. Fermani, G. Falini and D. Kralj, *Crystals*, 2017, **7**, 355.

166 Y. Y. Kim, R. Darkins, A. Broad, A. N. Kulak, M. A. Holden, O. Nahi, S. P. Armes, C. C. Tang, R. F. Thompson, F. Marin, D. M. Duffy and F. C. Meldrum, *Nat. Commun.*, 2019, **10**, 5682.

167 R. Stepić, L. Jurković, K. Klementyeva, M. Ukrainczyk, M. Gredičak, D. M. Smith, D. Kralj and A. S. Smith, *Cryst. Growth Des.*, 2020, **20**, 2853–2859.

168 S. Weiner and L. Addadi, *J. Mater. Chem.*, 1997, **7**, 689–702.

169 L. Addadi, J. Moradian, E. Shay, N. G. Maroudas and S. Weiner, *Proc. Natl. Acad. Sci. U. S. A.*, 1987, **84**, 2732–2736.

170 L. A. Gower and D. A. Tirrell, *J. Cryst. Growth*, 1998, **191**, 153–160.

171 S. Borukhin, L. Bloch, T. Radlauer, A. H. Hill, A. N. Fitch and B. Pokroy, *Adv. Funct. Mater.*, 2012, **22**, 4216–4224.

172 C. A. Orme, A. Noy, A. Wierzbicki, M. T. McBride, M. Grantham, H. H. Teng, P. M. Dove and J. J. DeYoreo, *Nature*, 2001, **411**, 775–779.

173 Y. M. Guo, F. F. Wang, J. Zhang, L. Yang, X. M. Shi, Q. L. Fang and X. M. Ma, *Res. Chem. Intermed.*, 2013, **39**, 2407–2415.

174 N. Wada, N. Horiuchi, M. Nakamura, K. Nozaki, A. Nagai and K. Yamashita, *Cryst. Growth Des.*, 2018, **18**, 872–878.

175 G. Montanari, L. Z. Lakshtanov, D. J. Tobler, K. Dideriksen, K. N. Dalby, N. Bovet and S. L. S. Stipp, *Cryst. Growth Des.*, 2016, **16**, 4813–4821.

176 F. C. Meldrum and H. Cölfen, *Chem. Rev.*, 2008, **108**, 4332–4432.

177 B. Njegić-Džakula, L. Brečević, G. Falini and D. Kralj, *Cryst. Growth Des.*, 2009, **9**, 2425–2434.

178 P. J. Smeets, K. R. Cho, R. G. Kempen, N. A. Sommerdijk and J. J. De Yoreo, *Nat. Mater.*, 2015, **14**, 394–399.

179 H. Deng, S. Wang, X. Wang, C. Du, X. Shen, Y. Wang and F. Cui, *Regener. Biomater.*, 2015, **2**, 187–195.

180 S. Xu, H. Zhang, B. Qiao and Y. Wang, *Cryst. Growth Des.*, 2021, **21**, 7306–7325.

181 H. Colfen and S. Mann, *Angew. Chem., Int. Ed.*, 2003, **42**, 2350–2365.

182 M. Jehannin, A. Rao and H. Colfen, *J. Am. Chem. Soc.*, 2019, **141**, 10120–10136.

183 D. Gebauer, M. Kellermeier, J. D. Gale, L. Bergstrom and H. Colfen, *Chem. Soc. Rev.*, 2014, **43**, 2348–2371.

184 R. Demichelis, P. Raiteri, J. D. Gale, D. Quigley and D. Gebauer, *Nat. Commun.*, 2011, **2**, 590.

185 J. Rieger, M. Kellermeier and L. Nicoleau, *Angew. Chem., Int. Ed.*, 2014, **53**, 12380–12396.

186 P. Bots, L. G. Benning, J.-D. Rodriguez-Blanco, T. Roncal-Herrero and S. Shaw, *Cryst. Growth Des.*, 2012, **12**, 3806–3814.

187 Y. Politi, R. A. Metzler, M. Abrecht, B. Gilbert, F. H. Wilt, I. Sagi, L. Addadi, S. Weiner and P. U. P. A. Gilbert, *Proc. Natl. Acad. Sci. U. S. A.*, 2008, **105**, 17362–17366.

188 J. Seto, Y. Ma, S. A. Davis, F. Meldrum, A. Gourrier, Y. Y. Kim, U. Schilde, M. Sztucki, M. Burghammer, S. Maltsev, C. Jager and H. Colfen, *Proc. Natl. Acad. Sci. U. S. A.*, 2012, **109**, 3699–3704.

189 L. Granasy, T. Pusztai, G. Tegze, J. A. Warren and J. F. Douglas, *Phys. Rev. E: Stat., Nonlinear, Soft Matter Phys.*, 2005, **72**, 011605.

190 J. D. Rodriguez-Blanco, S. Shaw and L. G. Benning, *Nanoscale*, 2011, **3**, 265–271.

191 W.-L. Tan, A. L. Ahmad, C. P. Leo and S. S. Lam, *J. CO2 Util.*, 2020, **42**, 101333.

192 J. Pedrosa, J. A. F. Gamelas, A. F. Lourenço and P. J. Ferreira, *Colloid Surf., A*, 2016, **497**, 1–7.

193 Y. U. Liang, S. Sun, H. A. O. Ding and X. Hou, *Surf. Rev. Lett.*, 2020, **27**, 1950224.

194 A. Sarkar, A. K. Ghosh and S. Mahapatra, *J. Mater. Chem.*, 2012, **22**, 11113.

195 A. Barhoum, L. Van Lokeren, H. Rahier, A. Dufresne and G. Van Assche, *J. Mater. Sci.*, 2015, **50**, 7908–7918.

196 G. Cheng, X. Yu, G. Ding and C. Xu, *Asian J. Chem.*, 2013, **25**, 5558–5560.

197 L. C. Li and Y. Zhang, *Adv. Mater. Res.*, 2009, **79-82**, 1967–1970.

198 Z. Tang, G. Cheng, Y. Chen, X. Yu and H. Wang, *Adv. Powder Technol.*, 2014, **25**, 1618–1623.

199 J. Lee, S. H. Jo and J. Lim, *J. Ind. Eng. Chem.*, 2019, **74**, 63–70.

200 N. Shimpi, A. Mali, D. P. Hansora and S. Mishra, *Nanosci. Nanoeng.*, 2015, **3**, 8–12.

201 Y. Zhou, S. Wang, Y. Zhang and Y. Zhang, *J. Polym. Sci., Part B: Polym. Phys.*, 2006, **44**, 1226–1236.

202 L. M. Racca, L. C. Bertolino, C. R. Nascimento, A. M. F. de Sousa, L. Y. Reznik, L. Yokoyama and A. L. N. da Silva, *J. Nanopart. Res.*, 2019, **21**, 232.

203 J. Kim, S. K. Bea, Y. H. Kim, D.-W. Kim, K.-Y. Lee and C.-M. Lee, *Biotechnol. Bioprocess Eng.*, 2015, **20**, 794–799.

204 Z. Cao, M. Daly, L. Clémence, L. M. Geever, I. Major, C. L. Higginbotham and D. M. Devine, *Appl. Surf. Sci.*, 2016, **378**, 320–329.

205 S. R. Mihajlović, D. R. Vučinić, Ž. T. Sekulić, S. Z. Milićević and B. M. Kolonja, *Powder Technol.*, 2013, **245**, 208–216.

206 C. Jeon, S. Park, J.-H. Bang, S. Chae, K. Song and S.-W. Lee, *Coatings*, 2018, **8**, 43.

207 E. Yoğurtcuoğlu and M. Uçurum, *Powder Technol.*, 2011, **214**, 47–53.

208 Deepika, S. K. Hait and Y. Chen, *J. Coat. Technol. Res.*, 2014, **11**, 273–282.

209 C. Zeng, H. Hu, X. Feng, K. Wang and Q. Zhang, *Chemosphere*, 2020, **249**, 126227.

210 Deepika, S. K. Hait, J. Christopher, Y. Chen, P. Hodgson and D. K. Tuli, *Powder Technol.*, 2013, **235**, 581–589.

211 D. Kim, J. Lee, S. Lee and J. Lim, *Colloid Surf., A*, 2018, **536**, 213–223.

212 E. Song, D. Kim, B. J. Kim and J. Lim, *Colloid Surf., A*, 2014, **461**, 1–10.

213 Z. G. Cui, Y. Z. Cui, C. F. Cui, Z. Chen and B. P. Binks, *Langmuir*, 2010, **26**, 12567–12574.

214 E. M. Song, D. W. Kim and J. C. Lim, *J. Ind. Eng. Chem.*, 2015, **28**, 351–358.

215 D. S. Kim and C. K. Lee, *Appl. Surf. Sci.*, 2002, **202**, 15–23.

216 S. Zhang and X. Li, *Powder Technol.*, 2004, **141**, 75–79.

217 C. Cui, H. Ding, L. Cao and D. Chen, *Pol. J. Chem. Technol.*, 2015, **17**, 128–133.

218 L. Jiang, K. Pan and Y. Dan, *Colloid Polym. Sci.*, 2006, **285**, 65–74.

219 A. M. Ferreira, A. S. Vikulina and D. Volodkin, *J. Controlled Release*, 2020, **328**, 470–489.

220 S. Sharma, A. Verma, B. V. Teja, G. Pandey, N. Mittapelly, R. Trivedi and P. R. Mishra, *Colloid Surf., B*, 2015, **133**, 120–139.

221 G. Choukrani, B. Maharjan, C. H. Park, C. S. Kim and A. R. Kurup Sasikala, *Mater. Sci. Eng., C*, 2020, **106**, 110226.

222 K. H. Min, H. S. Min, H. J. Lee, D. J. Park, J. Y. Yhee, K. Kim, I. C. Kwon, S. Y. Jeong, O. F. Silvestre, X. Chen, Y.-S. Hwang, E.-C. Kim and S. C. Lee, *ACS Nano*, 2015, **9**, 134–145.

223 D. J. Park, K. H. Min, H. J. Lee, K. Kim, I. C. Kwon, S. Y. Jeong and S. C. Lee, *J. Mat. Chem. B*, 2016, **4**, 1219–1227.

224 Y. Fujita, T. Yamamuro, T. Nakamura, S. Kotani, C. Ohtsuki and T. Kokubo, *J. Biomed. Mater. Res.*, 1991, **25**, 991–1003.

225 C. Combes, B. Miao, R. Bareille and C. Rey, *Biomaterials*, 2006, **27**, 1945–1954.

226 F. P. He, J. Zhang, F. W. Yang, J. X. Zhu, X. M. Tian and X. M. Chen, *Mater. Sci. Eng., C*, 2015, **50**, 257–265.

227 S. Umemoto, T. Furusawa, H. Unuma, M. Tajika and T. Sekino, *Dent. Mater. J.*, 2021, **40**, 1202–1207.

228 Q. W. Zhong, W. H. Li, X. P. Su, G. Li, Y. Zhou, S. C. Kundu, J. M. Yao and Y. R. Cai, *Colloid Surf., B*, 2016, **143**, 56–63.

229 J. Rodríguez-Sánchez, B. Myszka, A. R. Boccaccini and D. K. Dysthe, *J. Am. Ceram. Soc.*, 2019, **102**, 6980–6990.

230 A. Diez-Escudero, M. Espanol and M.-P. Ginebra, *Synthetic bone graft substitutes: Calcium-based biomaterials*, Woodhead Publishing, 2020.

231 B. Myszka, K. Hurle, K. Zheng, S. E. Wolf and A. R. Boccaccini, *J. Mater. Chem. B*, 2019, **7**, 3403–3411.

232 P. Opitz, L. Besch, M. Panthöfer, A. Kabelitz, R. E. Unger, F. Emmerling, M. Mondeshki and W. Tremel, *Adv. Funct. Mater.*, 2021, **31**, 2007830.

233 S. Kim and C. B. Park, *Adv. Funct. Mater.*, 2013, **23**, 10–25.

234 Y. Lee, Y. M. Hahm, S. Matsuya, M. Nakagawa and K. Ishikawa, *J. Mater. Sci.*, 2007, **42**, 5728–5735.

235 C. T. Begley, M. J. Doherty, R. A. B. Mollan and D. J. Wilson, *Biomaterials*, 1995, **16**, 1181–1185.

236 Y. Barbotteau, J. L. Irigaray and J. F. Mathiot, *Phys. Med. Biol.*, 2003, **48**, 3611–3623.

237 S. Rossler, R. Unbehau, T. Gemming, B. Kruppke, H. P. Wiesmann and T. Hanke, *Sci. Rep.*, 2020, **10**, 118.

238 M. Xie, M. O. Olderoy, J. P. Andreassen, S. M. Selbach, B. L. Strand and P. Sikorski, *Acta Biomater.*, 2010, **6**, 3665–3675.

239 Y. Suzawa, T. Funaki, J. Watanabe, S. Iwai, Y. Yura, T. Nakano, Y. Umakoshi and M. Akashi, *J. Biomed. Mater. Res. Part A*, 2010, **93A**, 965–975.

240 N. H. Munro and K. M. McGrath, *Chem. Commun.*, 2012, **48**, 4716–4718.

241 H. Li, H. L. Xin, D. A. Muller and L. A. Estroff, *Science*, 2009, **326**, 1244–1247.

242 O. Grassmann and P. Lobmann, *Chem. – Eur. J.*, 2003, **9**, 1310–1316.

243 Y. H. Gong, Y. L. Zhang, Z. N. Cao, F. Ye, Z. F. Lin and Y. Li, *Biomater. Sci.*, 2019, **7**, 3614–3626.

244 N. Rauner, M. Meuris, S. Dech, J. Godde and J. C. Tiller, *Acta Biomater.*, 2014, **10**, 3942–3951.

245 T. E. L. Douglas, A. Lapa, S. K. Samal, H. A. Declercq, D. Schaubroeck, A. C. Mendes, P. V. der Voort, A. Dokupil, A. Plis, K. De Schamphelaere, I. S. Chronakis, E. Pamula and A. G. Skirtach, *J. Tissue Eng. Regen. Med.*, 2017, **11**, 3556–3566.

246 M. Li, H. Ma, F. Han, D. Zhai, B. Zhang, Y. Sun, T. Li, L. Chen and C. Wu, *Adv. Mater.*, 2021, **9**, e2104829.

247 Q. Huang, Y. Liu, Z. Ouyang and Q. Feng, *Bioact. Mater.*, 2020, **5**, 980–989.

248 C. Dhand, S. T. Ong, N. Dwivedi, S. M. Diaz, J. R. Venugopal, B. Navaneethan, M. H. Fazil, S. Liu, V. Seitz, E. Wintermantel, R. W. Beuerman, S. Ramakrishna, N. K. Verma and R. Lakshminarayanan, *Biomaterials*, 2016, **104**, 323–338.

249 Y. C. Wu, T. M. Lee, K. H. Chiu, S. Y. Shaw and C. Y. Yang, *J. Mater. Sci.: Mater. Med.*, 2009, **20**, 1273–1280.

250 V. Viateau, M. Manassero, L. Sensebe, A. Langonne, D. Marchat, D. Logeart-Avramoglou, H. Petite and M. Bensidhoum, *J. Tissue Eng. Regener. Med.*, 2016, **10**, E177–187.

251 C. T. Tran, C. Gargiulo, H. D. Thao, H. M. Tuan, L. Filgueira and D. Michael Strong, *Cell Tissue Bank.*, 2010, **12**, 247–261.

252 B. Kruppke, J. Farack, S. Weil, E. D. Aflalo, D. Polakova, A. Sagi and T. Hanke, *J. Biomed. Mater. Res., Part A*, 2020, **108**, 694–708.

253 M. S. Saveleva, A. N. Ivanov, M. O. Kurtukova, V. S. Atkin, A. G. Ivanova, G. P. Lyubun, A. V. Martyukova, E. I. Cherevko, A. K. Sargsyan, A. S. Fedonnikov, I. A. Norkin, A. G. Skirtach, D. A. Gorin and B. V. Parakhonskiy, *Mater. Sci. Eng., C*, 2018, **85**, 57–67.

254 A. D. Woldetsadik, S. K. Sharma, S. Khapli, R. Jagannathan and M. Magzoub, *ACS Biomater. Sci. Eng.*, 2017, **3**, 2457–2469.

255 Q. Li, E. Hu, K. Yu, R. Xie, F. Lu, B. Lu, R. Bao, T. Zhao, F. Dai and G. Lan, *Adv. Funct. Mater.*, 2020, **30**, 2004153.

256 W. He, X. Huang, J. Zhang, Y. Zhu, Y. Liu, B. Liu, Q. Wang, X. Huang and D. He, *Materials*, 2021, **14**, 3350.

257 J. K. Jang, O. S. Lee, T. J. Kang and S. C. Lim, *Food Sci. Biotechnol.*, 2013, **22**, 99–105.

258 J. R. Baylis, J. H. Yeon, M. H. Thomson, A. Kazerooni, X. Wang, A. E. St John, E. B. Lim, D. Chien, A. Lee, J. Q. Zhang, J. M. Piret, L. S. Machan, T. F. Burke, N. J. White and C. J. Kastrup, *Sci. Adv.*, 2015, **1**, e1500379.

259 B. T. Turner, Jr. and M. C. Maurer, *Biochemistry*, 2002, **41**, 7947–7954.

260 M. L. P. Vidallon, A. M. Douek, A. Quek, H. McLiesh, J. Kaslin, R. F. Tabor, A. I. Bishop and B. M. Teo, *Part. Part. Syst. Charact.*, 2020, **37**, 1900471.

261 C. Qi, J. Lin, L. H. Fu and P. Huang, *Chem. Soc. Rev.*, 2018, **47**, 357–403.

262 M. Kim, J. H. Lee, S. E. Kim, S. S. Kang and G. Tae, *ACS Appl. Mater. Interfaces*, 2016, **8**, 8409–8418.

263 Z. Wei, X. Lin, M. Wu, B. Zhao, R. Lin, D. Zhang, Y. Zhang, G. Liu, X. Liu and J. Liu, *Sci. Rep.*, 2017, **7**, 5370.

264 S. L. Goss, K. A. Lemons, J. E. Kerstetter and R. H. Bogner, *J. Pharm. Pharmacol.*, 2007, **59**, 1485–1492.

265 J. Zhang, Y. Li, H. Xie, B. L. Su, B. Yao, Y. Yin, S. Li, F. Chen and Z. Fu, *ACS Appl. Mater. Interfaces*, 2015, **7**, 15686–15691.

266 J. Li, H. Jiang, X. Ouyang, S. Han, J. Wang, R. Xie, W. Zhu, N. Ma, H. Wei and Z. Jiang, *ACS Appl. Mater. Interfaces*, 2016, **8**, 30027–30036.

267 Q. Q. Dong, J. L. Li, L. Y. Cui, H. L. Jian, A. H. Wang and S. Bai, *Colloid Surf., A*, 2017, **516**, 190–198.

268 X. Y. Wan, H. Zhong, W. Pan, Y. H. Li, Y. Y. Chen, N. Li and B. Tang, *Angew. Chem., Int. Ed.*, 2019, **58**, 14134–14139.

269 Q. Guan, L. L. Zhou, F. H. Lv, W. Y. Li, Y. A. Li and Y. B. Dong, *Angew. Chem., Int. Ed.*, 2020, **59**, 18042–18047.

270 M. Chang, Z. Hou, D. Jin, J. Zhou, M. Wang, M. Wang, M. Shu, B. Ding, C. Li and J. Lin, *Adv. Mater.*, 2020, **32**, 2004647.

271 Y. Liu, B. Yu, X. Dai, N. Zhao and F. J. Xu, *Biomaterials*, 2021, **274**, 120885.

272 C. Y. Xu, Y. F. Yan, J. C. Tan, D. H. Yang, X. J. Jia, L. Wang, Y. S. Xu, S. Cao and S. T. Sun, *Adv. Funct. Mater.*, 2019, **29**, 1808146.

273 J. J. Xing, Y. Q. Cai, Y. K. Wang, H. F. Zheng and Y. J. Liu, *Adv. Polym. Technol.*, 2020, 8749238.

274 S. Maleki Dizaj, M. Barzegar-Jalali, M. H. Zarrintan, K. Adibkia and F. Lotfipour, *Expert Opin. Drug Delivery*, 2015, **12**, 1649–1660.

275 Y. Zhang, P. Ma, Y. Wang, J. Du, Q. Zhou, Z. Zhu, X. Yang and J. Yuan, *World J. Nano Sci. Eng.*, 2012, **02**, 25–31.

276 S. Haruta, T. Hanafusa, H. Fukase, H. Miyajima and T. Oki, *Diabetes Technol. Ther.*, 2003, **5**, 1–9.

277 D. Preisig, D. Haid, F. J. O. Varum, R. Bravo, R. Alles, J. Huwyler and M. Puchkov, *Eur. J. Pharm. Biopharm.*, 2014, **87**, 548–558.

278 G. Magnabosco, M. Di Giosia, I. Polishchuk, E. Weber, S. Fermani, A. Bottoni, F. Zerbetto, P. G. Pelicci, B. Pokroy, S. Rapino, G. Falini and M. Calvaresi, *Adv. Healthcare Mater.*, 2015, **4**, 1510–1516.

279 M. Barbalinardo, M. Di Giosia, I. Polishchuk, G. Magnabosco, S. Fermani, F. Biscarini, M. Calvaresi, F. Zerbetto, G. Pellegrini, G. Falini, B. Pokroy and F. Valle, *J. Mat. Chem. B*, 2019, **7**, 5808–5813.

280 R. Kurapati and A. M. Raichur, *J. Mat. Chem. B*, 2013, **1**, 3175–3184.

281 X. Ma, S. Yuan, L. Yang, L. Li, X. Zhang, C. Su and K. Wang, *CrystEngComm*, 2013, **15**, 8288–8299.

282 H. Z. Shi, L. Li, L. Y. Zhang, T. T. Wang, C. G. Wang, D. X. Zhu and Z. M. Su, *CrystEngComm*, 2015, **17**, 4768–4773.

283 S. Maleki Dizaj, S. Sharifi, E. Ahmadian, A. Eftekhari, K. Adibkia and F. Lotfipour, *Expert Opin. Drug Delivery*, 2019, **16**, 331–345.

284 T. Yang, Z. Wan, Z. Liu, H. Li, H. Wang, N. Lu, Z. Chen, X. Mei and X. Ren, *Mater. Sci. Eng., C*, 2016, **63**, 384–392.

285 D. Zhao, C. Q. Wang, R. X. Zhuo and S. X. Cheng, *Colloids Surf., B*, 2014, **118**, 111–116.

286 Y. Wu, W. Gu, J. Tang and Z. P. Xu, *J. Mat. Chem. B*, 2017, **5**, 7194–7203.

287 C. Q. Wang, J. L. Wu, R. X. Zhuo and S. X. Cheng, *Mol. Biosyst.*, 2014, **10**, 672–678.

288 P. Liang, C.-Q. Wang, H. Chen, R.-X. Zhuo and S.-X. Cheng, *Polym. Int.*, 2015, **64**, 647–653.

289 P. Shi, S. Luo, B. Voit, D. Appelhans and X. Zan, *J. Mat. Chem. B*, 2018, **6**, 4205–4215.

290 Q. Chen, C. Wang, X. Zhang, G. Chen, Q. Hu, H. Li, J. Wang, D. Wen, Y. Zhang, Y. Lu, G. Yang, C. Jiang, J. Wang, G. Dotti and Z. Gu, *Nat. Nanotechnol.*, 2019, **14**, 89–97.

291 H. Ruan, Q. Hu, D. Wen, Q. Chen, G. Chen, Y. Lu, J. Wang, H. Cheng, W. Lu and Z. Gu, *Adv. Mater.*, 2019, **31**, e1806957.

292 J. D. Snook, C. B. Chesson, A. G. Peniche, S. M. Dann, A. Paulucci, I. V. Pinchuk and J. S. Rudra, *J. Mater. Chem. B*, 2016, **4**, 1640–1649.

293 V. Lauth, B. Loretz, C.-M. Lehr, M. Maas and K. Rezwan, *Chem. Mater.*, 2016, **28**, 3796–3803.

294 H. Kakisawa and T. Sumitomo, *Sci. Technol. Adv. Mater.*, 2011, **12**, 064710.

295 T. Kato, T. Suzuki and T. Irie, *Chem. Lett.*, 2000, 186–187.

296 A. Sugawara-Narutaki, *Polym. J.*, 2012, **45**, 269–276.

297 G. Falini, S. Fermani and S. Goffredo, *Semin. Cell Dev. Biol.*, 2015, **46**, 17–26.

298 A. Junaidi, *J. Anim. Vet. Adv.*, 2007, **6**, 591–594.

299 L. Li, M. J. Connors, M. Kolle, G. T. England, D. I. Speiser, X. H. Xiao, J. Aizenberg and C. Ortiz, *Science*, 2015, **350**, 952–956.

300 H. Li, C. Y. Sun, Y. Fang, C. M. Carlson, H. Xu, A. Jesovnik, J. Sosa-Calvo, R. Zarnowski, H. A. Bechtel, J. H. Fournelle, D. R. Andes, T. R. Schultz, P. Gilbert and C. R. Currie, *Nat. Commun.*, 2020, **11**, 5792.

301 J. Wang, Q. Cheng and Z. Tang, *Chem. Soc. Rev.*, 2012, **41**, 1111–1129.

302 Y. Y. Zhang, S. S. Gong, Q. Zhang, P. Ming, S. J. Wan, J. S. Peng, L. Jiang and Q. F. Cheng, *Chem. Soc. Rev.*, 2016, **45**, 2378–2395.

303 S. Kamat, X. Su, R. Ballarini and A. H. Heuer, *Nature*, 2000, **405**, 1036–1040.

304 K. Iwase and K. Mori, *Cryst. Growth Des.*, 2020, **20**, 2091–2098.

305 A. Xin, Y. Su, S. Feng, M. Yan, K. Yu, Z. Feng, K. Hoon Lee, L. Sun and Q. Wang, *Adv. Mater.*, 2021, **33**, e2006946.

306 N. A. Yaraghi and D. Kisailus, *Annu. Rev. Phys. Chem.*, 2018, **69**, 23–57.

307 G. M. Luz and J. F. Mano, *Philos. Trans. R. Soc., A*, 2009, **367**, 1587–1605.

308 A. R. Studart, *Chem. Soc. Rev.*, 2016, **45**, 359–376.

309 H. Zhao, Z. Yang and L. Guo, *NPG Asia Mater.*, 2018, **10**, 1–22.

310 P. Das, J. M. Malho, K. Rahimi, F. H. Schacher, B. Wang, D. E. Demco and A. Walther, *Nat. Commun.*, 2015, **6**, 5967.

311 B. Zhu, N. Jasinski, A. Benitez, M. Noack, D. Park, A. S. Goldmann, C. Barner-Kowollik and A. Walther, *Angew. Chem., Int. Ed.*, 2015, **54**, 8653–8657.

312 A. Finnemore, P. Cunha, T. Shean, S. Vignolini, S. Guldin, M. Oyen and U. Steiner, *Nat. Commun.*, 2012, **3**, 966.

313 H. Bai, Y. Chen, B. Delattre, A. P. Tomsia and R. O. Ritchie, *Sci. Adv.*, 2015, **1**, e1500849.

314 L. B. Mao, H. L. Gao, H. B. Yao, L. Liu, H. Colfen, G. Liu, S. M. Chen, S. K. Li, Y. X. Yan, Y. Y. Liu and S. H. Yu, *Science*, 2016, **354**, 107–110.

315 X. Q. Li and H. C. Zeng, *Adv. Mater.*, 2012, **24**, 6277–6282.

316 P. L. Wang, T. T. Shen, X. Y. Li, Y. Y. Tang and Y. J. Li, *ACS Appl. Nano Mater.*, 2020, **3**, 1272–1281.

317 M. S. Islam, W. S. Choi, B. Nam, C. Yoon and H.-J. Lee, *Chem. Eng. J.*, 2017, **307**, 208–219.

318 Q. Q. Shi, Y. T. Wang, X. Zhang, B. X. Shen, F. M. Wang and Y. F. Zhang, *Fuel Process. Technol.*, 2020, **199**, 106247.

319 S. Mallakpour, A. Abdolmaleki and F. Tabesh, *Ultrason. Sonochem.*, 2018, **41**, 572–581.

320 X. Zhang, D. Shi, X. Li, Y. Zhang, J. Wang and J. Fan, *Chemosphere*, 2019, **224**, 390–397.

321 J. J. Jacob, R. Varalakshmi, S. Gargi, M. A. Jayasri and K. Suthindhiran, *npj Clean Water*, 2018, **1**, 1.

322 R. Liu and B. Lian, *J. Hazard. Mater.*, 2019, **378**, 120707.

323 P. Lin, H. Wu, S. Hsieh, J. Li, C. Dong, C. Chen and S. Hsieh, *Chemosphere*, 2020, **254**, 126903.

324 X. Ma, L. Li, L. Yang, C. Su, K. Wang and K. Jiang, *J. Cryst. Growth*, 2012, **338**, 272–279.

325 X. Ma, L. Li, L. Yang, C. Su, K. Wang, S. Yuan and J. Zhou, *J. Hazard. Mater.*, 2012, **209–210**, 467–477.

326 X. Zhou, W. Liu, J. Zhang, C. Wu, X. Ou, C. Tian, Z. Lin and Z. Dang, *ACS Appl. Mater. Interfaces*, 2017, **9**, 35785–35793.

327 T. Wen, Y. Zhao, T. Zhang, B. Xiong, H. Hu, Q. Zhang and S. Song, *Chemosphere*, 2020, **246**, 125842.

328 H. Henry, M. F. Naujokas, C. Attanayake, N. T. Basta, Z. Q. Cheng, G. M. Hettiarachchi, M. Maddaloni, C. Schadt and K. G. Scheckel, *Environ. Sci. Technol.*, 2015, **49**, 8948–8958.

329 Y. Du, F. Lian and L. Zhu, *Environ. Pollut.*, 2011, **159**, 1763–1768.

330 X. Zhou, W. Liu, C. Tian, S. Mo, X. Liu, H. Deng and Z. Lin, *Chem. Eng. J*, 2018, **351**, 816–824.

331 H. Merrikhpour and M. Jalali, *Clean Technol. Environ. Policy*, 2012, **14**, 845–855.

332 B. Xiong, T. Zhang, Y. Zhao, T. Wen, Q. Zhang, S. Bao and S. Song, *Sci. Total Environ.*, 2020, **698**, 134270.

333 M. Zaharia, F. Bucatariu, F. Doroftei, D. Loghin, A. Vasiliu and M. Mihai, *Colloid Surf., A*, 2021, **613**, 126084.

334 S. Ramola, T. Belwal, C. J. Li, Y. Y. Wang, H. H. Lu, S. M. Yang and C. H. Zhou, *Sci. Total Environ.*, 2020, **709**, 136171.

335 Y. Lei, J. Remmers, M. Saakes, R. van der Weijden and C. Buisman, *ACS Sustainable Chem. Eng.*, 2019, **7**, 7362–7368.

336 Y. Lei, S. Narsing, M. Saakes, R. D. van der Weijden and C. J. N. Buisman, *Environ. Sci. Technol.*, 2019, **53**, 10774–10780.

337 S. Ramola, T. Belwal, C. J. Li, Y. X. Liu, Y. Y. Wang, S. M. Yang and C. H. Zhou, *J. Cleaner Prod.*, 2021, **299**, 126802.

338 X. Yuan, W.-C. Nie, C. Xu, X.-H. Wang, Q. Xiao, F. Song, X.-L. Wang and Y.-Z. Wang, *Adv. Funct. Mater.*, 2018, **28**, 1704956.

339 J. Dai, L. Wang, Y. Wang, S. Tian, X. Tian, A. Xie, R. Zhang, Y. Yan and J. Pan, *ACS Appl. Mater. Interfaces*, 2020, **12**, 4482–4493.

340 R. K. Gupta, G. J. Dunderdale, M. W. England and A. Hozumi, *J. Mater. Chem. A*, 2017, **5**, 16025–16058.

341 J. D. Dai, L. L. Wang, Y. Wang, S. J. Tian, X. H. Tian, A. H. Xie, R. L. Zhang, Y. S. Yan and J. M. Pan, *ACS Appl. Mater. Interfaces*, 2020, **12**, 4482–4493.

342 J. Yang, J. Y. Cui, A. T. Xie, J. D. Dai, C. X. Li and Y. S. Yan, *Colloids Surf., A*, 2021, **608**, 125583.

343 M. Li, Y. Chen, L. B. Mao, Y. Jiang, M. F. Liu, Q. Huang, Z. Yu, S. Wang, S. H. Yu, C. Lin, X. Y. Liu and H. Colfen, *Langmuir*, 2018, **34**, 2942–2951.

344 S. K. Tang, X. T. Chang, M. Y. Li, T. Ge, S. C. Niu, D. S. Wang, Y. C. Jiang and S. B. Sun, *Chem. Eng. J.*, 2021, **405**, 126597.

345 Y. Guo, D.-P. Yang, M. Liu, X. Zhang, Y. Chen, J. Huang, Q. Li and R. Luque, *J. Mater. Chem. A*, 2019, **7**, 8832–8844.

346 X. Zhang, J. Huang, Z. Kang, D.-P. Yang and R. Luque, *Mol. Catal.*, 2020, **484**, 110786.

347 X. H. Zhang, M. H. Liu, Z. W. Kang, B. Q. Wang, B. Wang, F. Y. Jiang, X. S. Wang, D.-P. Yang and R. Luque, *Chem. Eng. J.*, 2020, **388**, 124304.

348 S. Yu, X. Wang and D. Wu, *Energy Fuels*, 2014, **28**, 3519–3529.

349 H. Liu, X. Tian, M. Ouyang, X. Wang, D. Wu and X. Wang, *Renewable Energy*, 2021, **179**, 47–64.

350 Y. Jiang, D. Wang and T. Zhao, *J. Appl. Polym. Sci.*, 2007, **104**, 2799–2806.

351 L. Sánchez, P. Sánchez, A. de Lucas, M. Carmona and J. F. Rodríguez, *Colloid Polym. Sci.*, 2007, **285**, 1377–1385.

352 Y. Ma, J. Zong, W. Li, L. Chen, X. Tang, N. Han, J. Wang and X. Zhang, *Energy*, 2015, **87**, 86–94.

353 Q. Zhang, C. Liu and Z. Rao, *ChemistrySelect*, 2019, **4**, 8482–8492.

354 S. Yu, X. Wang and D. Wu, *Appl. Energy*, 2014, **114**, 632–643.

355 T. Wang, S. Wang, R. Luo, C. Zhu, T. Akiyama and Z. Zhang, *Appl. Energy*, 2016, **171**, 113–119.

356 Z. Jiang, W. Yang, F. He, C. Xie, J. Fan, J. Wu and K. Zhang, *Langmuir*, 2018, **34**, 14254–14264.

357 Y. Fang, T. Zou, X. Liang, S. Wang, X. Liu, X. Gao and Z. Zhang, *ACS Sustainable Chem. Eng.*, 2017, **5**, 3074–3080.

358 Z. Jiang, W. Yang, F. He, C. Xie, J. Fan, J. Wu and K. Zhang, *ACS Sustainable Chem. Eng.*, 2018, **6**, 5182–5191.

359 H. Wei, F. He, Y. Li, Q. Zhang, Y. Zhou, H. Yan, R. He, J. Fan and W. Yang, *ACS Sustainable Chem. Eng.*, 2019, **7**, 18854–18862.

360 S. Emir and H. Paksoy, *Energy Storage*, 2020, **3**, e214.

361 Y. Pan, M. Wu and Q. Su, *Mater. Res. Bull.*, 2003, **38**, 1537–1544.

362 H. He, J. Li, L. Liu, S. Bao, X. Chen, P. Zhang, W. Zhang and X. Lai, *Ceram. Int.*, 2018, **44**, 5070–5075.

363 H. Zhu, B. Qian, X. Zhou, Y. Song, K. Zheng, Y. Sheng and H. Zou, *J. Lumin.*, 2018, **203**, 441–446.

364 E. A. Minchin, *Fortschr. Zool.*, 2022, **2**, 171–274.

365 L. Addadi, S. Raz and S. Weiner, *Adv. Mater.*, 2003, **15**, 959–970.

366 M. J. Root, *Calcif. Tissue Int.*, 1990, **47**, 112–116.

367 N. Nassif, N. Pinna, N. Gehrke, M. Antonietti, C. Jager and H. Colfen, *Proc. Natl. Acad. Sci. U. S. A.*, 2005, **102**, 12653–12655.

368 Y. Levi-Kalisman, S. Raz, S. Weiner, L. Addadi and I. Sagi, *Adv. Funct. Mater.*, 2002, **12**, 43–48.

369 R. S. K. Lam, J. M. Charnock, A. Lennie and F. C. Meldrum, *CrystEngComm*, 2007, **9**, 1226–1236.

370 D. Gebauer, P. N. Gunawidjaja, J. Y. P. Ko, Z. Bacsik, B. Aziz, L. Liu, Y. Hu, L. Bergström, C.-W. Tai, T.-K. Sham, M. Edén and N. Hedin, *Angew. Chem., Int. Ed.*, 2010, **49**, 8889–8891.

371 Z. Zou, X. Yang, M. Albéric, T. Heil, Q. Wang, B. Pokroy, Y. Politi and L. Bertinetti, *Adv. Funct. Mater.*, 2020, **30**, 2000003.

372 Z. Zou, J. Xie, E. Macías-Sánchez and Z. Fu, *Cryst. Growth Des.*, 2020, **21**, 414–423.

373 S. Kajiyama, T. Nishimura, T. Sakamoto and T. Kato, *Small*, 2014, **10**, 1634–1641.

374 S. Matsumura, S. Kajiyama, T. Nishimura and T. Kato, *Small*, 2015, **11**, 5127–5133.

375 L. K. Grunenfelder, S. Herrera and D. Kisailus, *Small*, 2014, **10**, 3207–3232.

376 J. Jiang, M. R. Gao, Y. H. Qiu and S. H. Yu, *Nanoscale*, 2010, **2**, 2358–2361.

377 C. Zhong and C. C. Chu, *Langmuir*, 2009, **25**, 3045–3049.

378 I. Sondi, S. D. Skapin and B. Salopek-Sondi, *Cryst. Growth Des.*, 2008, **8**, 435–441.

379 M. Faatz, F. Grohn and G. Wegner, *Mater. Sci. Eng., C*, 2005, **25**, 153–159.

380 J. M. Xto, C. N. Borca, J. A. van Bokhoven and T. Huthwelker, *Chem. Commun.*, 2019, **55**, 10725–10728.

381 J. Ihli, A. N. Kulak and F. C. Meldrum, *Chem. Commun.*, 2013, **49**, 3134–3136.

382 S. Leukel, M. Panthöfer, M. Mondeshki, G. Kieslich, Y. Wu, N. Krautwurst and W. Tremel, *Chem. Mater.*, 2018, **30**, 6040–6052.

383 R. Sun, P. Zhang, É. G. Bajnóczi, A. Neagu, C.-W. Tai, I. Persson, M. Strømme and O. Cheung, *ACS Appl. Mater. Interfaces*, 2018, **10**, 21556–21564.

384 S. F. Chen, H. Colfen, M. Antonietti and S. H. Yu, *Chem. Commun.*, 2013, **49**, 9564–9566.

385 J. Ihli, Y. Y. Kim, E. H. Noel and F. C. Meldrum, *Adv. Funct. Mater.*, 2013, **23**, 1575–1585.

386 B. Guillemet, M. Faatz, F. Grohn, G. Wegner and Y. Gnanou, *Langmuir*, 2006, **22**, 1875–1879.

387 F. J. Zhu, T. Nishimura, T. Sakamoto, H. Tomono, H. Nada, Y. Okumura, H. Kikuchi and T. Kato, *Chem. – Asian J.*, 2013, **8**, 3002–3009.

388 E. Loste, R. M. Wilson, R. Seshadri and F. C. Meldrum, *J. Cryst. Growth*, 2003, **254**, 206–218.

389 J. D. Rodriguez-Blanco, S. Shaw, P. Bots, T. Roncal-Herrero and L. G. Benning, *J. Alloys Compd.*, 2012, **536**, S477–S479.

390 S. Zhang, O. Nahi, L. Chen, Z. Aslam, N. Kapur, Y. Y. Kim and F. C. Meldrum, *Adv. Funct. Mater.*, 2022, **32**, 2201394.

391 A. Gal, S. Weiner and L. Addadi, *J. Am. Ceram. Soc.*, 2010, **132**, 13208–13211.

392 A. Al-Sawalmih, C. Li, S. Siegel, P. Fratzl and O. Paris, *Adv. Mater.*, 2009, **21**, 4011–4015.

393 A. Sato, S. Nagasaka, K. Furihata, S. Nagata, I. Arai, K. Saruwatari, T. Kogure, S. Sakuda and H. Nagasawa, *Nat. Chem. Biol.*, 2011, **7**, 197–199.

394 E. M. Pouget, P. H. H. Bomans, J. A. C. M. Goos, P. M. Frederik, G. D. With and N. A. J. M. Sommerdijk, *Science*, 2009, **323**, 1455–1458.

395 S. Sun, D. Gebauer and H. Colfen, *Chem. Commun.*, 2016, **52**, 7036–7038.

396 S.-S. Wang and A.-W. Xu, *Cryst. Growth Des.*, 2013, **13**, 1937–1942.

397 W. Shi, Z. Ma, Y. Mu, J. Wang, B. Li, X. Wang, Z. Teng and X. Liu, *RSC Adv.*, 2017, **7**, 45113–45120.

398 L. B. Gower and D. J. Odom, *J. Cryst. Growth*, 2000, **210**, 719–734.

399 Y. Jiang, M. Kellermeier, D. Gebaue, Z. Lu, R. Rosenberg, A. Moise, M. Przybylski and H. Colfen, *Nat. Commun.*, 2017, **8**, 15933.

400 Z. Zou, L. Bertinetti, Y. Politi, P. Fratzl and W. Habraken, *Small*, 2017, **13**, 1603100.

401 J. Su, X. Liang, Q. Zhou, G. Zhang, H. Wang, L. Xie and R. Zhang, *Biochem. J.*, 2013, **453**, 179–186.

402 D. J. Tobler, J. D. R. Blanco, K. Dideriksen, K. K. Sand, N. Bovet, L. G. Benning and S. L. S. Stipp, *Procedia Earth Planet. Sci.*, 2014, **10**, 143–148.

403 Z. Zou, I. Polishchuk, L. Bertinetti, B. Pokroy, Y. Politi, P. Fratzl and W. Habraken, *J. Mat. Chem. B*, 2018, **6**, 449–457.

404 D. J. Tobler, J. D. Rodriguez Blanco, H. O. Sørensen, S. L. S. Stipp and K. Dideriksen, *Cryst. Growth Des.*, 2016, **16**, 4500–4508.

405 J. Ihli, W. C. Wong, E. H. Noel, Y. Y. Kim, A. N. Kulak, H. K. Christenson, M. J. Duer and F. C. Meldrum, *Nat. Commun.*, 2014, **5**, 3169.

406 M. Saharay, A. O. Yazaydin and R. J. Kirkpatrick, *J. Phys. Chem. B*, 2013, **117**, 3328–3336.

407 E. Beniash, J. Aizenberg, L. Addadi and S. Weiner, *Proc. R. Soc. B*, 1997, **264**, 461–465.

408 T. Y. J. Han and J. Aizenberg, *Chem. Mater.*, 2008, **20**, 1064–1068.

409 S. Raz, O. Testeniere, A. Hecker, S. Weiner and G. Luquet, *Biol. Bull.*, 2002, **203**, 269–274.

410 T. Saito, Y. Oaki, T. Nishimura, A. Isogai and T. Kato, *Mater. Horiz.*, 2014, **1**, 321–325.

411 D. Kuo, T. Nishimura, S. Kajiyama and T. Kato, *ACS Omega*, 2018, **3**, 12722–12729.

412 H. Ping, H. Xie, Y. M. Wan, Z. X. Zhang, J. Zhang, M. Y. Xiang, J. J. Xie, H. Wang, W. M. Wang and Z. Y. Fu, *J. Mater. Chem. B*, 2016, **4**, 880–886.

413 M. Milovanovic, L. Mihailowitsch, M. Santhirasegaran, V. Brandt and J. C. Tiller, *J. Mater. Sci.*, 2021, **56**, 15299–15312.

414 C. Xu, Y. Yan, J. Tan, D. Yang, X. Jia, L. Wang, Y. Xu, S. Cao and S. Sun, *Adv. Funct. Mater.*, 2019, **29**, 1808146.

415 Y. Zhao, Z. Luo, M. Li, Q. Qu, X. Ma, S. H. Yu and Y. Zhao, *Angew. Chem., Int. Ed.*, 2015, **54**, 919–922.

416 T. L. Liu, L. L. Li, X. Teng, X. L. Huang, H. Y. Liu, D. Chen, J. Ren, J. Q. He and F. Q. Tang, *Biomaterials*, 2011, **32**, 1657–1668.

417 C. Wang, X. Liu, S. Chen, F. Hu, J. Sun and H. Yuan, *Chem. Commun.*, 2018, **54**, 13080–13083.

418 C. Wang, S. Chen, Q. Yu, F. Hu and H. Yuan, *J. Mater. Chem. B*, 2017, **5**, 2068–2073.

419 C. Wang, S. Chen, Y. Wang, X. Liu, F. Hu, J. Sun and H. Yuan, *Adv. Mater.*, 2018, **30**, e1706407.

420 M. Wang, B. Zhou, L. Wang, F. Zhou, N. Smith, D. Saunders, R. A. Towner, J. Song, J. Qu and W. R. Chen, *J. Mat. Chem. B*, 2020, **8**, 8261–8270.